VILNIUS UNIVERSITY

Martynas Barkauskas

TIME-RESOLVED SPECTROSCOPY OF NONLINEAR CRYSTALS AND PHOTOCHROMIC SWICHES

Doctoral dissertation

Physical sciences, physics (02 P)

Vilnius, 2009

Dissertation was prepared at the Vilnius University in 2004-2008

Scientific supervisor:
prof. habil. dr. Valdas Sirutkaitis (Vilnius University, physical sciences, physics – 02 P)

Scientific advisor:
doc. dr. Mikas Vengris (Vilnius University, physical sciences, physics – 02 P)

VILNIAUS UNIVERSITETAS

Martynas Barkauskas

NETIESINIŲ KRISTALŲ IR FOTOCHROMINIŲ JUNGIKLIŲ KINETINĖ SPEKTROSKOPIJA

Daktaro disertacija
Fiziniai mokslai, fizika (02 P)

Vilnius, 2009

Disertacija rengta 2004-2008 metais Vilniaus universitete

Mokslinis vadovas:
prof. habil. dr. Valdas Sirutkaitis (Vilniaus universitetas, fiziniai mokslai, fizika – 02 P)

Konsultantas:
doc. dr. Mikas Vengris (Vilniaus universitetas, fiziniai mokslai, fizika – 02 P)

Contents

List of abbreviations

DKDP – potassium dideuterium phosphate (KD_2PO_4), nonlinear crystal
EPR – electron paramagnetic resonance
ESA – excited state absorption
IA – induced absorption
IB1 – indolo[2,1-*b*][1,3]benzoxazine, IB1a(b) refers to the opened (or closed) form
ICF – inertial confinement fusion
IndI – Indolium-Iodide, a model compound
IR – infrared
FWHM – full width at half maximum
GSB – ground state bleaching
KDP – potassium dihydrogen phosphate (KH_2PO_4), nonlinear crystal
LIL – Laser Integration Line, a prototype facility for LMJ (see below)
LMJ – Laser Mégajoule, a high-power laser facility in France aimed at achieving ICF
MeCN – acetonitrile (CH_3CN), solvent
MPTAS – multipulse transient absorption spectroscopy/spectrometer
nIR – near infrared
Nd:YVO_4 – neodymium-doped yttrium orthvanadate
Nd:YAG – neodymium-doped yttrium aluminium garnet (Nd:$Y_3Al_5O_{12}$)
OPA – optical parametric amplifier
PDP – pump-dump-probe
pNph and pNphe – 4-nitrophenol and 4-nitrophenolate
PP – pump-probe
PrPP – pump-repump-probe
R-KDP – KH_2PO_4 crystal grown by rapid-growth technique
SADS – species associated difference spectrum
SE – stimulated emission
SHG – second harmonic generation
TA – transient absorption
TPA – two-photon absorption
UV – ultraviolet
VIS – visible region

i. Introduction

The phenomenon of time and temporal change has been one of the most fundamental concepts of science. Temporal changes directly investigated by scientific methods occur on the time scales which comprise more than 33 orders of magnitudes. This covers recently reported temporal distinguishment between photoelectrons coming from different states of crystalline tungsten [1], which requires time resolution in the order of 100 attoseconds (10^{-16} s); and the current estimate for the age of the universe: 13.7 bilion years ($4.3 \cdot 10^{17}$ s), that comes form the ongoing cosmic microwave background observations [2]. As the expansion to the longest time scales is limited by the “big bang” itself, the pursue for ever shorter timescales has tremendously advanced by some 13 orders of magnitude over the last six decades. And this expansion is probably going to continue, because in the field of particle physics, scientists are already making indirect observation based estimates of events with the durations of yoctoseconds (10^{-24} s).

One of the main frontiers of short-timescale science is the transient absorption spectroscopy that was initially pioneered by Norrish and Porter [3] in 1949. At first this technique gained the grounds of its time resolution from advances in electronics, but since the invention of laser in 1960 by Maiman [4] and generation of the ultrashort pulses in 1964 [5] the improvements of time resolution was simultaneous with the developments of ever shorter laser pulses. The introduction of optical parametric amplifiers and generators [6, 7] greatly increased the range of accessible wavelengths, thus allowing thorough investigation of almost any sample. Currently transient spectroscopic techniques are widely applied in biophysics, nanoparticle research, solar cell research and various aspects of physical chemistry; they allow investigation of ongoing intra- or inter-molecular dynamics in gas or condensed phases.

The technical backbone of this thesis is three transient absorption setups that have been constructed and used to investigate dynamics in nonlinear crystals and photochromic compounds. The main spectrometer is presented in chapter 3 and it is aimed at spectroscopic investigations with femtosecond time resolution and possibility to implement non-trivial excitation and (de-)re-excitation schemes. Second one, presented in section 4.2.4, is a standard flash photolysis setup with a nanosecond temporal resolution, which complements the first setup in the investigations that stretch out of the ultrafast time domain. And last but not the least, a setup described in section 2.3.3 that is dedicated to the long-lived transient absorption detection induced by high pump laser fluencies. This setup, in contrast to the flash photolysis arrangement, uses a coherent probe source (i.e. pulsed laser) that allows minimizing the interaction region of pump and probe, thus loosening the requirement of very high energy pump laser.

The main **goal** of this thesis was to implement optical transient absorption measurement methods in a wide temporal range and to apply them in the investigation of nonlinear crystals and photochromic switches. By planning ahead these investigations, the following specific **tasks** were set:

- Construction of femtosecond multi-pulse transient absorption spectrometer and nanosecond flash photolysis setup.
- Experimental study of UV-laser induced transient defects in large aperture rapidly-grown KDP (R-KDP) crystals.
- Spectroscopic investigation of newly synthesized molecular switches.

The **innovations** presented in this thesis are:

- Two-photon absorption anisotropy at 355 nm in KDP crystals was observed for the first time.
- Elucidation of the UV-laser induced conditioning effect on to the lifetimes of transient defect-states in R-KDP crystals.
- Primary investigation of ultrafast dynamics in the indolo[2,1-*b*][1,3]benzoxazine-type photochromes.

The **statements to defend** in this thesis are:

- Two-photon absorption of 355 nm laser pulses induces VIS absorbing defects in R-KDP crystals, which fully decay within ca. 6 s.
- Overall lifetime increase of transient defect-states in R-KDP is associated with UV-laser induced conditioning effect and this can over time increase the accumulation of absorbing defects in laser systems that use R-KDP crystals.
- Deprotonation of 4-nitrophenol in acetonitrile solution, causes a decrease of excited state lifetime by ~2 orders of magnitude that makes it an efficient excitation quenching moiety in molecular complexes.
- After photoexcitation oxazine ring in indolo[2,1-*b*][1,3]benzoxazine opens in ca. 12 ps and fully closes back within < 100 ns.

This thesis is arranged in the following way. The first chapter provides an introduction to time-resolved absorption techniques at various time domains. The second chapter starts with a short overview on KDP crystals and their defects followed by the investigation of

absorbing defects formation and decay in rapidly grown KDP crystals. The third chapter presents a detailed description and characterization of three-pulse transient absorption spectrometer along with the demonstration of direct observation of ground state dynamics in membrane marker molecule. Finally the fourth chapter is a detailed investigation of ultrafast dynamics in a newly synthesized photochromic compound.

ii. Author's publications

The results presented in this thesis were published in 2 papers in peer-reviewed journals (A1-A2) and 1 paper in journal with an impact-factor (A3). In addition, author's publications not included in this thesis are also listed below (B1-B5).

Publications:

[A1] **M. Barkauskas**, A. Melninkaitis, M. Šinkevičius, A. Čiburys, R. Gadonas, V. Sirutkaitis, H. Bercegol, and L. Lamaignère, Linear and nonlinear absorption and defects formation in KDP crystals used for large aperture doublers and triplers, SPIE **5949**, 59491T (2005).

[A2] **M. Barkauskas**, A. Melninkaitis, D. Mikšys, L. Meslinaitė, R. Grigonis, V. Sirutkaitis, H. Bercegol, and L. Lamaignère, Characterization of KDP crystals used in large aperture doublers and triplers, SPIE **6403**, 64031V (2006).

[A3] **M. Barkauskas**, V. Martynaitis, A. Šačkus, R. Rotomskis, V. Sirutkaitis, and M. Vengris, Ultrafast dynamics of photochromic compound based on oxazine ring opening, Lithuanian Journal of Physics **48** (3), 231-242 (2008).

Other publications (not included in this thesis):

[B1] B. Sherliker, M. Halsall, I. Kasalynas, D. Seliuta, G. Valusis, M. Vengris, **M. Barkauskas**, V. Sirutkaitis, P. Harrison, V.D. Jovanovic, D. Indjin, Z. Ikonic, P.J. Parbook, T. Wang, and P.D. Buckle, Room temperature operation of AlGaN/GaN quantum well infrared photodetectors at a 3-4 μm wavelength range, Semicond. Sci. Technol. **22**, 1240-1244 (2007).

[B2] **M. Barkauskas**, F. Brandi, F. Giammanco, D. Neshev, A. Pirri, and W. Ubachs, A novel-type tunable and narrowband extreme ultraviolet radiation source based on high-harmonic conversion of picosecond laser pulses, J. Electron. Spectrosc. Relat. Phenom. **144**, 1151-1155 (2005).

[B3] F. Giammanco, A. Pirri, F. Brandi, **M. Barkauskas**, and W. Ubachs, Measurement of chirp-induced frequency shift in high-order harmonic generation in xenon, Laser Phys. **15**, 328-333 (2005).

[B4] V. Sirutkaitis, E. Gaižauskas, V. Kundriašov, **M. Barkauskas**, V. Vaičaitis, R. Grigonis, and A.P. Piskarskas, Self-guiding supercontinuum generation and damage in bulk materials induced by femtosecond pulses, SPIE **4932**, 346-357 (2003).

[B5] O. Balachninaitė, **M. Barkauskas**, R.C. Eckardt, R. Grigonis, M. Maciulevičius, A. Melninkaitis, and V. Sirutkaitis, Absorptance measurement of nonlinear crystals by calorimetric method at 1064 and 532 nm, SPIE **4751**, 291-296 (2002)

iii. Author's contribution

The author has built up the setups described in sections 2.3.3 and 4.2.4, as well as the one described in chapter 3. He has carried out all the experiments and data analysis presented in this thesis. In addition to that, he was responsible for writing the drafts of accompanying publications.

1. Time-resolved absorption spectroscopies

In this chapter time-resolved absorption techniques are introduced mostly in the order in which they have developed historically, while a short account of studied systems is also included.

1.1. Microsecond flash spectrometers

The first attempts to use flash discharges of (probably) a few microseconds duration for the time resolution of fast events were carried out as early as 1851 when Fox Talbot made a photographic record of a rapidly rotating cylinder onto which a newspaper was adhered. In an another well-known (and often mythologized) story, photography pioneer Eadweard Muybridge, on commission from Leland Stanford, in 1877 developed a system of rapid-sequence photography to conclusively prove that a galloping or trotting horse briefly has all four feet aloft simultaneously – an event too fast for the human eye to follow. However after that, it took about a century before Norrish and Porter [3] in 1949 developed the technique of flash photolysis, used to study photochemical reactions, that broke through the millisecond barrier of observable events. This achievement was letter recognized by the Nobel prize in chemistry (1967). Up to the commencement of flash photolysis the shortest lifetimes which could be directly measured were of the order of a few milliseconds; though indirect methods were already available which allowed the determination of excited states lifetimes in a ns time scale, i.e. estimation form oscillator strengths and fluorescence quantum yields, Stern-Volmer quenching or spectral linewidth measurements.

In a conventional flash photolysis setup the sample, typically enclosed in cylindrical cell with path length of a few centimeters; is excited by short flashes of light that are generated by rapid electrical

discharge in the gas tube. Optical filters are commonly used to select a suitable wavelength region for excitation and (multi-)elliptical reflectors focus the light onto the sample. Typical durations of these flashes are from roughly one microsecond to several milliseconds, and although shorter flashes can be also generated, they are not used in practice since the flash energy rapidly decreases with reduction of pulse duration. The detection of generated short-lived species in conventional flash photolysis can be divided into two measurement modes: the kinetic and the spectroscopic technique. In the kinetics measurement, a thoroughly stabilized continuous lamp is used as the steady source of the monitoring beam (Xe arc lamps are widely used for that purpose), and the temporal changes in its transmission through the sample are monitored with light detector and storage oscilloscope/recorder. In the spectroscopic mode, the transient spectrum is obtained in a single experiment if a second flashlamp is used as an analyzing light source together with a spectrograph and detector array. In this case temporal delay is introduced between excitation and monitoring flashes. Temporal resolution in both methods is limited by the duration of flashes.

1.2. Laser flash photolysis (nanosecond time domain)

Soon after the invention of the laser in 1960 by Maiman [4], it became possible, by employing active or passive Q-switching, to generate light pulses of a few nanoseconds in duration. These light ‘flashes’ easily have peak powers in the order of tens of mega-watts which corresponds to $>10^{16}$ photons/ns (in VIS range). Replacing the discharge lamps by the pulsed laser source and maintaining the basic principles described above, allowed the time resolution to be improved by roughly 3 orders of magnitude [8], this required much faster sampling oscilloscopes and detectors. Use of laser light and its unique

properties also provides some additional advantages for the laser flash photolysis[1]; e.g. a small beam divergence enables focusing the light into a small area that, in turn, allows to use much smaller quantities of sample, compared to conventional flash photolysis. Active volumes of a few mm^3 are quite common. Another advantageous laser feature is the coherence of light, which allows the measurement of properties connected not only with the amplitude but also with the phase of light; like in the case of transient grating method [9], which allows investigating not only the changes in transmission due to photochemical relaxations, but also physical phenomena like diffusion [10]. With the advent of tunable laser light, another laser property was harnessed for scientific purposes; namely, the relatively narrow bandwidth of the laser light that allows selective excitation of the states present in the sample.

1.3. Spectroscopy with ultra-fast pulses (pico- and femto-second domain)

Excited state lifetimes of molecules or molecular complexes typically are of the order of several nanoseconds. Thus the development of the first picosecond laser source by De Maria *et al.* [11], opened a new realm for the investigations of (intra-)inter-molecular energy transfer, orientational relaxation in liquids, photodissociation or photoionization etc. Later on, the time resolution of spectroscopic investigations rapidly increased with the development of ever shorter laser pulses, while almost reaching its natural limit in the optical domain of sub-5 fs pulses [12].

In contrast to millisecond, microsecond and nanosecond spectroscopy the “classical” detection techniques (oscilloscopes,

[1] Note that these advantages are not restricted to the nanosecond domain, but are applicable to all times scales as long as laser light is in use.

photodetectors etc.) can not be used in (pico-)femtosecond range because of their bandwidth limitations. The basic principle of ps and fs absorption spectrometer is the use of the excite-and-probe (often called pump-probe – PP) technique. Like in the laser flash spectroscopy (see section 1.2) a strong laser pulse excites the sample while a weak probe pulse 'looks' for the changes in transmission, reflection, gain and/or polarization after a variable time delay. In contrast to the spectroscopy in ms-ns range, in these experiments the excitation and probe beams come from the same laser source. The time delay is typically achieved by an optical delay line using the constant propagation velocity of light in air 0.3 mm/ps.

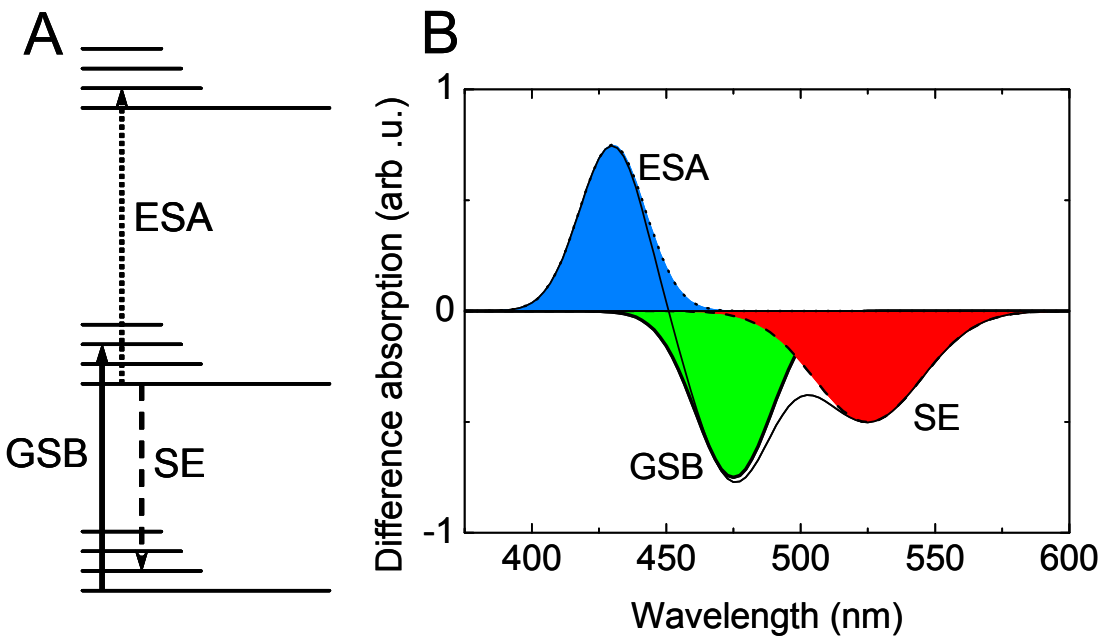

Figure 1.1 The energy level scheme (A) of a hypothetical molecule and different transitions influencing the pump-probe spectrum (B): ground state bleach (GBS), stimulated emission (SE) and excited state absorptions (ESA). By tuning the third pulse of a laser into the resonance with ESA and SE band, a means of controlling the photoreaction can be established. In the case the third pulse acting on ESA, pump-repump-probe technique (PrPP) is obtained, whereas if the third pulse is in resonance with SE, the technique is called pump-dump-probe (PDP).

Pump-probe spectroscopy, is probably the most widely used ultrafast technique to investigate photoinduced reactions [13]. PP data are usually presented in the form of time-resolved difference spectra, i.e. $\Delta OD = \Delta OD(t,\lambda)$, where ΔOD is the difference between the sample absorbance with and without the pump pulse (Figure 1.1 B). The absorption-difference (ΔOD) spectra measured in pump-probe experiments are shaped by a number of qualitatively different contributions that may originate from transitions between the different states of the system (Figure 1.1 A), e.g. ground state bleach (GSB), stimulated emission (SE) and induced absorption (excited state absorption, ESA, or absorption by nonequilibrated ground state). Without additional experimental information, when no additional control is exerted on the sample, these contributions often become impossible to distinguish one from another and the data interpretation becomes ambiguous.

1.4. Multipulse transient absorption spectroscopy

The difficulties of traditional PP experiment can be addressed using multipulse transient absorption spectroscopies (MPTAS) that involve the introduction of a third pulse to the PP experiment [14]. This additional pulse can be appropriately wavelength-tuned and delayed to selectively interact with a 'targeted' electronic transition. In PDP experiments, this added pulse interacts with the SE of an exited state and results in the de-excitation of molecules and the transfer of population from the excited state to the ground state. In PrPP experiments, the additional pulse interacts with an ESA band and causes the redistribution of population within the excited state manifold whilst the total amount of excitations is preserved, i.e. the ground state population remains unaffected.

Ultrafast single-wavelength PDP experiments were initially used to study the properties of the excited states in bacteriorhodopsin by Gai *et al.* in 1997 [14, 15], while also used in the study of ground state dynamics in calmodulin [16]; asymptotic-limited dispersed PDP has been used to study ground state liquid dynamics [17]. The higher excited-state dynamics of bacteriorhodopsin has been studied by single wavelength PrPP [18] and the combined use o PDP and PrPP allowed the discrimination of overlapping bands in the PP signals [14]. In the recent years, the MPTAS techniques have been further developed to include dispersed detection [19, 20], which allows the simultaneous probing of complete spectra with an unprecedented signal-to-noise ratio, that subsequently can be analyzed globally. This development, which allowed to test explicit physical models for light-driven biological processes, moved ultrafast research to a qualitatively new level.

The utility of MPTAS spectroscopies lies in their ability to control reaction as they evolve, by manipulating the populations of transient species with applied laser pulses. This is, to a certain extent, related to coherent control mechanism where reactions are manipulated via complex processes such as vibrational wave packet motion, quantum interferences and electronic coherences [21]. A more appropriate term for describing MPTAS spectroscopies is incoherent control, because the control effects are achieved and the data is interpreted solely in terms of manipulated electronic state populations.

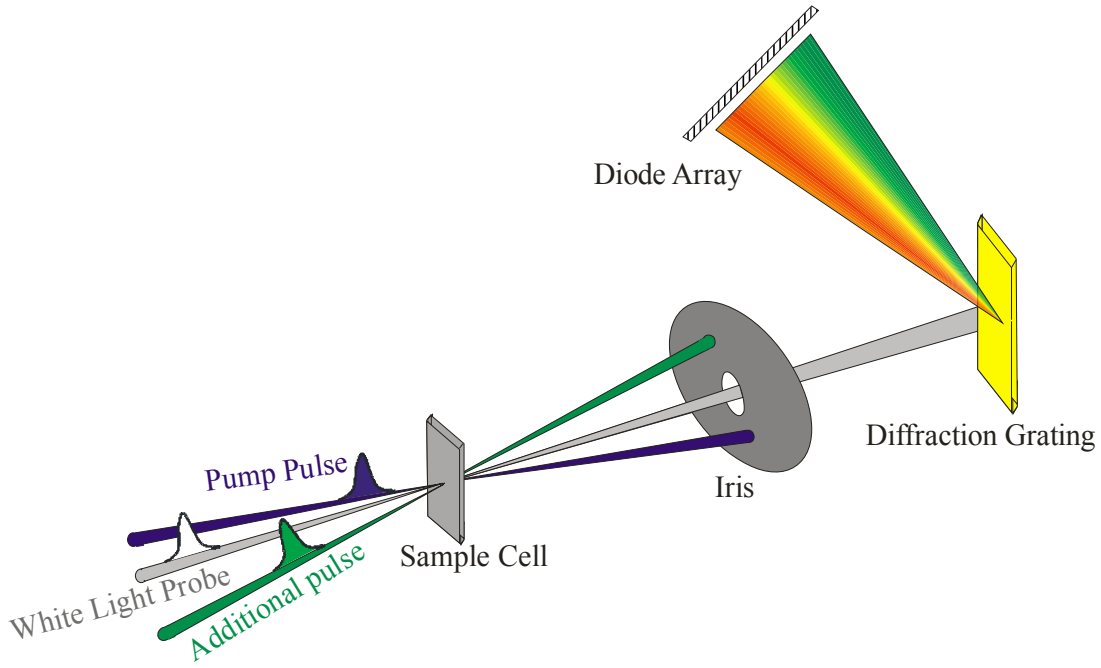

Figure 1.2 Laser beam arrangement in the multipulse transient absorption experiment. The additional pulse can be in resonance with excited state absorption or stimulated emission.

2. Investigation of transient defects in rapidly-grown KDP crystals

In this chapter, a short overview on KDP crystal structure, growth and selected defects is followed by the spectroscopic investigation of UV-induced formation, bleaching and decay of transient defect-states in large aperture rapidly-grown KDP crystals (R-KDP). In the end, connection between defect decay kinetics and the UV-stimulated conditioning effect in R-KDP is elucidated.

2.1. Introduction

Potassium dihydrogen phosphate (KH_2PO_4 or KDP for short) and its deuterated isomorph (KD_2PO_4 or DKDP) are nonlinear crystals with a broad transparency range, extending form the UV to nIR regions; together with their remarkable nonlinear and electro-optical properties, these are the major factors leading to a widespread usage of (D)KDP crystals in various laser systems [22]. The exclusive ability for KDP and DKDP to be grown as a single large-size crystals have also made them technologically attractive and unique for the nonlinear optics applications in large-aperture laser systems. The state-of-the-art for these large-size and high-power lasers are the inertial confinement fusion (ICF) [23] drivers that require large scale crystals for the frequency doubling and tripling applications [24]. Additionally large aperture electro-optical switches (Pockels cells), with diameters of over 400 mm [25], are necessary for their regenerative booster amplifiers [26]. At present, all the major ICF experimental facilities (for example: National Ignition Facility in the US [27], Laser Mégajoule (LMJ) in France [28] and Iskra-6 in Russia [29]) are using or plan to use KDP and DKDP crystals for above mentioned applications.

In recent years, large KDP and DKDP crystals have been successfully grown from highly supersaturated solutions at the rates of over 30 mm/day [30-33]. This rapid crystal growth technique decreases the costs and growth periods for large aperture crystals. However, some important crystal quality parameters, as absorption losses, scattering and laser-induced damage thresholds, were reported to worsen in rapidly-grown crystals as compared with the ones grown using conventional methods [34, 35]. Additionally, it was shown that these parameters vary not only depending on the crystal growth conditions [35-37], but even within different parts of the same crystal boule [38, 39]. Thus in order to reliably predict the performance of large aperture systems, a detailed investigation of aforementioned parameters is required in R-KDP crystals.

One of the major concerns in the practical applications of KDP crystals is that under intense UV irradiation unwanted optical absorption bands are produced in 200-700 nm spectral region [40]. This induced absorption in (D)KDP crystals is caused by the generation of transient defect states [41], that fully decay with characteristic times ranging from a few tens of milliseconds to a few seconds [42]. Transient coloration is even more important in the large-aperture systems, because their maximum output energy is usually limited by the elements made from R-KDP crystals. Hence, while designing these high-power lasers, operating at energy fluencies close to the damage thresholds of R-KDP crystals, it is important to understand the properties of laser induced absorbing defect states that have a negative influence on harmonic conversion efficiencies [42], laser induced damage threshold [43] and the overall system performance.

Present study is focused on the characterization of UV-induced transient absorption in R-KDP crystals. The tested crystals were grown by the Saint-Gobain Cristaux & Détecteurs Company in France and later-on cut and polished by Cleveland Crystals, Inc. These R-KDP

crystals have been chosen for the nonlinear optics applications in the high power laser facilities LIL[2] and LMJ at CEA-Cesta in Bordeaux, France [28, 44]. As properties of these crystals depend on the growth conditions and fabrication procedures that vary from vendor to vendor (there can even be variations in the individual crystal growth runs at the same producer), a critical application such as Laser Mégajoule (LMJ) requires exact parameter evaluation for crystals, grown by a particular producer.

2.2. KDP crystals and its defects (an overview)

2.2.1. KDP crystal structure

At room temperature, KDP crystals belong to the scalenohedral (twelve-sided polyhedron) class of tetragonal crystal system. Structure of this type of crystals has a point group $\bar{4}2m$ $(D_{2d} = V_d)$ and the space symmetry group $I\bar{4}2d$ with lattice constants a = 7.448 Å and c = 6.977 Å [45]. As the temperature is lowered below the T_C = 123 K (Curie temperature), KDP lattice undergoes polymorphic transition to the ferroelectric phase. This is a first-order phase transition and the crystal structure changes form tetragonal to orthorhombic with point group $mm2$ (C_{2v}) and space symmetry group $Fdd2$. In this case, lattice parameters are: a = 10.44 Å, b = 10.53 Å and c = 6.90 Å, whilst c being the ferroelectric axis. Due to their noncentrosymmetric lattice structure, KDP crystals also possess nonlinear optical[3] characteristics.

---

[2] The LIL (Laser Integration Line) facility is currently a 4-beam prototype of LMJ

[3] Note that noncentrosymmetric crystal lattice gives rise to nonzero elements in the second order susceptibility tensor, thus allowing second order nonlinear optical effects.

The structure of KDP crystal is shown in Figure 2.1 which was initially proposed by Stephenson *et al*. [46, 47]. There are 32 atoms in the primitive unit cell of KDP, and each unit cell is formed by four formula units. Each phosphorus ion in KDP is surrounded by four oxygen ions located at the vertices of a nearly regular tetrahedron (contracted along the *c* axis, by approximately 2%). These PO_4^{3-} tetrahedrals are arranged in every layer with a cubic arrangement (Layer structure in Figure 2.1) and each PO_4^{3-} group is linked tetrahedrally to four other PO_4^{3-} groups, spaced *c*/4 apart along the *c* axis, by hydrogen bonds of 2.48 Å length. These PO_4^{3-} groups are rotated 16º about the *c* axis and of the *a* axes[4] (Figure 2.1 a). The potassium ions merely have fixed positions in the crystal and together with the PO_4^{3-} groups are arranged in such a manner that potassium and phosphorus ions are spaced at a distance of *c*/2 along the *c* axis. The PO_4^{3-} tetrahedra are also connected by potassium ions. Each potassium ion is surrounded by eight oxygen ions with four of these oxygens belonging to tetrahedra of neighboring columns (Figure 2.1 b). One set of four oxygen ions lies closer to the potassium ion than the other quadruplet.

[4] Note that above the Curie temperature lattice constants of *a* and *b* are the same, thus sometimes both of these axes are being referred to as the *a* axes.

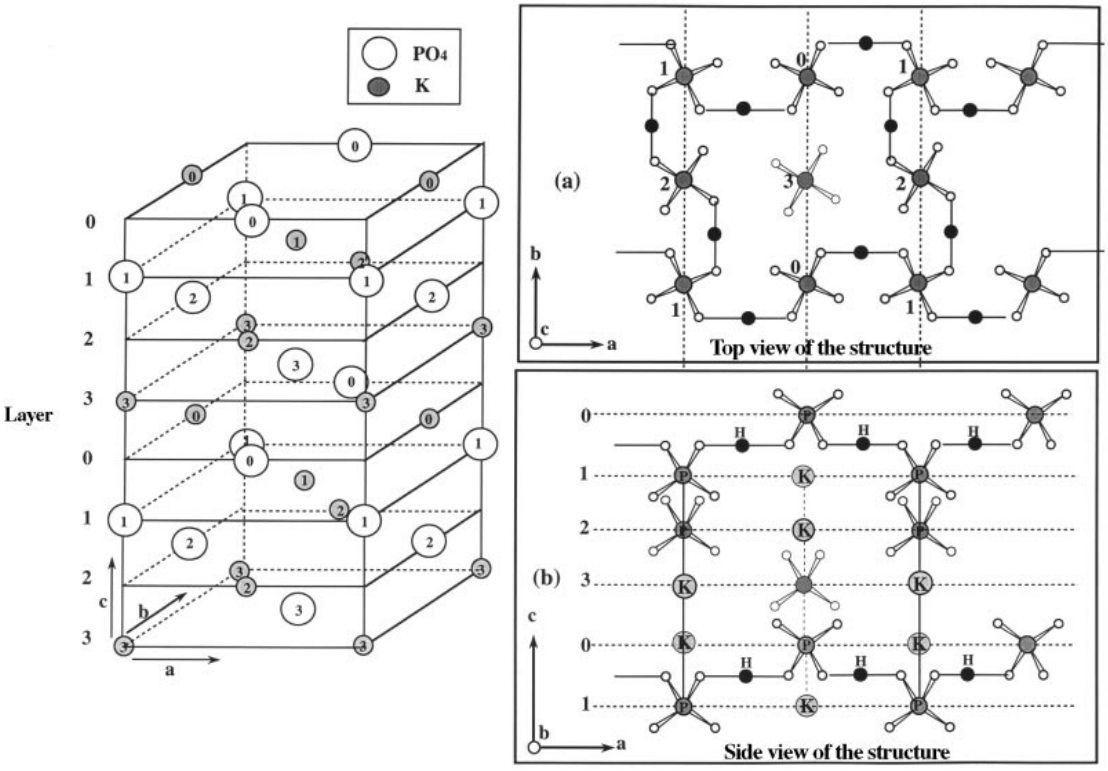

Figure 2.1 Structure of KDP crystal. (a) Projection along the *a* axis, (b) projection along the *c* axis (adapted from Ref. [48])

Hydrogen atoms in KDP crystal connect one upper and one lower oxygen atom of the neighboring PO_4^{3-} units that are positioned in the different layers (Figure 2.1 b). As a result, all hydrogen bonds lie in a plane nearly perpendicular to the *c* axis of the crystal. In the crystal's paraelectric phase hydrogen atoms do not have a well-defined or ordered positions relative to the overall crystal structure. A double potential well (Morse potential) for proton is symmetrically located about the center of the bond and allows the proton to be closer to the one of oxygen ions. At higher temperatures protons start tunneling between these two wells. Proton ordering occurs with the transformation to the ferroelectric phase, in such a way, that all the protons are located close to the PO_4^{3-} tetrahedra (in one of the wells), with every PO_4^{3-} unit attracting two protons. This proton ordering is also accompanied by the increase in the hydrogen bond length (up to 2.51 Å) and distortion of

PO_4^{3-} unit by movement of phosphorus ion along the *c* axis relative to its four oxygen counterparts. This movement of phosphor gives rise to spontaneous electric polarization along the *c* axis with direction matching that of the P atom displacement. A more detailed description of KDP structure in both phases can be found in Ref. [49].

2.2.2. Crystal growth

KDP-type crystals are usually grown from aqueous solution at near room temperatures by controlling five main growth parameters: supersaturation, pH of the solution, hydrodynamics of the crystallizer, temperature of growth and the content of impurity that actively keep the solution form spontaneous nucleation (see Ref. [50] and references therein). As KDP and DKDP crystals belong to the point symmetry group $\bar{4}2m$, they are faceted by the sets of $\{101\}$ (pyramidal) and $\{100\}$ (prismatic) faces[5].

[5] Note that $\{101\}$ notation refers to the whole family of pyramidal faces. In specific: (101), (011), $(\bar{1}01)$ and $(\bar{1}01)$. The same holds for the prismatic faces notation $\{100\}$.

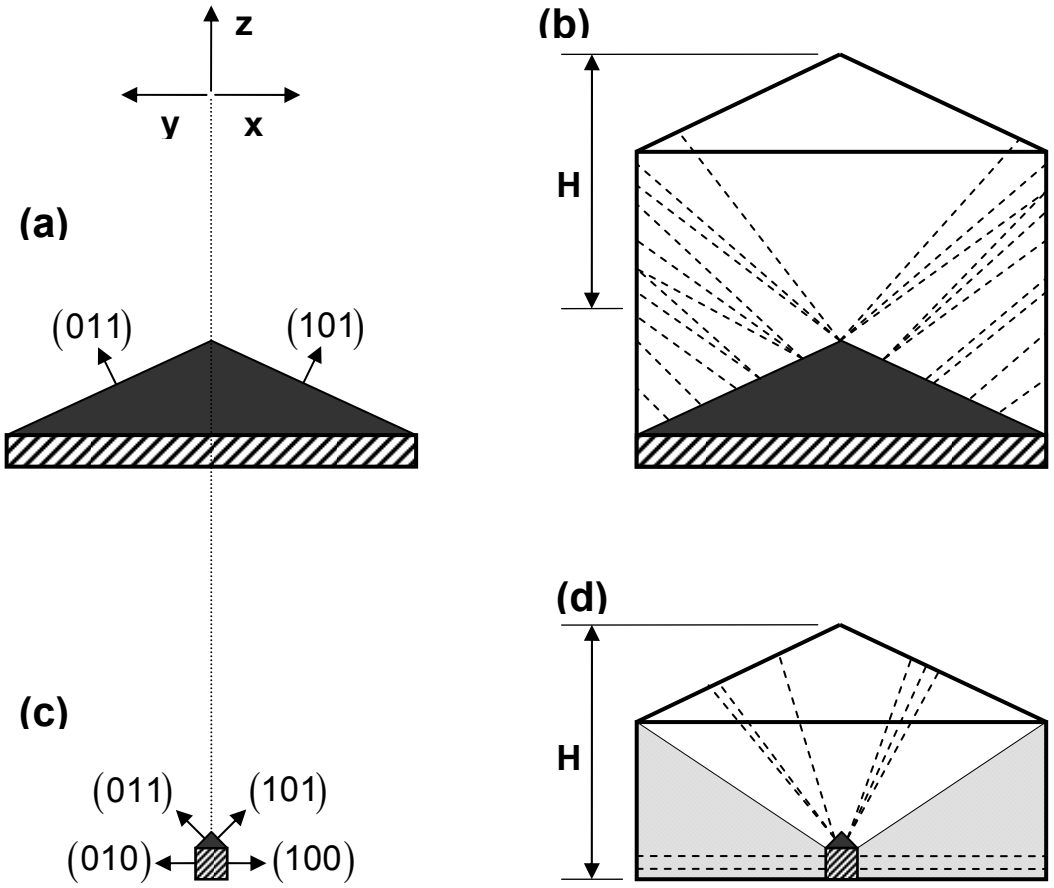

Figure 2.2 Schematic drawing of traditional crystal growth (a) and (b); and that of rapid crystal growth initiated by a point seed (c) and (d). Seeds with regenerated crystal caps are depicted on the left side (a) and (c), whilst the grown crystals, with the usable length H needed for cutting plates, are illustrated on the right side (b) and (d). Hatched regions – seeds; solid black regions – unusable regenerated seed caps; dashed lines – dislocations; light solid lines – sectorial boundaries between pyramidal (white regions) and prismatic (solid gray regions) sectors. Marked arrows show crystal growth directions. (011) and (101) expansion of pyramidal faces; (010) and (100) expansion of prismatic faces. (Partially reproduced from Ref [32])

Using the conventional crystal growth techniques, crystals are grown only in the $[001]$ direction by slow growth of the $\{101\}$ faces [22]. This phenomenon is dictated by the fact that at low supersaturation prismatic $\{100\}$ faces practically do not grow because of the blocking effect of trivalent metal ions like Fe^{3+} Cr^{3+} and Al^{3+} [51]. These metal ion impurities experience a large barrier for the adsorption onto the positively charged pyramidal $\{101\}$ faces [52], thus yielding their

selective accumulation on the prismatic $\{100\}$ faces and limiting crystal growth in this direction. Consequently, to achieve a desired size crystal by conventional techniques, the growth should start from a seed that has the same cross section as the final crystal (see (a) in Figure 2.2). This introduces a substantial difficulty into large-size crystal growth due to the complicated process of obtaining seeds with the required size and shape.

The method of crystal growth on a point seed avoids this difficulty. High supersaturation, in combination with extensive purification of the raw material, makes it possible to overcome the blocking effect of impurities and grow crystals uniformly on both prismatic $\{100\}$ and pyramidal $\{101\}$ faces. The final size of the crystal does not depend of the initial size of the seed (typically about 1 cm^3), which significantly simplifies the growth process. Additionally, it decreases the amount of dislocations in growing crystals. Typically the region occupied by the regenerated seed and its close vicinity has many structural defects, and often cannot be used for optical applications. This is especially pronounced in conventional crystals grown from large-size seeds, which give rise to a high number of dislocations. As Figure 2.2 shows, to obtain material with a low dislocation density, the final size of traditionally grown boule should be approximately twice as long as it is wide. The use of a point seed makes it possible to substantially decrease the size of the defective region and obtain crystals with low dislocation density. Besides, the length and weight of grown crystal is a factor of two smaller than that of the one grown by slow techniques for the same applications.

2.2.3. KDP defects

In this subsection the most important defects in KDP crystals are overviewed with the primary focus on the best studied ones with well defined physical models. Obviously, most of the attention is given to these defects that have direct implications on the optical properties of bulk crystal.

One of the first point defect to be identified [53-55] by the electron paramagnetic resonance (EPR) technique in x-ray and γ-ray irradiated KDP crystals at liquid nitrogen temperature (77 ºK) was the $\left[\mathrm{HP\dot{O}_4}\right]^-$ center, which was initially labeled the A radical. This defect consists of a hole localized at a single oxygen ion adjacent to a hydrogen vacancy. The regular KDP lattice contains K^+ ions and $\left(H_2PO_4\right)^-$ units while upon removal of a proton, a $\left(H_2PO_4\right)^-$ unit becomes $\left(HPO_4\right)^{2-}$ unit, which then easily stabilizes a hole and forms a paramagnetic $\left[\mathrm{HP\dot{O}_4}\right]^-$ center. The hole resides primarily on the oxygen ion next to the site of missing proton [55]. The absorption spectrum of A radical was initially measured in 1978 by McMillan *et al.* [56] but not only until the work of Chirila *et al.* [41] in 2003 was it unambiguosly ascribed to the $\left[\mathrm{HP\dot{O}_4}\right]^-$ center. Absorption spectrum of A radical comprises of one very wide band-like structure that covers almost entire UV-visible region, whilst stretching form 200 to 700 nm, with a maximum absorbance peaking at ca. 460 nm. From thermal annealing experiments on x-ray irradiated KDP crystals, it was determined that $\left[\mathrm{HP\dot{O}_4}\right]^-$ center is stable up to the crystal's Curie temperature, which in case of KDP is T_C = 123ºK.

A second hole-like center to be reported was the $\left[\mathrm{H_2P\dot{O}_4}\right]^0$ defect, which by some investigators is also called the B radical. This self-

trapped hole center is created under similar conditions as the above described proton vacancy hole center (i.e., exposure to ionizing radiation or high-power UV laser beam). A well established model for this defect is a hole trapped by $(H_2PO_4)^-$ group [56], where the hole is shared by two oxygen ions on one PO_4 unit in the otherwise perfect lattice [57]. Possible existence of such a defect in irradiated KDP had been postulated by early investigators [58, 59], but Wells *et al.* [60] were the first to precisely identify its structure. Absorption spectrum of radical B is similar to the one of radical A, it also exhibits a very broad absorption covering entire VIS range with two absorbance bands around 390 and 510 nm (In the case of DKDP crystal the second band is shifted to 550 nm.) [41, 58]. This double band structure discerns the radical B from its "cousin" or counterpart, radical A. Thermal decay of $\left[H_2P\dot{O}_4\right]^0$ defect was reported [59] to occur at temperatures around 70 K with the emission of thermoluminescence band with maximum at ~ 3.54 eV (350 nm) and a bandwidth of ~ 0.86 eV (~ 86 nm).

Another intrinsic defect of significant interest in KDP is the interstitial hydrogen atom H^0 (or deuterium atom in the case of DKDP). This is a trapped electron center which was recently identified [60, 61] by EPR technique in x-ray and UV-laser irradiated crystals. Absorbance of this defect lies in the middle-UV range with absorption band having the width of ca. 35 nm and centered around 230 nm [41]. This defect is relatively stable at liquid nitrogen temperature (77 ºK), whist at higher temperature it starts to decay and fully disappears when the temperature reaches ca. 200 ºK. The H^0 centers are the electron traps that complement the previously described $\left[HP\dot{O}_4\right]^-$ and $\left[H_2P\dot{O}_4\right]^0$ hole traps in irradiated KDP samples [61].

In addition to these "native" or intrinsic defects, Garces *et al.* in 2001 [62] have identified several new hole and electron traps in

undoped KDP. These traps are produced during the crystal growth in the form of structural defects, and after the irradiation of crystal they form defect centers by trapping produced electrons or holes. A distinct feature of these defect centers is that they are stable at room temperature. Specifically these investigators have identified the $\left[H_2Si\dot{O}_4\right]^-$ center, which consists of silicon impurity substituting for a phosphorus ion with a hole trapped on one of the adjacent oxygen ion, and $\left(PO_3\right)^{2-}$ electron trap, which itself is and oxygen vacancy with the trapped electron. In the case of the second trap, regular $\left(PO_4\right)^{3-}$ unit is replaced by a $\left(PO_3\right)^-$ unit during growth which then changes to a $\left(PO_3\right)^{2-}$ unit when it traps an electron, conceivably produced by ionizing radiation. These last centers were also investigated by Chirila *et al.* [41] and a relatively small amount of radiation-induced optical absorption between 400 and 200 nm was tentatively ascribed to these defects. The electronic structure calculations of the oxygen vacancy center showed [63] that its introduction in the KDP lattice causes a decrease in the band gap by approximately 1.9 eV.

Besides the intrinsic defects and the silicon impurity discussed above, which are believed to be present in all the KDP and DKDP crystals, there are other point defects like the transition metal ion impurities that can affect the optical properties of these crystals. In general, unless intentionally doped, most KDP crystals contain very small concentrations of transition-metal ions. Although direct evidence for the Fe^{3+} ion as a cause for UV absorption were not found [64], a strong correlation between even a trace amounts of metal ion impurities and the UV absorption in the 200÷300 nm range have been reported by numerous studies [65-67]. This impurity incorporation into the crystal is strongly dependent on the growth rate [68], consequently leading to the relative decrease of their concentration as the speed of growth

inceases. But crystals grown by the rapid-growth techniques expand not only in the pyramidal direction but also grow the prismatic sectors that have much higher concentrations of metal ion impurities (see section 2.2.2). This sectorial difference also translates into the different absorbance in the UV part of spectrum [39, 69, 70]

Recent investigations [38, 71] of inhomogeneities in KDP crystals by the means of fluorescence microscopy have led to the identification of fluorescent defect cluster in the bulk of the crystal. The concentration of these defects was found to be strongly dependent on the crystal growth speed; i.e., a change in growth rate from 1 to 8 mm/day have caused an increase in cluster density by a factor of 25 (from 10^4 to $2.5 \cdot 10^5$ per mm^3 [36]). Moreover, these defect clusters are unevenly distributed in different crystal sectors, with increased concentration in the prismatic part (see a in Figure 2.3). Although no accurate identifications of these defect species ware performed, it is likely that they represent a mechanism of compensation for the impurity incorporation during the crystal growth.

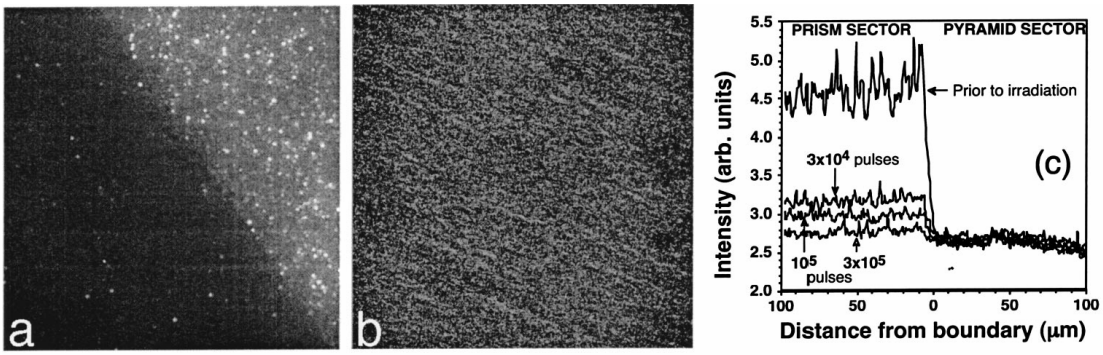

Figure 2.3 Images of the same 190×200 μm^2 section of the rapidly-grown KDP crystal at the boundary between prismatic (upper-right part of picture) and pyramidal (lower-left one) sectors using (a) fluorescence microscopy with 640-nm long-pass filter and (b) a light-scattering image. Both images obtained using 488-nm cw-laser illumination. (c) The digitized flourescence intensity profiles across sector boundary for different number of laser-conditioning pulses. (Adapted from Ref. [36])

The unique feature of R-KDP crystals is that under intense and continuous UV irradiation (355-nm ns-pulses at 1÷5 J/cm^2) the above described fluorescent defect clusters decrease their fluorescence output [36, 71]. That is the so called conditioning effect and it mainly affects the prismatic sector, where the concentration of these defects is biggest (see c in Figure 2.3).

2.2.4. UV-induced Transient absorption in KDP

As it was initially reported by Davis *et al.* [40], exposure of KDP crystals to the intense UV irradiation at room temperature causes a formation of a wide absorption band that covers entire 200-700 nm region and fully decays within the time scale of few seconds, leaving the sample optically transparent again. The same researchers have ascribed this absorption band to the formation and decay of $\left[\mathrm{HP\dot{O}_4}\right]^-$ center (the A radical, see section 2.2.3). According to their proposed model, two-photon absorption event is quickly followed by the transport of a proton or a hydrogen atom and the simultaneous formation of an $\left[\mathrm{HP\dot{O}_4}\right]^-$ center. This model was latter backed by additional EPR studies [61] where simultaneous observation of $\left[\mathrm{HP\dot{O}_4}\right]^-$ center and interstitial hydrogen atoms H^0, with comparable concentrations in the order of 10^{-18} cm^{-3}, was performed in the x-ray and 266-nm laser irradiated KDP crystals. Aside from these studies, subsequent investigators have also noticed that self-trapped hole center $\left[\mathrm{H_2P\dot{O}_4}\right]^0$ (the B radical see section 2.2.3) should be also produced under above mentioned circumstances and that it also has its input in the transient absorption spectrum [72, 73].

Marshal *et al.* [42] have also studied the UV-induced transient absorption in KDP. These latter investigators concentrated on the

determination of various parameters needed to characterize the phenomenon; whilst noticing, that depending on the particular sample under study, defect-state absorption decays over a wide variety of time scales, ranging form fractions of a second to even several days. This decay time did not appear to be correlated neither with the level of deuteration nor the concentration of chemical impurities. Surprisingly though, the temperature-dependence of decay rates had an Arrhenius-like behavior with a single activation energy of 0.51 ± 0.04 eV for all samples under study; hence leading to the conclusion that defect rate appears to be mediated by a diffusional process.

The following investigation focuses on the transient defects in KDP crystals grown by Saint-Gobain Cristaux & Détecteurs and intended to be used in the LIL and LMJ facilities.

2.3. Materials and methods

2.3.1. Investigated crystals

The material for the presented measurements is a rapidly-grown KDP (R-KDP) crystal. It was cut and polished by Cleveland Crystals Inc, with polishing performed by diamond-turned surfaces to meet the LIL standards. The crystal boule itself was grown by Saint-Gobain Cristaux & Détecteurs (boule No: A12), which is the primary supplier of R-KDP crystals to LIL and LMJ facilities. The investigated R-KDP sample had the following parameters:

Third harmonic generator crystal: type-II tripler cut crystal (Θ = 58º), 100×100 mm² in section and 10 mm in thickness. This crystal was cut from the prismatic sector of the boule. Reference number: PY5 01-0102.

In some measurements, for the purposes of reference, we have also used a conventionally grown KDP sample. This sample was cut at a similar angle (Θ = 58º) and had identical thickness of 10 mm (other dimensions: 15×15 mm^2)

2.3.2. Picosecond pump-probe setup

Time resolved spectroscopy method was used to investigate the formation of transient absorption in R-KDP crystals. A two color pump-probe setup depicted in Figure 2.4 was employed for this purpose. Transient coloration in R-KDP crystals was induced by the third harmonic (352 nm) of modelocked Nd:glass laser TWINKLE (Light conversion) that had 1.3 ps pulse duration and operated at 20 Hz repetition rate. The excitation beam was focused into the crystal with estimated peak intensity in the order of 100 GW/cm^2. The induced

absorption was measured by the tunable wavelength pulses from parametric amplifier TOPAS (Light Conversion), which itself was pumped by the second harmonic (527 nm) of the driving laser. The temporal resolution of our experiment was ~ 1 ps, and it was limited by the duration of the pulses in use.

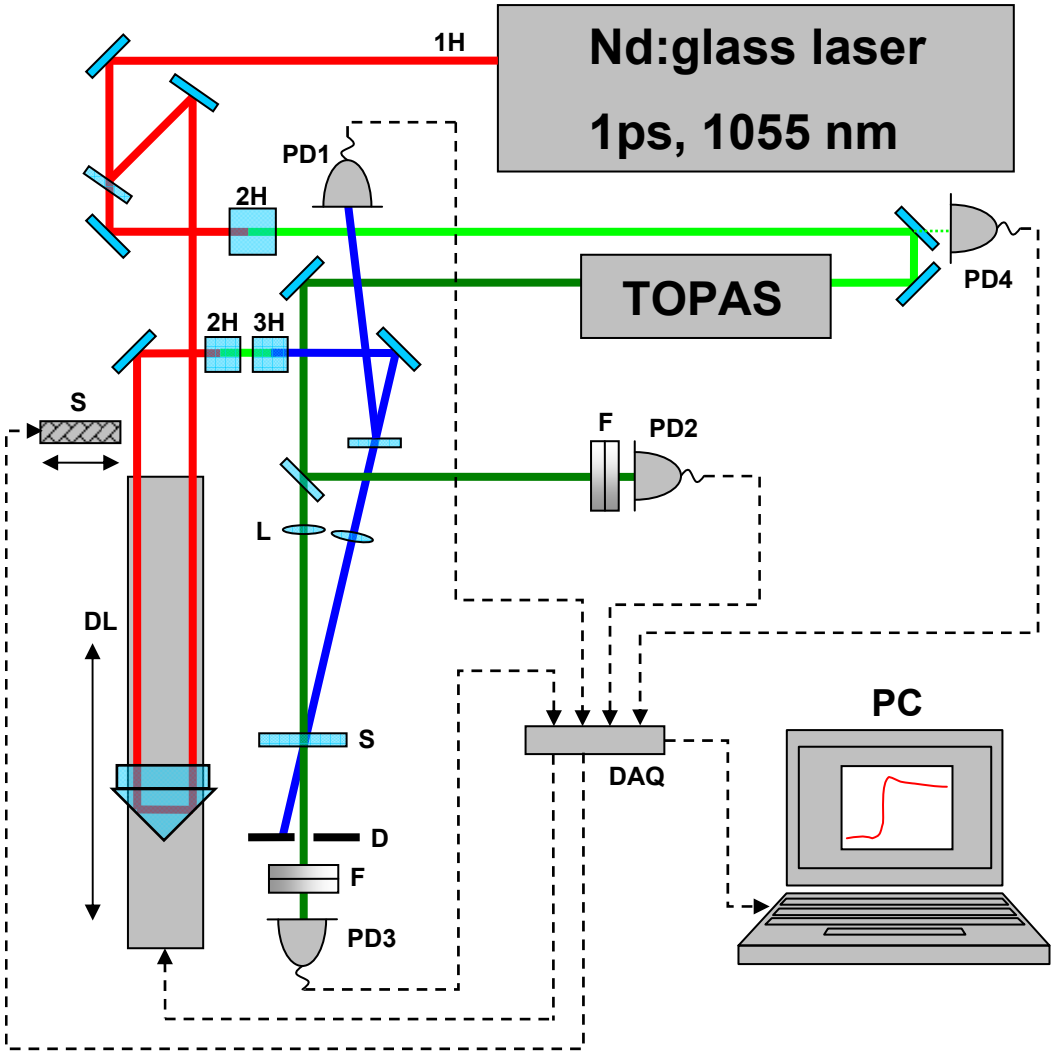

Figure 2.4 Optical layout of experimental setup used to measure induced absorption formation in R-KDP crystals. 2H and 3H – nonlinear crystals generating 2nd and 3rd harmonics; PD1, PD2, PD3 and PD4 – pump, reference, sample and synchronization photodiodes; DL – delay line; S – shutter; L – lenses; S – sample; D – iris diaphragm; F – neutral density filters; DAQ – data acquisition device; PC – personal computer.

Two photodiodes (PD2 and PD3) were used to measure optical transmission of the sample and additional photodiodes (PD1 and PD4)

were used to measure pump pulse energy and to synchronize the data acquisition system (DAQ). In order to get the absolute values of absorption change, computer-controlled shutter was placed into the path of pump beam and the ratio between signals coming form sample and reference photodiodes was measured at the open and closed shutter positions. A single data point was calculated by averaging approximately 50 to 100 shots. Temporal delay between pump and probe pulses was induced by translating the retroreflector prism that was mounted on the computer-controlled linear stage. Personal computer (PC) was used for online control of the experiment (shutter, delay line and parametric amplifier) and the data acquisition.

2.3.3. Long-lived defect decay detection system

To investigate the decay time of UV-induced transient absorption in R-KDP crystals we have used the setup presented in Figure 2.5. The samples were excited using a third or fourth harmonics (355 nm, 266 nm) of Q-switched Nd:YAG laser (NL301G, EKSPLA). This laser delivered up to 46 mJ pulses at the 355 nm or 8 mJ at the 266 nm, whilst the pulse durations was around 4-5 ns. Laser repetition rate was set to 1 Hz, and, in combination with laser-synchronized and computer-controlled shutter, this gave us a possibility to have a single excitation pulse on demand. For the probing, we used a second harmonic (535 nm) output of Q-switched diode-pumped Nd:YVO_4 laser (NL640, EKSPLA), with the repetition rate of 1 kHz. The induced absorption dynamics was monitored by measuring transmission changes from pulse to pulse. Given the probe laser's repetition rate, this yielded a temporal resolution of 1 ms. Before the sample, probe pulse energy was attenuated to the minimum (~ 2 nJ) in order to decrease, as much as possible, its influence on the measured kinetics. Incident and transmitted pulse energy was monitored by reference and sample

photodiodes (Hamamatsu S1337), while the third photodiode measured the energy of the single pump pulse. Pump and probe beams were spatially matched in the sample and focused to spots with diameters of ~ 400 μm and 200 μm, respectively.

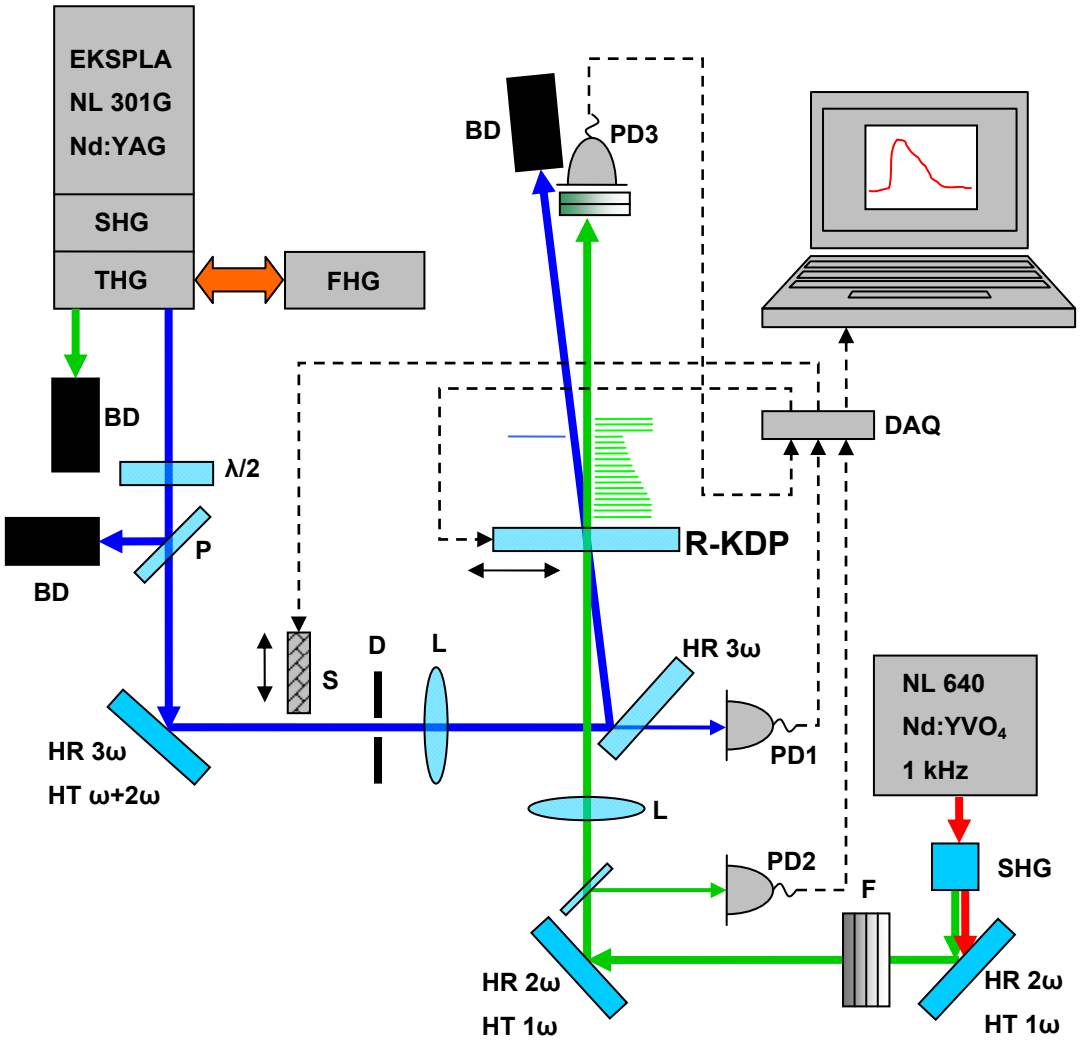

Figure 2.5 Optical layout of experimental setup used to measure UV-induced transient absorption decay in R-KDP crystals. SHG, THG and FHG – laser modules generating 2nd, 3rd and 4th harmonics; PD1 – photodiode monitoring pump energy; PD2 and PD3 – reference and sample photodiodes; λ/2 – wave plate; P – polarizer; BD – beam dumps; S – shutter; D – diaphragm; L – lenses; F – neutral density filters; DAQ – data acquisition device; PC – personal computer.

Computer-controlled λ/2 wave plate and dielectric polarizer ware used as variable attenuator for the pump energy. In order to eliminate the accumulation of long-living defect states, with life-times in excess of

10 s (that is a typical duration of our single shot measurement), and to acquire a better statistics over the crystal, our sample was translated to a different location for every excitation shot. A typical dataset consisted of 50 averaged kinetic traces, whilst the procedure of averaging also incorporated a correction for the fluctuations in pump's energy. Polarization of pump and probe radiation was linear and perpendicular to each other. Although transient defects under our experimental condition do not show any noticeable dichroism [40, 42], the following polarization configuration was chosen in order to exactly simulate the third harmonic generation[6] process in R-KDP crystal and to explicate the influence of UV-induced defects in ICF drivers.

2.3.4. Setup for evaluation of TPA coefficient

To determent the two-photon absorption (TPA) coefficient in R-KDP crystal we have performed an intensity dependant transmission measurement [74] using a setup presented in Figure 2.6. We have used a commercial femtosecond laser system SpitFire (Spectra Physics) that delivered ~ 130 fs pulses. Laser wavelength was tuned to 355 nm by an OPA Topas (Light Conversion) to match with the one of preceding measurements and be close to the main operating wavelength of ICF drivers. The beam was loosely focused by a lens L and sample was positioned into the diverging beam, away from the waist. Beam diameter at the sample was measured with a CCD beam profiler and was 293 μm (FWHM). Within the sample length (1 cm) this diameter varied only by ± 5 μm, thus in the further estimation of TPA coefficient, we have assumed that our beam was collimated. Pulse energy was varied by means of λ/2 wave plate and polarizer with the maximum

[6] Note that the sample crystal itself did not generate any radiation during our experiments.

value of ~ 8 μJ. This limit for the pulse energy and proportionately peak intensity was caused by the threshold for continuum generation. A second λ/2 wave plate was used to additionally rotate the polarization with respect to the crystal axes (i.e. *o* or *e* polarization). Repetition rate of the laser system was reduced to 1 Hz in order to decrease the influence of transient defect accumulation on the intensity dependent transmission. We estimate that under above described conditions, the contribution of UV-induced defect accumulation to the overall change in transmission would be ca. $2 \cdot 10^{-4}$. The transmission itself was measured with Laserstar (Ophir) power meter and two detector heads (PE and PD) were used in order to eliminate possible laser power fluctuations. Energy dependent ratio between the two channels was recorded with and without the sample; whilst one data point was typically averaged from 10^3 laser shots.

The TPA coefficient was determined by fitting intensity-dependent energy transmission by a standard procedure [75]:

$$T = \frac{E_{out}}{E_{in}} = \frac{\int_0^{\infty}\int_{-\infty}^{\infty} I_{in}(r,t)\cdot dt \cdot 2\pi r dr}{\int_0^{\infty}\int_{-\infty}^{\infty} I_{out}(r,t)\cdot dt \cdot 2\pi r dr}, \qquad (2.1)$$

where $I_{in}(r,t)$ and $I_{out}(r,t)$ are the intensities of incident and transmitted radiation given in polar coordinates. The incident and transmitted [74] intensity in the case of Gaussian pulse with a Gaussian spatial profile are:

$$I_{in} = I_0 \exp\left\{2\ln(4)\left[-(t/\tau)^2 - (r/d)^2\right]\right\}, \qquad (2.2)$$

$$I_{out} = \frac{I_0(1-R)^2 \exp\left\{2\ln(4)\left[-(t/\tau)^2 - (r/d)^2\right]\right\} e^{-\alpha L}}{1 + \beta I_0 (1-R)\exp\left\{2\ln(4)\left[-(t/\tau)^2 - (r/d)^2\right]\right\}\left(1-e^{-\alpha L}\right)}. \qquad (2.3)$$

Here τ and d are the pulse width and the beam radius (both defined at FWHM); α and L are the linear absorption and sample length, β – TPA coefficient, R – reflection coefficient and I_0 – maximum on-axis intensity that according to our definitions can be expressed as:

$$\mathrm{I}_0 = \left(\frac{2\ln(4)}{\pi}\right)^{3/2} \frac{\mathrm{E}}{\tau \mathrm{d}^2}, \tag{2.4}$$

whrere E is the pulse energy. After the integration of Eq. (2.1), the intensity-dependent transmission is expressed as:

$$\mathrm{T} = \frac{(1-\mathrm{R})\mathrm{e}^{-\alpha \mathrm{L}}\alpha}{\sqrt{\pi}\beta \mathrm{I}_0\left[1-\mathrm{e}^{-\alpha \mathrm{L}}\right]} \int_{-\infty}^{\infty} \ln\left\{1+\beta(1-\mathrm{R})\mathrm{I}_0\left[\frac{1-\mathrm{e}^{-\alpha \mathrm{L}}}{\alpha}\right]\mathrm{e}^{-\mathrm{t}^2}\right\}\mathrm{dt} \tag{2.5}$$

This function was numerically fitted onto the experimental data with only one free variable β

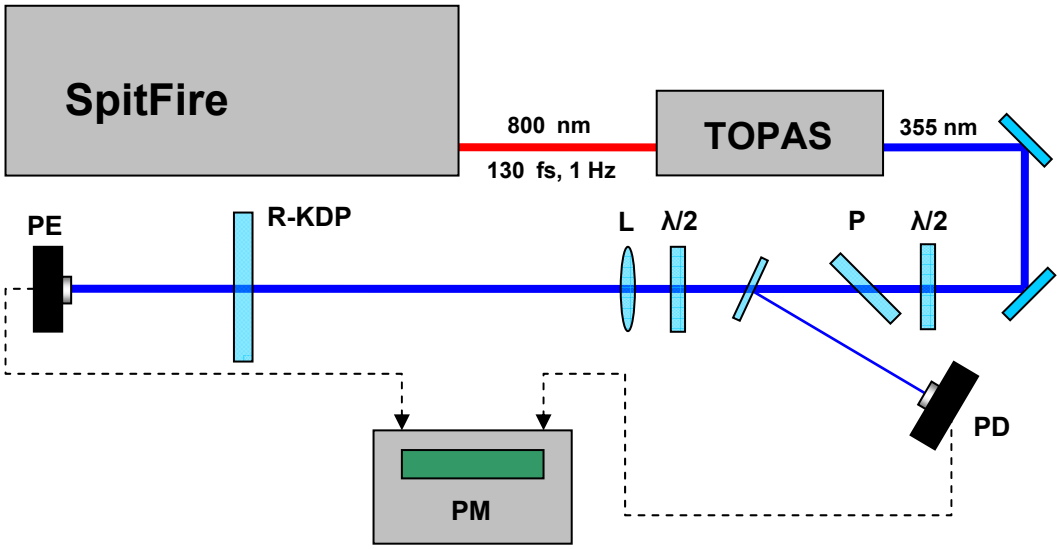

Figure 2.6 Experimental setup for the measurement of absolute two-photon absorption coefficient values. λ/2 – wave plates; P - polarizer; L – lens; R-KDP – sample crystal; PE – piroelectric head; PD – photodiode head; PM – power meter;

2.4. Results and discussion

The necessity to perform a detailed characterization of UV-induced defects in R-KDP crystals was driven by the work of Marshal *et al.* [42], where it was shown that defect relaxation times in (D)KDP crystals strongly varies from sample to sample, and attempts to uncover the correlations between these decay times and any external crystal parameter or impurity concentration have failed. Note, that the majority of studies dedicated to investigate defect formation and decay in hydrogen bonded solids (like KDP) were performed with 266-nm laser excitation. In contrast to that, almost all the experiments described in this section, with the exception of laser conditioning studies, were done with the lasers operating at wavelengths that matched, or almost matched, with the third harmonic of Nd:glass laser. This choice yielded considerably weaker signals and additional struggle during alignment, but the main objective of this study was to characterize transient defects with laser parameters (i.e. wavelength, pulse duration, energy density and orientation of polarization) similar those of ICF drivers [28].

2.4.1. Investigation of defect formation in R-KDP

To investigate the formation of transient defect states, we have performed a picosecond pump-probe experiments on R-KDP crystal using the setup described earlier (section 2.3.2). In the spectral range of 450-600 nm, we have observed an increase in sample absorption by ca. 2 mOD and a typical trace from these measurements is presented in Figure 2.7.

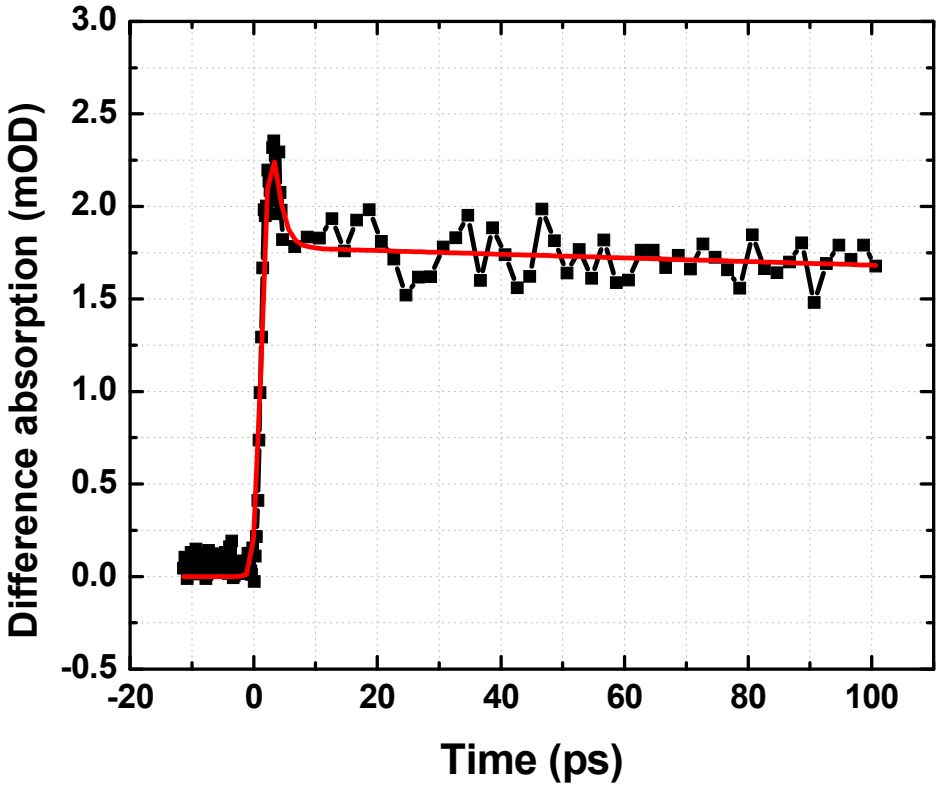

Figure 2.7 Trace of time-resolved pump-probe experiment in R-KDP crystal at 520 nm probe wavelength. Red line is the double-exponent decay fit on collected data.

Here we see a steep absorption increase immediately after the excitation, which is followed by almost steady signal in the picosecond time domain. Small and fast signal decrease is also present at the zero delay. We have fitted collected data with a double-exponent decay function, whilst the time constant of the first decay was set to the instrument response of our experiment (1.3 ps). It can be clearly seen that the fit adequately represents the measured data and given the high pump pulse's intensity, we think that initial decrease in absorption could be ascribed to the cross phase modulation or some other coherent phenomenon that appears at the moment of temporal pulse overlap. Unfortunately, we can not deduce the exact defect formation time from our measurements but it should be close to (or shorter than) the IRF of our experiment. Having in mind the earlier reported [40] defect formation time in KDP crystal (1.6±0.4 ps), we could say that defect

formation time in our R-KDP crystal is at least as short as the one of KDP. The major part of induced absorption exhibits relatively long lifetime which is hard to evaluate from our measurements, due to a lack of data at further delays. In addition, the 20 Hz repetition rate of our driving laser system did not enable us to detect the light-induced centers with the lifetimes longer than 50 ms. If those longer living centers appeared (which probably was the case), their equilibrium concentration was reached. This concentration is determined by the average rates of defect creation and bleach/decay, consequently leaving them “invisible” in such a measurement scheme.

2.4.2. Defect-state decay

To gain a better understanding on the UV-induced defect decay, we have concentrated on measuring the full decay kinetics. For this purpose, we have built the setup described in section 2.3.3 and measured typical induced absorption decay traces for R-KDP that are presented in Figure 2.8 (A). Every single trace in this picture is an average of 50 distinct measurements at various spots in the crystal. Additionally, we have also performed measurements[7] on a ‘reference’ slowly grown KDP sample (B in Figure 2.8). As it is evident from the presented data, the transient absorption dynamics is non-exponential and complex. We have tried to fit these kinetics with different model functions, like the one for thermally activated diffusion-limited recombination of particle pairs [76] assumed by Davis *et al.* [40] or interdefect tunneling recombination proposed by Ogorodnikov *et al.* [72], but neither one gave a reasonable fit for the entire kinetic. Thus in

[7] Note that only measurement for *o* polarization is presented because signal in the case of *e* polarization was too weak and it was impossible to extract reliable trace.

our further analysis we have decided to use a multi-exponential function with three decaying components, the smallest number that yielded an adequate fit. Table 2.1 summarizes the fitted parameters; note that traces of R-KDP sample were fitted globally using the same set of time parameters for both polarizations.

The first eye catching thing, once comparing R-KDP traces with the one of KDP, is that conventionally-grown crystal has much longer final defect relaxation time. Indeed, transient absorption in large aperture crystal practically disappears in ca. 6 s, while in the case of reference sample the third decay parameter is ca. 40 s. This large difference in decay rates reproduces the results reported by other investigators [42], and is in line with their suggestion that final defect decay time is governed by the concentration of imperfections or traps, which is expected to be higher in rapidly grown crystals [68]. This seemingly increases the number of recombination channels and leads to shorter defect lifetimes.

Another result evident in Figure 2.8 (A) is that the absolute induced absorption change is polarization dependent (i.e. it is some 2 times larger for the *o* polarization then for *e* one). Note that the excitation conditions were identical and the only difference was the orientation of polarized laser light relative to the crystal axis. According to the model proposed by Davis *et al.* [40], UV laser induced two-photon absorption creates electrons and holes in KDP lattice and subsequently some of them get trapped at nearby defect sites and form VIS absorbing centers. Thus, in order to explain a polarization dependent concentration of absorbing defects states, either two-photon absorption or defect formation probability should depend on the crystal orientation.

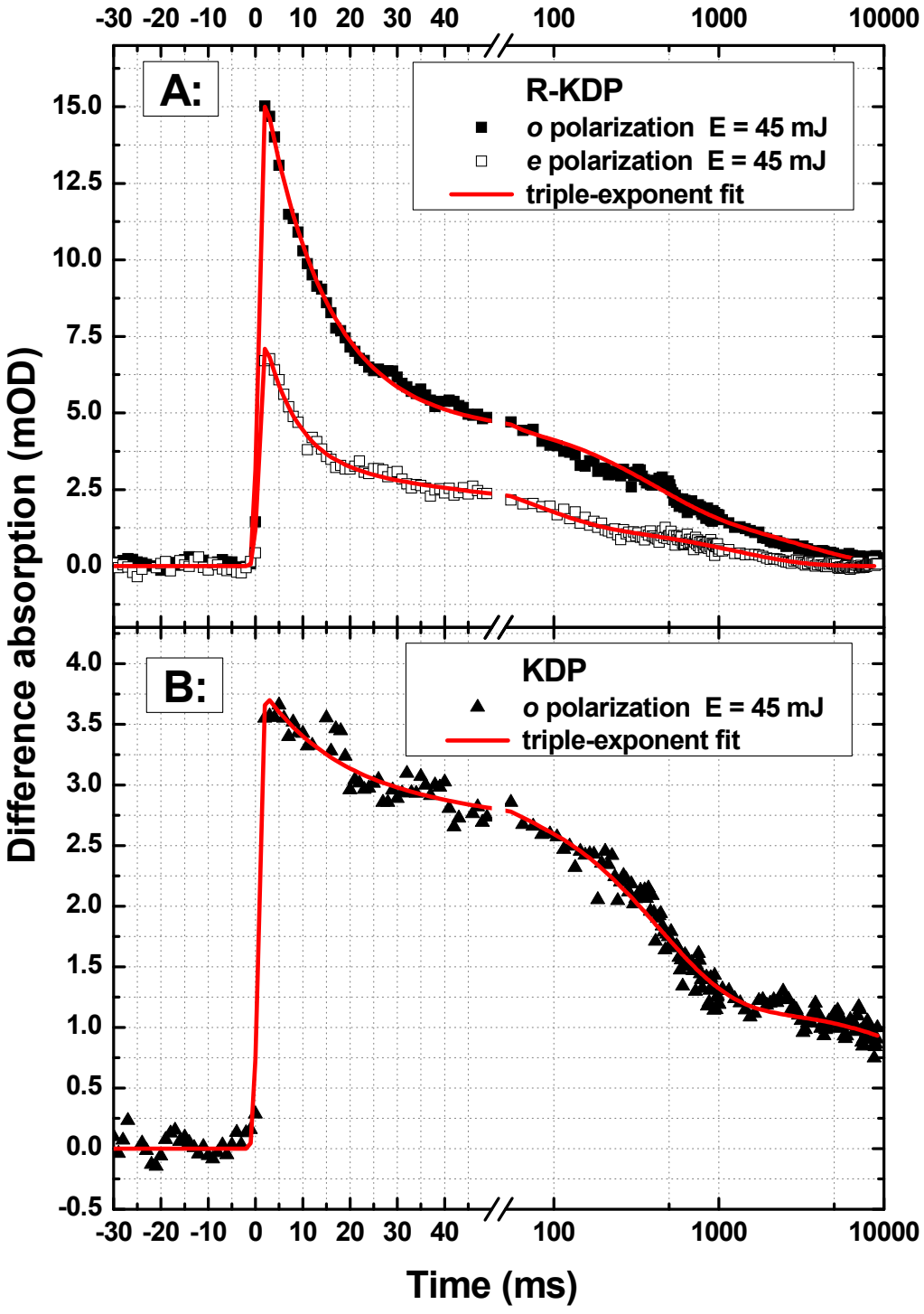

Figure 2.8 Representative decays obtained from time-resolved transient absorption experiments performed on R-KDP (A, upper panel) and KDP (B, lower panel) samples. Filled squares and triangles are measured data with *o* polarized pump, while hollow squares are points collected with *e* polarized pump. Red lines are triple-exponent decay fits. Note the log scale after the brake.

Table 2.1 Fitted parameters of multi-exponential defect decay.

Crystal	A_1, mOD	τ_1, ms	A_2, mOD	τ_2, ms	A_3, mOD	τ_3, ms
R-KDP *o* polarization	4.5 ± 0.1	11.5 ± 0.3	1.6 ± 0.1	160 ± 10	1.0 ± 0.05	2 000 ± 80
R-KDP *e* polarization	11 ± 0.1	11.5 ± 0.3	2.7 ± 0.1	160 ± 10	2.8 ± 0.1	2 000 ± 80
KDP *o* polarization	0.83 ± 0.06	16 ± 2.6	1.7 ± 0.1	435 ± 25	1.1 ± 0.05	40 000 ± 8 000

Alternatively, it is also well known (see section 2.2.2) what (R-)KDP crystals possess some linear absorption in the UV part of spectrum, which could in principle lead to formation of additional excitation through cascade absorption. Since this linear absorbance is polarization dependent [45], this would also translate into supplementary anisotropy of created defect centers. However, according our earlier reported [77] values of linear absorption in the similar R-KDP crystal, this absorption has a very small polarization variance and that of different sign than induced defect absorption (to be precise, absorption for *o* polarization was some 7 % smaller then that for *e* one). Thus we could tentatively conclude that linear absorption does not have any considerable influence to transient defect formation in our sample.

2.4.3. Determination of absolute two-photon absorption coefficients

Further search for the cause of polarization dependent defect concentrations has led us to the measurements of absolute two-photon absorption (TPA) values for R-KDP. The setup used for this purpose is briefly described in section 2.3.4. The choice of femtosecond laser for TPA measurements was driven by the intent to minimize the influence of generated defect states on the overall TPA value. The results of this experiment are presented in Figure 2.9. The collected data was

numerically fitted with the function presented in Eq. (2.5), where reflection coefficients R_o and R_e were calculated from Sellmeier equations [45] by assuming the normal incidence angle, and liner absorption coefficient α estimated from low intensity transmission data.

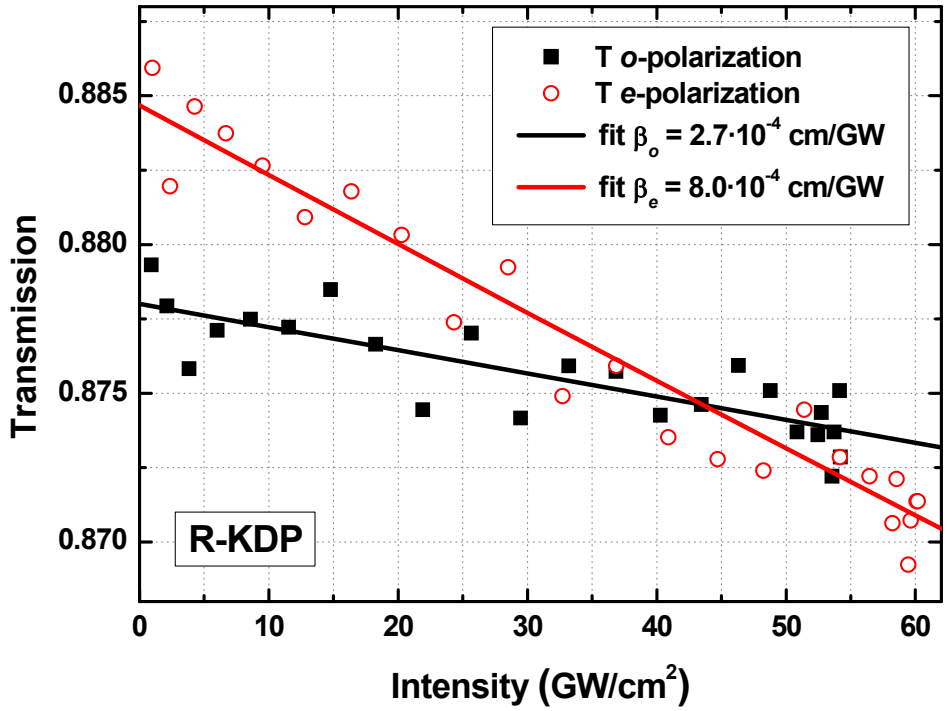

Figure 2.9 Intensity dependent transmission curves for R-KDP crystal measured at 355 nm. Filled squares and hollow circles are measured data for *o* and *e* polarizations, respectively. Solid curves are the best numerical fits.

Figure 2.9 clearly shows that TPA possesses a polarization dependency with fitted coefficients: $\beta_o = (2.7\pm0.5)\cdot10^{-4}$ cm/GW and $\beta_e = (8.0\pm1.0)\cdot10^{-4}$ cm/GW. Although other investigators [78, 79] did not observe any anisotropy of the TPA in KDP crystals, their reported values were determined with lasers operating at 211-264 nm wavelength range. Having in mind, that absorption edge (defined as decrease in transmission by 50 %) in KDP was determined [80] to be 176 nm, it would be conceivable to say that our measurements at 355 nm wavelength probes the edge of TPA. In principle, the band gap energy can vary depending on the crystal orientation, and hence the TPA value could also exhibit anisotropy. The only study, that we are

aware of, which reported the TPA values in KDP at 355 nm wavelength is by Lui *et al.* [74]. Unfortunately, these investigators did not performed polarization dependant measurements and reported only a single value of $\beta = 5.9 \cdot 10^{-3}$ cm/GW. This value is an order of magnitude larger than the one that we have determined. The source of this discrepancy is most likely the difference in the used laser pulse durations. Lui *et al.* have use laser pulses with the duration of 30 ps and their measurements could have been susceptive to the absorption of transient defects that are formed in > 1 ps (see section 2.4.1 and [40]), hence 'increasing' the value of TPA coefficient. Alternatively performing such measurements at high repetition rates, even though using a femtosecond pulses, would also increase TPA value due to defect accumulation, and, since defect decay and bleaching should not be dependent on crystal orientation, liftoff the anisotropy.

Returning to the question of source for anisotropy in induced absorption changes we could conclude that this anisotropy originates from TPA process and not from subsequent defect formation. This deduction is also supported by the notion that characteristic duration of electronic polarization dephasing (T_2) in solids lies in the 10^{-15} s range and defect formation time is around 1 ps (see above). We also note that these measurements of TPA and transient defect absorption directly correlate with our earlier report [81] of light induced damage threshold measurements for the same crystal[8] and with corresponding laser wavelength. Specifically, the multi-pulse damage thresholds measured for the *o*-polarization were significantly lower then for the *e*-one.

[8] These investigations were part of throughout characterization of this R-KDP crystal.

2.4.4. Characterization of defect formation and bleach

In order to deduce, in the parameterized manner, functional dependence that would allow us predicting transient defect absorption in our R-KDP sample, we have performed energy dependant kinetic trace measurements for both crystal polarizations with the setup described in section 2.3.3. The measurement results are summarized in Figure 2.10. Here the sum of amplitudes from the triple-exponent fit is plotted as a function of pump fluence. This sum expresses the overall defect-state absorption immediately after the excitation.

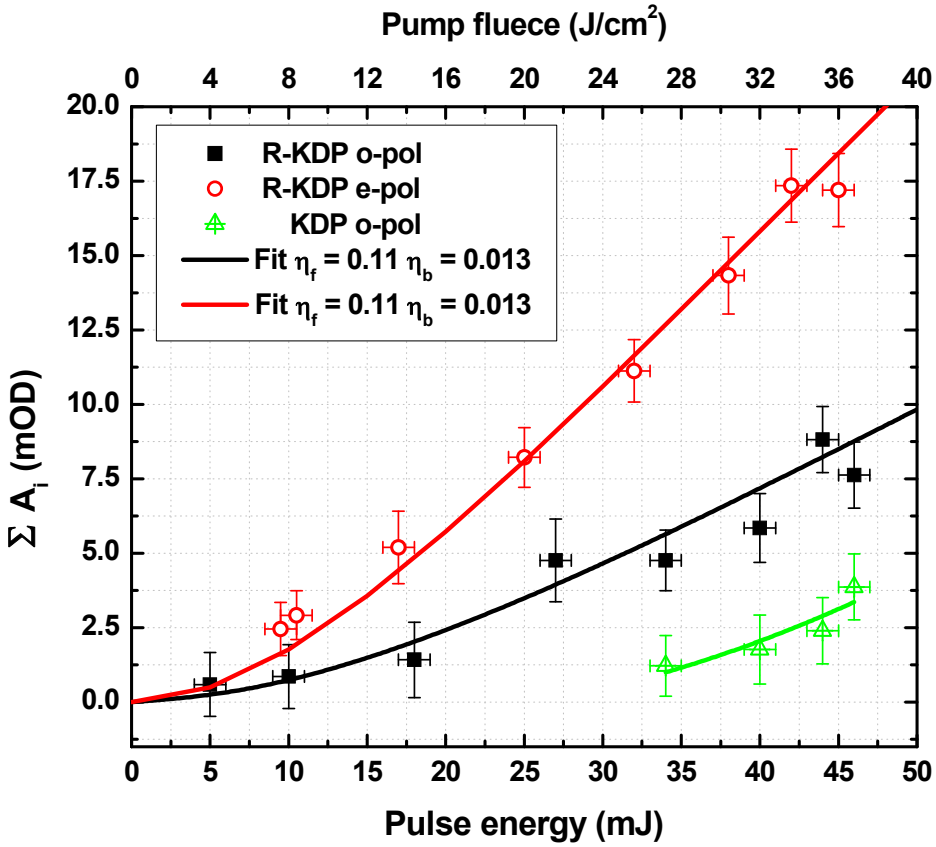

Figure 2.10 Fluence dependence of transient absorption strength, expressed by the sum of amplitudes from the triple-exponent fit on measured kinetics. Filled squares, hollow circles and crossed triangles are measured data at *o* and *e* polarizations of R-KDP and *o* polarization of KDP, respectively. Black and red solid curves are fits using a function presented in Eq. (2.9). Green curve – is provided to guide the eye.

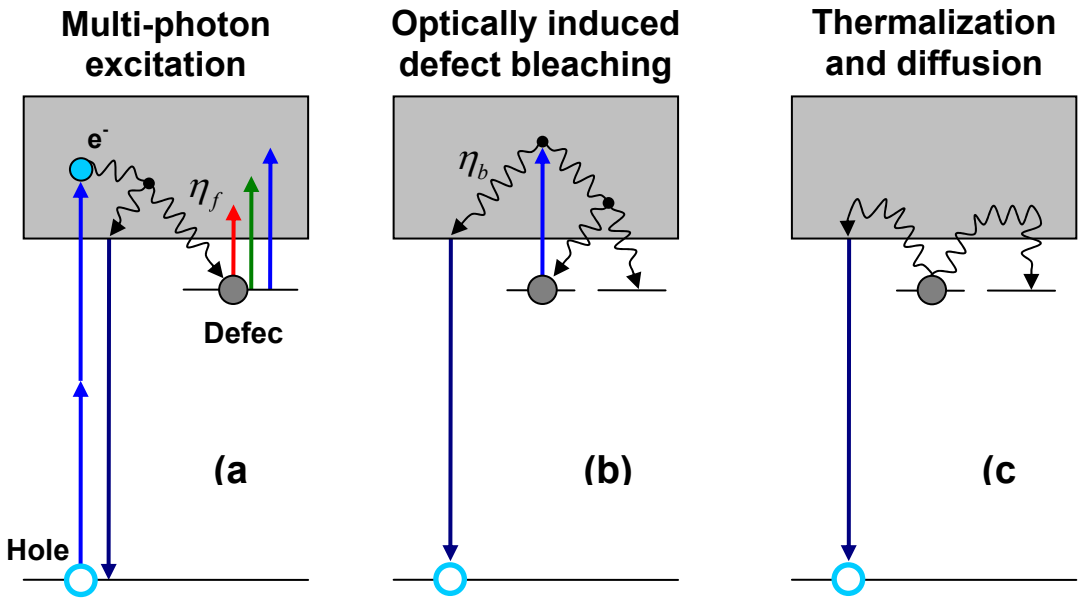

Figure 2.11 Diagram depicting transient absorption phenomena in KDP. (a) Two-photon absorption generating an absorbing defect with an efficiency η_f. (b) Optically induced defect bleaching process with an efficiency of η_b. (c) Thermal defect bleaching process leading to decay recombination and consequent decay of transient absorption or diffusion governed defect migration to neighboring site. (Reproduced from Ref. [42].)

To fit these optical absorption dependencies on the UV-pulse energy we have adapted to our experimental conditions a phenomenological model proposed by Marshal *et al.* [42]. This model is summarized in Figure 2.11. The initial step of this model is TPA initiated promotion of electron to the conduction band of the crystal, which then can either rapidly recombine with its geminate hole or interact with the lattice and generate an absorbing defect state with a formation efficiency of η_f (Figure 2.11 a). Subsequently, this absorbing defect can be re-excited and return to its original or neighboring defect state, or can recombine with an effective bleaching efficiency of η_b (Figure 2.11 b). This possibility of optical defect state bleaching was already observed by the early investigators [56]. When no additional light is incident upon the sample, the defect-state population can decay by thermal activation of the electron into the conduction band and its

subsequent recombination (Figure 2.11 c). Note that due to the fact that these UV-induced defects have substantial linear absorption in the blue part of the spectrum [40], they can also be bleached by the same UV-pulse that generated them.

The general differential equation governing the defect density N according to the model described above is:

$$\frac{dN(z,t)}{dt} = \frac{\eta_f \beta I_{3\omega}^2(z,t)}{6\hbar\omega} - \frac{N(z,t)\eta_b \sigma_{3\omega} I_{3\omega}(z,t)}{3\hbar\omega}, \tag{2.6}$$

with an initial condition of:

$$N(z, t=-\infty) = 0, \tag{2.7}$$

where z, β, η_f, η_b, $\sigma_{3\omega}$ and $\hbar\omega$ are the depth in the crystal, the TPA coefficient, the defect-formation probability, the defect bleaching probability, the defect absorption cross section, and the fundamental photon energy of Nd:YAG, respectively. In Eq. (2.6) the first and the second terms of the right-hand side describe defect formation by TPA and destruction or bleaching by linear absorption, respectively. In the general case, laser intensity and consequently defect density are quantities dependent of propagated crystal length (noted by z the in brackets). But as our pump beam is relatively weakly affected by TPA and defect-state induced absorption (see sections 2.4.2 and 2.4.3) we can assume the absence of pump depletion, thus the z dependences can be ignored. For the temporally square pump pulse of length τ and intensity $I_{3\omega}^0$ the solution for this equation is:

$$N(z,t) = \frac{\eta_f \beta I_{3\omega}^0}{2\eta_b \sigma_{3\omega}} \left[1 - \exp\left(\frac{-\eta_b \sigma_{3\omega} I_{3\omega}^0 t}{3\hbar\omega} \right) \right]. \tag{2.8}$$

The optical density (defined as the logarithm of reciprocal normalized transmission) measured at the output face of the crystal $z = d$, can be obtained by multiplication of $N(d,\tau)$ by both the appropriate probe absorption cross section σ_p and the crystal

thickness d. The optical density at ω_p (532 nm in our configuration) for a subsequent probe beam is:

$$OD(\tau) = \frac{N(d,\tau)\sigma_p d}{\ln(10)} = \frac{\eta_f \sigma_p \beta I_{3\omega}^0 d}{\eta_b \sigma_{3\omega} 2\ln(10)} \left[1 - \exp\left(\frac{-\eta_b \sigma_{3\omega} I_{3\omega}^0 \tau}{3\hbar\omega} \right) \right]. \quad (2.9)$$

This later function was used to globally fit the curves presented in Figure 2.10. The only variable parameters were defect formation η_f and bleach η_b probabilities. Note that the difference between *o* and *e* polarization functions were only in different β (see section 2.4.3) and $\sigma_{3\omega}$ (see polarization dependent defect absorption spectrum reported in Ref. [40]) coefficients. All the parameter values are summarized in the Table 2.2.

Table 2.2 Parameter use to model transient defect absorption strength.

	β (cm/GW)	η_f	η_b	$\sigma_{3\omega}$ (cm^2) *	σ_p (cm^2) **	τ (ns)	d (cm)
o pol.	$2.7\cdot10^{-4}$	0.11	0.013	$1.9\cdot10^{-18}$	$4.6\cdot10^{-18}$	4.5	1.0
e pol.	$8.0\cdot10^{-4}$			$2.6\cdot10^{-18}$			

* relative values to σ_p estimated from the spectrum presented in Ref. [40]

** Ref. [42]

To test the validity of our model function and fitted parameters, we have estimated the induced defect absorption in the configuration of our picosecond pump-probe experiment. While using the Eq. (2.9) with 1.3 ps pulse duration, 0.13 J/cm^2 pump fluence (see section 2.3.2) and other parameters for *e* polarization from Table 2.2, we arrive at the absorption value of 2 mOD, which is in good agreement with the measurement presented in Figure 2.7. We also note that this absorption estimation should be valid for the laser pulses with durations down to a few picoseconds; as for the shorter pulses, it could be that the bleaching probability should be set to zero due to the non-instantaneous defect formation mechanism (see section 2.4.1).

To conclude, we have characterized the formation and decay of transient defect-states in R-KDP crystal to be used in large aperture lasers. We also present a set of parameters (Table 2.1 and Table 2.2) that can be used to successfully predict the defect induced absorption in tripler crystals of ICF drivers.

2.4.5. Influence of laser conditioning

We have also investigated the influence of UV-laser conditioning on the UV-induced defect decay kinetics. This study was driven by the idea that since the nature of defect decay in KDP is governed by thermally activated diffusion process, as proposed by Davis *et al*. [40], diffusion of either trapped holes, protons or even electrons, should be sensitive to the local changes in crystal structure. A certain structural change, specifically the reduction in number of fluorescent defect clusters, was reported by Demos *et al*. [36] to occur under intense and repetitive UV-laser irradiation, exclusively in the prismatic sectors of R-KDP crystals. Since the investigated R-KDP sample crystal was from prismatic sector, we tested this idea by measuring the UV-induced defect kinetic in an untreated or “raw” spot of crystal and compared it with the one measured in the extensively UV irradiated site.

Measurements were performed using the setup presented in section 2.3.3; the only modification, that we have made to this setup, is the use of the fourth harmonic of Nd:YAG laser (266 nm) for the defect excitation and pre-exposition (or conditioning) in R-KDP crystal. This choice of the 4^{th} harmonic was dictated by the fact, that under the 355 nm excitation, the induced kinetics with ‘reasonable’ signal to noise ratio (as those in Figure 2.8) could be acquired only at pump fluencies approximately twice as high a the multi-pulse damage threshold of crystal in study [81]. Thus, exposing it to thousands of pulses in the conditioning mode would have definitely damaged the sample. On the

other hand, the absolute TPA coefficient values for the 4th harmonic are more than an order of magnitude higher than that for the 3rd one [74], consequently much larger yield of absorbing defects is achieved and it becomes possible to better resolve kinetic traces at lower intensities. During these measurements, we have used the same laser pulses for defect formation and sample pre-exposition. Typical pump fluencies were ~ 4 J/cm^2 and this yielded defect absorption in the order of 150 mOD.

The results of above described investigation are presented in Figure 2.12. Here we see that after pre-exposition to 10^4 UV pulses the induced defect kinetic starts to significantly deviate, in the longer time scales, from the one measured in an unconditioned sample (note the log scale after the brake in this figure). This deviation, or specifically increase in lifetime, commences at ca. 200 ms delay and continues up the full disappearance of absorption. One could also speculate about the inverse effect (decrease of lifetime) at the 'short' timescales of up to ca. 100 ms; but this possible result is observed in the measurement noise and further investigations are necessary to convincingly conclude that.

Before discussing the data presented in Figure 2.12, it is worthwhile to note the study performed by Chirila *et al.* [41] that identified the absorption spectra of $\left[\mathrm{HP\dot{O}_4}\right]^-$ (A radical) and $\left[\mathrm{H_2P\dot{O}_4}\right]^0$ (B radical) centers while performing EPR measurements on irradiated and thermally annealed samples. These investigators proposed that: initially after the UV excitation mainly the B radicals are formed, while afterwards the holes are re-trapped into the A radicals. This proposition was backed by the notion that transient absorption spectra taken by Davis *et al.* [40] 1 ms after the excitation and likewise by Marshal *et al.* [42] after 1 s, closely resemble the ones of $\left[\mathrm{H_2P\dot{O}_4}\right]^0$ and $\left[\mathrm{HP\dot{O}_4}\right]^-$

centers, respectively. We think that our experiments results in UV-conditioned R-KDP sample could add temporal dimension to this model.

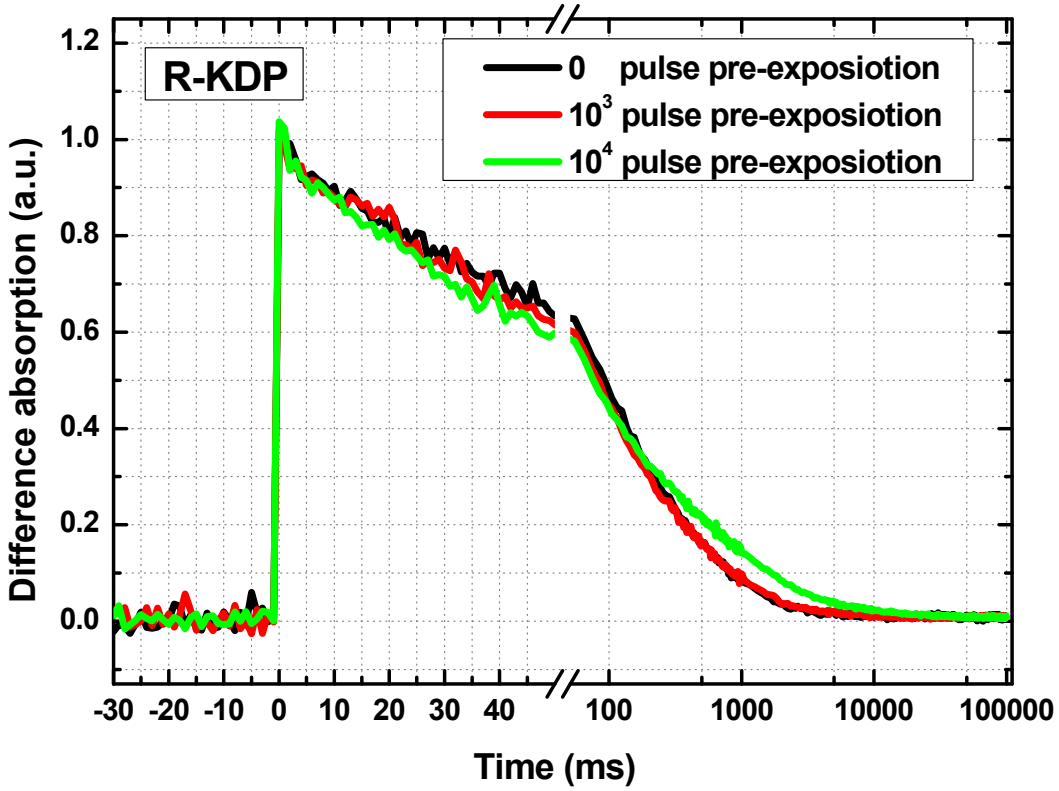

Figure 2.12 Influence of laser conditioning effect on defect state dynamics in R-KDP crystal. Measurements were performed at sample sites that were pre-exposed with different number of UV-laser pulses (266 nm). Note the log scale after the break.

As it can be seen in Figure 2.12, the initial defect dynamics (first ca. 100 ms) experiences small or no changes after the laser conditioning, while subsequent dynamics is strongly affected by it. This could be explained by the different nature of dominating defects. Namely, the decay of B radical that dominates at the 'short' times scale has little to do with structural defects (it is a self-trapped hole in a perfect lattice) and thus it is weakly affected by disappearance of neighboring fluorescent clusters; while the A radical, that presumably dominates in the 'long' time scales, is a center that lacks a proton, and in order to fully decay it has to meet a proton or a displaced hydrogen

atom. Thus, it would be conceivable that neighboring structural defects, formed during the growth of crystal, would increase the decay rate of such centers by ‘donating’ their weakly bound protons and later recapture, not necessarily at the same spot, the initially created one. This would also explain the conditioning process itself, as the UV-generated charges spread through the crystal and ‘heal’ the structural defects formed during the process of fast crystal growth.

We also make one practical notion from these investigations: as under UV-laser conditioning the density of defect clusters in the prismatic region approaches that of pyramidal (see Ref. [36] and Figure 2.3), and the overall UV-induced defect lifetime increases, this lifetime measurement could be used as one of parameters that characterizes KDP crystal homogeneity. And indeed, according to the results presented in Figure 2.8 where the KDP crystal has much longer overall defect decay time than the R-KDP one; and slowly grown crystals are expected to have considerably lower number of growth defects. These interpretations are further supported by the fact that they are in line with recently reported results [39] of damage threshold measurements performed with tightly focused 355-nm laser beam across the growth boundary of R-KDP crystal. In this study, it was observed that damage threshold in the pyramidal part of crystal is smaller then in the prismatic one. Higher growth defect concentration in prismatic sector causes longer-lived transient defects, and as the laser repetition rate in this study was 20 Hz, this causes a faster transient absorption accumulation and hence lowers the damage threshold.

3. A versatile three-pulse transient absorption spectrometer for UV-VIS-nIR spectral range

3.1. Introduction

Much of the current progress in the understanding of physics underlying the primary light-induced events in different materials, starting from small molecule chemistry and ending with the dynamics of complex biological systems, is based on femtosecond transient absorption spectroscopy. Its roots lie in the flash photolysis technique introduced by sir George Porter in the mid-twentieth century [82], who received the Nobel prize in chemistry in 1967. With the advent of pulsed lasers, delivering ever-shorter light flashes, the quest for time resolution began and progressed during the second half of the century. Powered by the advent of femtosecond Ti:Sapphire lasers, pump-probe and related techniques have become widely applied in biophysics [13, 83, 84], nanoparticle research [85, 86], solar cell research [87], and various aspects of physical chemistry. The processes of photochromism and photoisomerization [84, 88-91], energy transfer [92], electron transfer [93], proton transfer [94], solvation dynamics and intramolecular vibrational relaxation [95, 96], vibrational cooling [97] photochemical reaction dynamics [98], exciton dynamics in molecular aggregates [99] etc. were extensively investigated using pump-probe techniques. Significant progress was achieved not only in the experimental realizations of the technique, but also in the theoretical description, which was developed to include different resonant and non-resonant effects arising from the interaction between the investigated material and intense femtosecond laser pulses [100].

After opening the gates into the ultrafast world, femtosecond transient absorption techniques gained sophistication to tackle “inconvenient” biological systems: the pump and probe wavelengths

were extended both to the UV and infrared, giving access to higher-lying electronic states and vibrational transitions respectively; the former are important because of potential applications exploring biological material via its natural probes such as tryptophan [101], and the latter yields structural information about the molecular dynamics by probing vibrational modes directly [102]. Besides passive “excite and watch” method, control techniques were devised, where the excitation light pulses were specially tailored to produce desired photoreaction output [103]. This branch of spectroscopy-based techniques has been termed “quantum control” and “coherent control” and was, among other things, recently applied to photosynthetic light harvesting in both natural and artificial systems [104, 105]. Alternatively, multi-pulse transient absorption schemes were devised, where several intense laser pulses were tuned and timed to selectively interact with the stimulated emission or induced absorption bands of the photoreaction intermediates and thereby alter the reaction course [14, 15, 106]. Recent development of the technique to add dispersed spectral detection in combination with global analysis proved that such ‘incoherent control’ spectroscopy can be instrumental in unravelling different aspects of photoinduced molecular dynamics [107]. It has been applied to follow the *trans-cis* isomerization process in the molecules in solution [108, 109], disentangle complex energy relaxation pathways in carotenoids [20, 110], follow the dynamics of photoactive proteins [19], proton transfer reactions [111], and explain the multiple energy transfer pathways in photosynthetic light-harvesting complexes [112, 113].

Despite the fact that ultrafast transient absorption experiments have become a commonplace activity in modern physics, chemistry and biology labs, the instrumentation for it remains something that every group seeks to engineer from scratch. Although commercial systems have been introduced by Clarx MXR [114] and Newport Corp. [115], an

overwhelming majority of pump-probe spectrometers in use today remain home-built instruments, assembled by the scientists themselves and tailored to match their specific experiments. The reason for such absence of ‘industry standard’ is the fact that the requirements for ultrafast spectroscopic setups are constantly changing in terms of samples (gaseous, liquid, solid, cryogenic temperatures, thermostated etc.), collected data (kinetic traces, time-gated spectra, both) and automation levels. Independent design allows the scientists to retain the required flexibility; however, it comes with the penalty that every group follows similar paths of trial and error while putting their ultrafast systems together.

In this chapter, we try to present a partial solution to this issue by providing an exhaustive technical description and characterization of multi-pulse transient absorption setup developed and used in our laboratory. This description is by no means meant to set the standard for the field, or to claim that our implementation of multi-pulse pump-probe system is in any way better than those used in other labs. Our goal is to provide detailed information about one of the possible realizations of such setup for the people who are developing their own transient absorption systems and thereby to facilitate their efforts by providing the technical details underlying the system, rather than limiting ourselves to the brief descriptions normally found in ‘Materials and Methods’ sections of application-oriented papers. The technical description is organized into three major parts, describing a) the laser sources used, b) beam delivery components and optical layout and c) detection scheme, including optics, electronics and software used to collect and process the transient absorption data. In the last sections, the characterization of the various aspects of the spectrometer is performed, and the application of the setup to measure three-pulse transient absorption data on the molecular solution is presented.

3.2. Multi pulse transient absorption spectrometer (MPTAS): general description

3.2.1. General system layout

The overall layout of the system is presented in Figure 3.1. The backbone of the system is a commercially available amplified Ti:Sapphire laser system (Millenia/Tsunami/Evolution-X/Spitfire, Spectra Physics, USA), that employs chirped pulse amplification technique [116] to produce laser pulses with the following parameters: duration – 120 fs (FWHM), center wavelength – 803 nm, repetition rate – 1 kHz, pulse energy – 0.9 mJ).

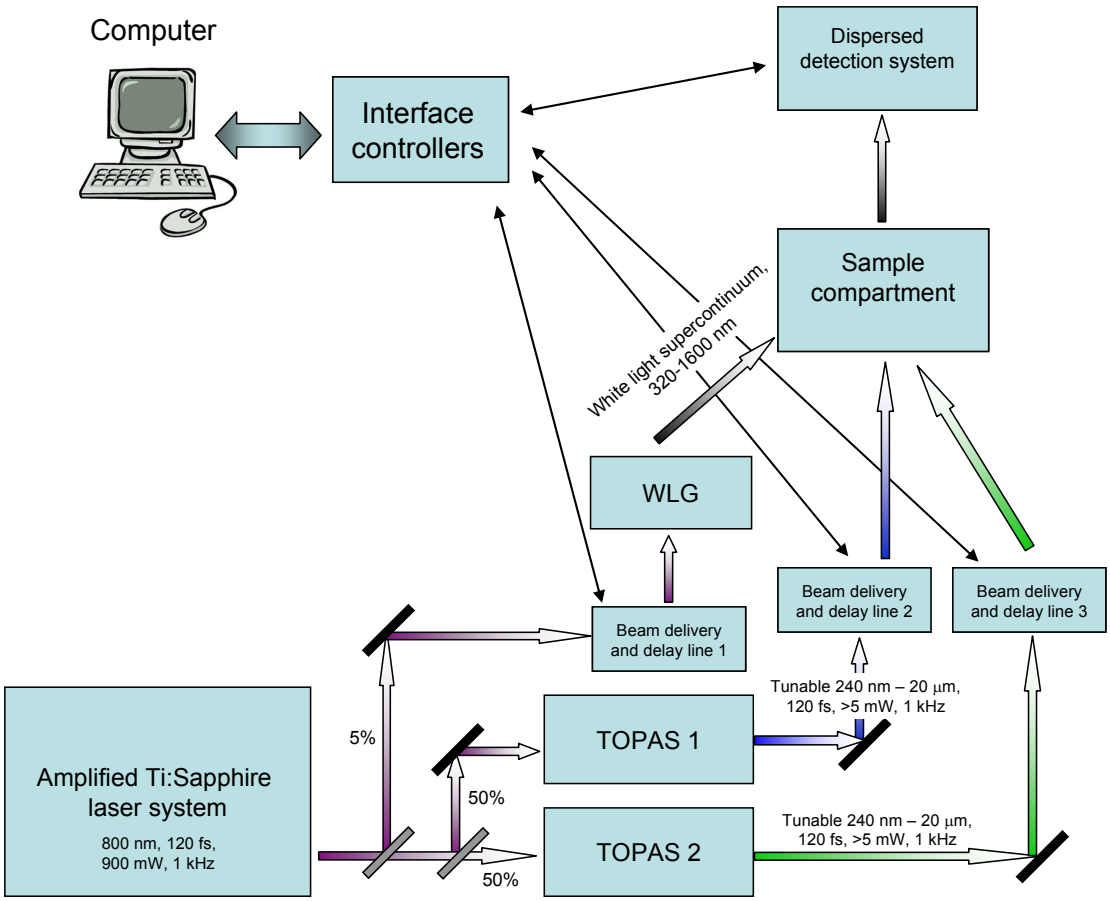

Figure 3.1 General layout of three pulse difference absorption spectrometer.

The fundamental output of the laser is split into three branches at power ratios 47.5 % : 47.5 % : 5 % using dedicated 5 % and 50 % dielectric beamsplitters on 3 mm thick fused silica substrate (Eksma, Lithuania). Fused silica substrate is essential for these beamsplitters because the peak power of the laser pulses is enough to produce multi-photon excitation of optical glasses (for example, the widely used BK7) which induces the formation of color centers and, consequently, absorption loss in the beamsplitter substrate. The two high-intensity beams are used to pump traveling wave optical parametric amplifiers (TOPAS, Light Conversion, Lithuania), providing excitation pulses tunable from 240 nm to 20 μm. The remaining 5 % of the fundamental output was delivered close to the sample compartment via the beam delivery and delay line 1 (BDDL1, see below). Before the sample, this light was used to produce white light supercontinuum for probing. The output beams of the two TOPAS amplifiers were delivered to the sample compartment via beam delivery and delay lines 2 and 3 (BDDL2 and BDDL3, see below) intersected with the probe beam in the sample. After passing through the sample, the probe light was dispersed in a spectrograph and detected using a home-built spectral detection system (see below). The beam delivery and detection was controlled by the computerized automation and data acquisition system. In the following sections, we discuss the details of all the system components.

3.2.2. Light sources

Amplified Ti:Sapphire laser system. Since the laser system underlying the multi-pulse transient absorption spectrometer (MPTAS) is commercial, in this section we will only address its main characteristics, such as pulse duration and spectrum, energy stability, transverse beam profile etc., which depend on the laboratory environment and system alignment.

We start the characterization of the system with the second-harmonic FROG trace of the Sptifire laser pulses is shown in Figure 3.2 along with the retrieved time- and wavelength-dependence of the electric field within the pulse. As indicated in Figure 3.2 C, the full width at half maximum of the integrated autocorrelation trace is ca. 170 fs, which corresponds to the pulse duration of ca. 120 fs. The temporal phase distribution (Figure 3.2 C) is relatively flat at the regions of the pulse, where the intensities are appreciable (above 10% of the maximum.). The correspondence between retrieved and measured autocorrelation traces is near-ideal. The retrieved spectrum of the pulse is similar to the measured spectrum (Figure 3.2 D), however, the correspondence is poorer than that of the autocorrelation trace, most probably because of acceptance angle limitation, induced by the mixing crystal (0.6 mm BBO, see Figure 3.2 D). In the spectral phase, the cubic phase distortion is evident (Figure 3.2 D, gray curve), which the grating compressor used in the Spitfire laser cannot compensate [117]. Overall spectrotemporal pulse quality can be estimated from the Laplacian time-bandwidth product (that $\Delta\tau_{RMS}$ and $\Delta\upsilon_{RMS}$) [118] which in this case is 0.6 (whereas in a pulse with a completely flat spectrotemporal phase it would be 0.5 [119]).

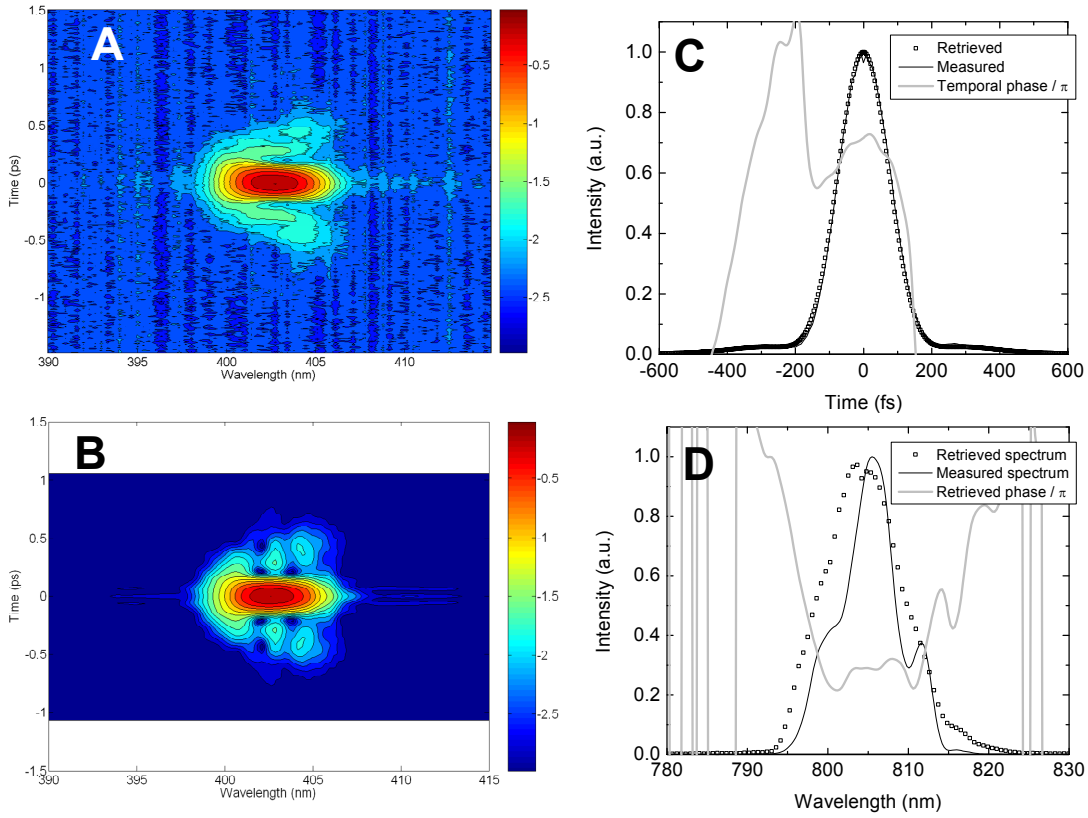

Figure 3.2 Experimentally obtained (A) and software retrieved (B) frequency-resolved optical gating (FROG) data of the SuperSpitfire laser pulse. Note that the base 10 logarithm of the FROG signal is depicted on the z scale. C: Temporal characteristics of the pulse (measured and retrieved autocorrelation traces and time-dependence of the electric field phase); D: Spectral characteristics of the pulse (measured and retrieved power spectra and wavelength-dependence of the electric field phase).

Besides the spectrotemporal characteristics of the pulse, spatial characteristics (transverse mode) is of paramount importance. The transverse mode determines propagation characteristics of the laser pulses and the size of the spot, into which the light of the laser source can be focussed. Transverse beam profile of the Spitfire laser is shown in Figure 3.3 A. It is obvious that the beam profile deviates significantly from the desired Gaussian profile, characteristic to a TEM_{00} mode. Although in the focal plane of the singlet fused silica lens (f = 250 mm) it yields a relatively symmetric spot (Figure 3.3 B).

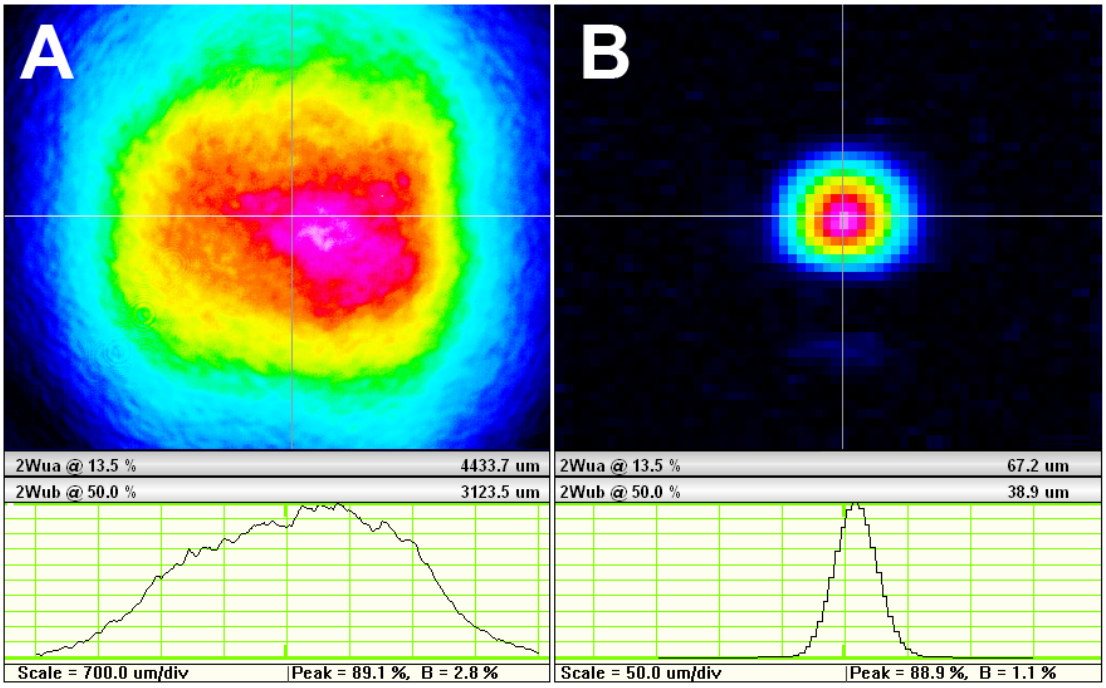

Figure 3.3 Spatial profiles of unfocussed (A) and focused (B) beams of the Spitfire laser. Focusing was performed using a singlet fused silica lens with the focal length of 250 mm.

Finally, the third parameter governing the performance of the entire spectrometric system is the energy stability. Since the pump and probe light is created from the fundamental output of the laser using nonlinear optical frequency converters (Topas, white light generator), the energy fluctuations of the driving laser ultimately become amplified and affect the quality of acquired data. Laser stability measured over 1 hour period (which is a typical timeframe of a time-resolved difference absorption measurement) recording the energy of every laser pulse is shown in Figure 3.4. As is evident from the raw data, the drift of the mean power is negligible and the long-term fluctuations are of the order of 5%. It must be noted that the trace graph is not entirely representative, because it contains too many data points and the edges of the trace are defined by the outlier pulses with “untypical” energies. The histogram shown in the inset of Figure 3.4 (note that the vertical scale is logarithmic) indicates that the standard deviation of the dataset is at

ca. 1.1 % of the mean, which is the real measure of the stability of the laser energy.

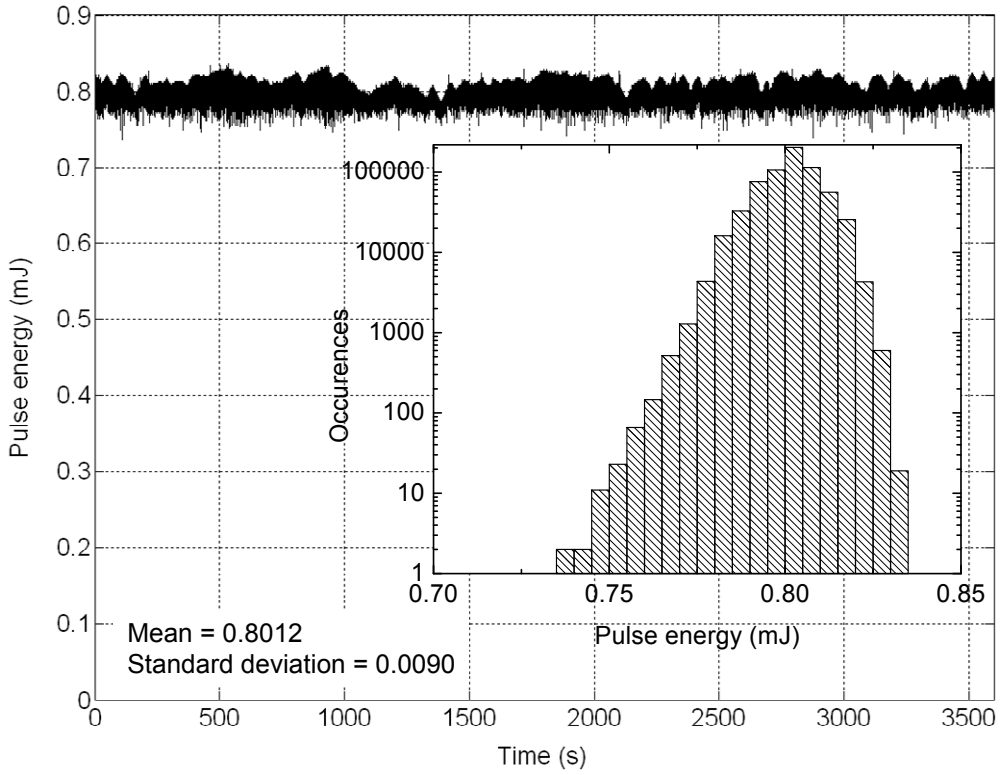

Figure 3.4 Energy stability of the Spitfire laser measured over 1 hour period. Histogram plot and statistical parameters of the obtained distribution are shown in the insets.

From the histogram, asymmetry of the distribution is evident: the pulses with energies lower than the mean are more likely to occur than the ones significantly exceeding the average energy. In simple words, one laser pulse out of a thousand is a low energy outlier. This fact must be accounted for, when averaging the acquired experimental data: outlier points can significantly contaminate the measured signals and deteriorate the quality of averaged data. Finally it must be noted that the indicated stability is achievable if the following environmental conditions are fulfilled in the lab: a) temperature is stable within the margin of 2°C (the air conditioning system in our lab keeps it between 19.5 and 21.5°C); b) the air turbulence on the laser table is minimized

(the seed beam from the Tsunami laser is guided to the Spitfire inside the metal pipes and the entire laser table is enclosed in solid casing with access windows for alignment); c) sufficient vibration isolation is provided by the optical tables (1HT/1VIS Standa, Lithuania). Additionally, clean environment bust be retained by slight overpressure created inside the table casing, the air supply of which is cleaned using HEPA filters.

Travelling wave optical parametric amplifiers (TOPAS) used for producing tunable frequency pump pulses (TOPAS 1 and TOPAS 2) have been described previously [120]. These fully automated devices are commercially available from Light Conversion, Lithuania, and have recently been remarketed by all the major ultrafast laser producers. The principle of operation is as follows: the part of the pump beam focused in type-2 β–barium borate (BBO) crystal produces parametric superfluorescence, which is then amplified in the same crystal, passing it several times and parametrically mixing the superfluorescence with the pump light. The signal wave of the TOPAS amplifier pumped by 800 nm Spitfire pulses can be tuned in the range from 1150 to 1600 nm, whereas the idler wave covers the spectral region from 1600 to 2630 nm. Using subsequent nonlinear frequency converters (frequency doubling and quadrupling of the signal and idler respectively, sum frequency between the signal/idler and residual pump, difference frequency between the signal and idler and combinations thereof), the total pump spectral range varies from 240 nm (second harmonic of sum frequency between the signal and residual pump) to ca. 20 μm (difference frequency between signal and idler). In our spectrometer, each TOPAS is pumped by 47.5 % of the fundamental laser output (ca. 380 μJ energy), and the conversion efficiency into the parametric radiation (signal + idler) is of the order of 30 %, depending on the wavelength.

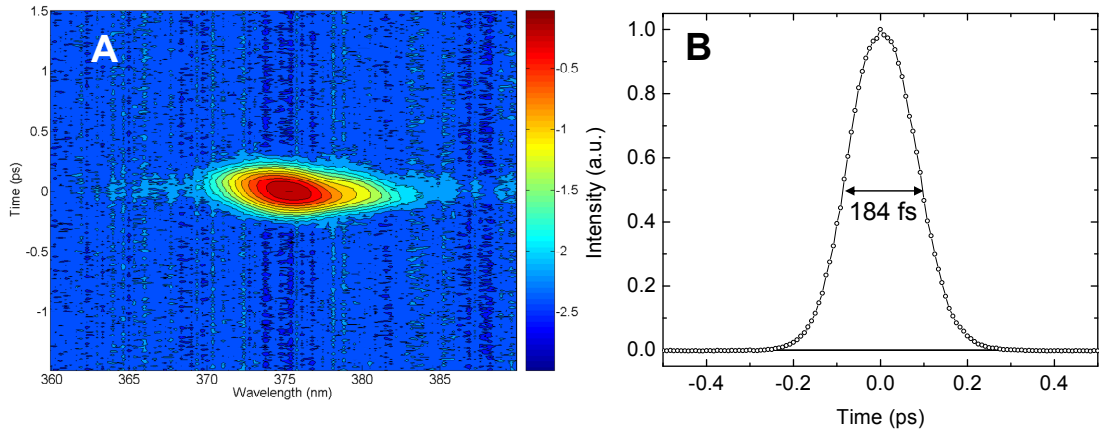

Figure 3.5 A. Second harmonic FROG trace of the TOPAS signal output. Z scale depicts the logarithm of the measured data to enable the viewing of smaller details. B: The corresponding pulse autocorrelation function reconstructed from the data.

Pulse characteristics of the second harmonic of TOPAS signal are summarized in Figure 3.5. From the FROG trace shown in Figure 3.5 A, it can be inferred that the nonlinear parametric conversion and subsequent frequency doubling processes result in a significantly "cleaner" pulse than that produced by the Spitfire laser: the FROG trace more closely resembles an ellipse than the trace shown in Figure 3.2 A. The corresponding autocorrelation trace (which can be reconstructed from the FROG data by integrating it over the entire spectrum) lacks the wings due to uncompensated cubic phase distortion seen in Figure 3.2 C. The FWHM of the autocorrelation function of the pulse is 184 fs, which corresponds to 130 fs pulse length, assuming Gaussian pulses. The reason for such "cleaning up" of the pulse is the fact that relatively weak regions of the pulse become diminished during the nonlinear parametric conversion process, which takes place only when the intensities of the pump are above the threshold for parametric superfluorescence. The slight "tilt" of the FROG trace shown in Figure 3.5 A is due to the chirp induced by the optics of the TOPAS. To summarize, the pulse does not become wider in the process of

parametric conversion, and the spectrotemporal characteristics are even improved.

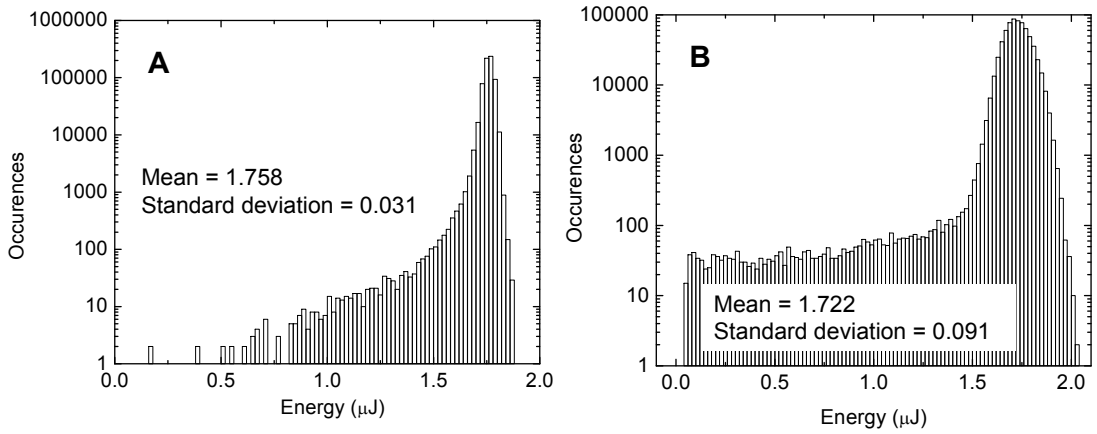

Figure 3.6 Energy stability of the fourth harmonic of TOPAS signal (A) and idler (B) output, accumulated over 1 hour period. Statistical parameters of the obtained distribution are shown on the plots. Note the logarithmic y axis. The average power was attenuated to ca. 1.75 μJ in both cases.

Figure 3.6 shows energy stability of the fourth harmonic of TOPAS signal (A) and idler (B) output measured over 1 hour period. The obtained distribution shows significant asymmetry with significantly larger number of low power shots than observed in Spitfire output. Also, the relative stability (estimated as the standard deviation of the measured distributions) are at 1.7 % for the fourth harmonic of the signal and 5.3 % for the fourth harmonic of the idler. The reason for this deterioration of stability is the nature of parametric superfluorescence, which is used as a seed light for the parametric amplifier: being a nonlinear process, initiated by the quantum noise in the crystal, it is extremely sensitive to the stability of the pump source. It must be noted, however, that the fourth harmonic of the signal and idler output is the 'worst case' scenario for the TOPAS, i.e. the configuration where the number of nonlinear conversion stages is the highest. The fact that the stability of several percent was achieved even in this case, can be evaluated as quite adequate for transient absorption experiments. The fact that idler output is less stable than the signal is likely due to the fact

that the same set of crystals is used to quadruple the frequency, and the saturation of these nonlinear processes is poorer in the case of the idler.

White light continuum generator. For probing the entire difference absorption spectrum at once, a broadband femtosecond light source is necessary. For this purpose, white light supercontinuum is normally used, which is produced by focusing the fundamental femtosecond laser output into nonlinear medium [121]. Due to the processes of self-phase modulation and light filamentation which are caused by the nonlinear refractive index of medium, a relatively narrow spectrum of near-transform-limited femtosecond pulses is converted into broadband radiation, covering the spectral range of hundreds of nanometers. The eventual spectral range covered by the supercontinuum depends on the band gap of material used – the band gap limits the extent of the spectrum to the higher frequencies [122]. Traditional materials are ethylene glycol, water and sapphire, which, when pumped with 800 nm femtosecond pulses, allow efficient generation of white light up to approximately 450 nm. To extend the spectrum of the probe as far to the UV as possible, we opted for CaF_2. The problem with using this material is its relatively low damage threshold, which results in the damage of the crystal and severe instability of the supercontinuum probe, if no additional measures are taken. However, it turned out that if the crystal is translated slowly (2 mm/s) during the experiment, no damage occurs and stable white light can be produced. Apparently, the damage mechanism is stepwise, when transient defects (such as colour centres) are produced in the crystal [123], which later absorb the incident radiation and result in the damage due to thermal stress. The best results were obtained by attaching the crystal to the xy stack of translation stages connected to the rigid rotating arm of the motor via a bearing. This produces circular motion of the crystal without turning points, while keeping its optical axis stationary. It must be noted that

rotational motion of the crystal (which is easier to realize technically) should be avoided, because CaF_2 is a relatively soft material and has some residual birefringence (even though its symmetry forbids it) due to growth defects and mounting stress. If such crystal is rotated, the polarization properties of the generated probe light will vary during the experiment, resulting in unreliable data.

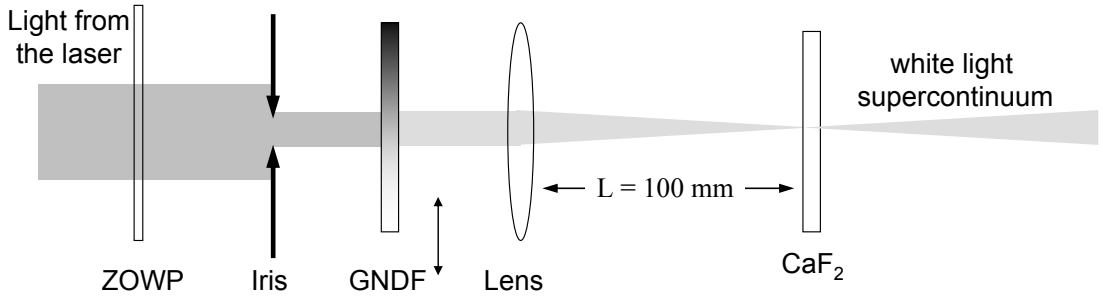

Figure 3.7 Optical layout of the white light continuum generator. ZOWP is zero-order half wave plate; GNDF is gradient neutral density filter.

Practically the white-light continuum generator is realized using the optical layout depicted in Figure 3.7. Zero order half wave plate (Eksma, Lithuania) placed in the incoming laser beam allows controlling the polarization of the produced white light continuum. The iris serves three functions: selecting the most stable spatial portion of incoming beam, course control of the incident intensity and control of the focusing properties of the lens. The fine control of the incident power is controlled using a gradient neutral density filter (Thorlabs, UK). The adjustment of the iris and the neutral density filter is made based on observed white light continuum spectrum: the optimization target is as much light as possible with minimum pulse-to-pulse noise. The incident light intensity must be kept below multi-filament level, i.e. the white light continuum should consist of a single filament. If multiple filaments occur in the crystal, the spectrum of the continuum becomes modulated due to their interference, and the stability deteriorates severely. The focussing lens is a simple singlet fused silica lens with the focal length

of 100 mm. This focal length was found to produce the most stable supercontinuum for probing.

It must be noted that the intensity of white light continuum strongly depends on the length of the medium (CaF_2). The longer medium produces stronger and better saturated (i.e. more stable) white light. However, the allowable path length of the CaF_2 crystal is limited by the group velocity dispersion of the produced continuum. To keep it at acceptable levels, 3 mm length crystal was found to be most appropriate. The characteristics of the resulting white light are discussed below (see section 3.3.2).

Finally, it is important to stress that the white light generator should be placed as close to the sample as possible, because the angular dispersion is present in the generated white light continuum (i.e. the divergence is different for different colors [122]) and significant portion of light is inevitably lost if an attempt is made to collimate it and transport over longer distances. Furthermore, if the delay line is present in the probe path, it is better to delay the fundamental of the laser, which has much smaller divergence and better propagation qualities. That way, the properties of white light will be constant at different delay values – a desirable property for measuring light.

3.2.3. Optical layout

Beam delivery and delay. Optical layout of the MPTAS spectrometer is shown in Figure 3.8. The beam delivery lines provide: a) adequate timing for pump and probe pulses; b) polarization control of the three beams with respect to each other; c) pulse energy control in the three beams; d) means of closing and opening the beams to enable difference absorption measurements.

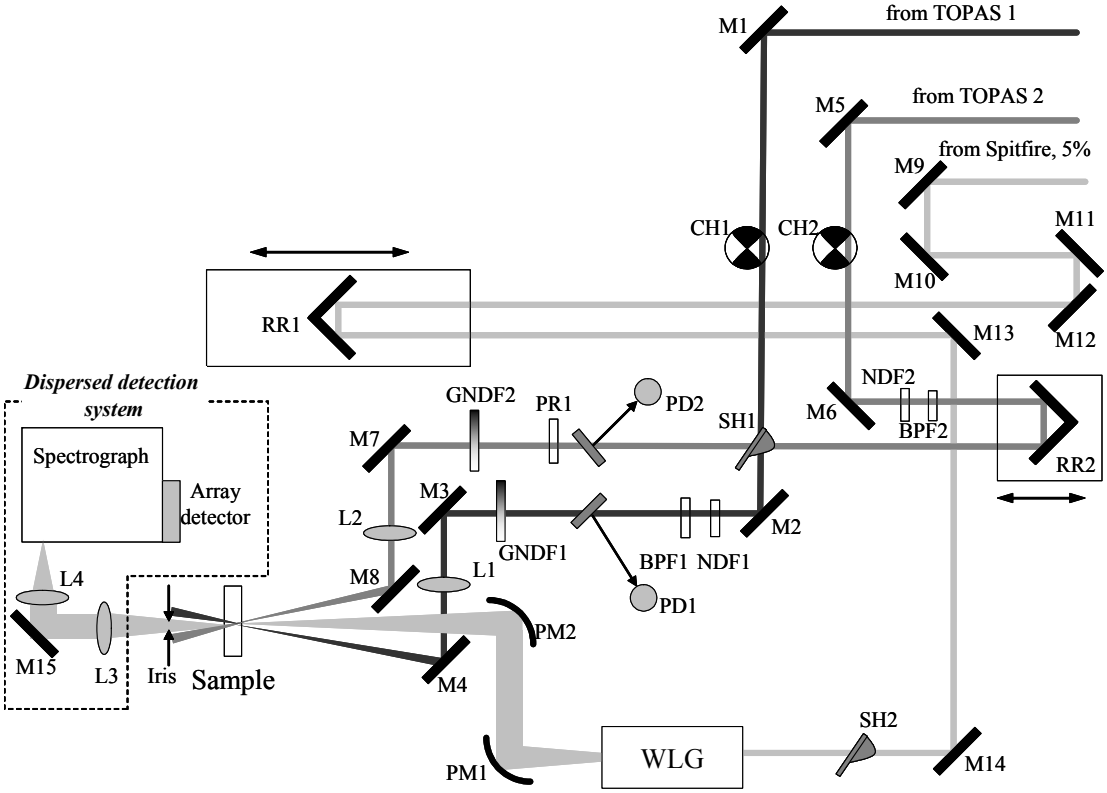

Figure 3.8 Optical layout of the multi-pulse transient absorption spectrometer: beam delivery and delay lines BDDL1 (light grey ray traces), BDDL2 (dark grey ray traces) and BDDL3 (medium grey). Dashed line encloses dispersed detection optical system. See text for further details and part notations.

Beam delivery and delay line used for handling the probe beam (BDDL1) is depicted by light grey ray traces. Mirrors M9 through M14 are dielectric high reflectors for 780-830 nm and 45° incidence angle (Altechna, Lithuania). M9-M11 fold the 800 nm beam to compensate the optical path length in the TOPAS1 and TOPAS2 amplifiers. Further, the beam enters the optical delay line which consists of a hollow corner cube retroreflector RR1 (protected gold coating, Edmund Optics, USA) mounted on a linear translation stage with linear position encoder (Aerotech ALS10060). In shorter delay lines, RR1 can be replaced by a mirror pair, however when the travel range exceeds 100 mm, pitch and yaw error of the translation stage become an issue and the angle of the returning beam starts to vary appreciably, as the stage moves. The direction of the beam returned by the retroreflector is insensitive to the angular deviations and thus the transverse position of the focal spot in

the sample remains stationary. Beam exiting from the RR1 is picked up by the mirror M13 and directed to the white light generator (Figure 3.7, see text above).

Electromechanical beam shutter SH2 (home built following [124, 125]) allows computerized closing and opening of the probe beam. The diverging white light continuum is collimated and subsequently focused into the sample by right angle off-axis parabolic reflectors PM1 and PM2 (protected aluminum coating, effective focal lengths 50.8 mm and 203.2 mm respectively, Janos Technology). Aluminum coating was selected because of its broad reflectance range, especially in the UV region and the mirrors were used instead of lenses in order to minimize the group velocity dispersion (GVD) of the white light continuum. Minimum GVD is desirable for at least two reasons: first of all, it reduces the number of delay points necessary in order to resolve fast dynamics around time zero and, secondly, coherent artifacts of pump-probe measurements become more pronounced when chirp is introduced into the probe [126, 127]. More details on the actual parameters of the probe light are given in the section 3.3.2.

The lines of the pump beams BDDL2 and BDDL3 (see Figure 3.1) are depicted by dark grey and medium gray ray traces in Figure 3.8. Mirror pairs M1/M2 and M5/M6 are dielectric mirrors designed to reflect specific tuning ranges of TOPAS amplifiers and suppress the residual unused signal/idler/pump outputs. They are essential in order to remove spectral components other than the ones used for pumping and reduce the power incident on the subsequent optical component (metallic coatings can easily be damaged even by unfocused TOPAS output). Shutter SH1 blocks both pump beams when data is not being collected (delay lines are moving or the experiment is finished) to prevent sample degradation due to overexposure, and optical choppers (Stanford Research Systems SRS540) block and open both pump beams at different frequencies (250 and 500 Hz) to enable differential

measurements. The power of the beams is further attenuated using neutral density filters NDF1 and NDF2 and the spectral purity of the pump beams is ensured by bandpass filters BPF1 and BPF2. Beam from TOPAS2 then enters another delay line composed of a linear translation stage (Aerotech ALS10030) and hollow retroreflector (protected aluminum coating, Edmund Optics). About 4% fractions of both beams are then split off by fused silica plate beamsplitters to the photodiodes for pulse power monitoring. The beams are then passed through variable neutral density filters GNDF1 and GNDF2 that enable precise excitation energy control and focused into the sample by singlet fused silica lenses L1 and L2 (300 mm and 250 mm focal length respectively). The angle between the two pump beams is less than 4.5° with probe beam in the middle (2.25° angle between the probe and each of the pump beams). Berek polarization compensator PR1 (New focus 5540) in BDDL2 enables polarization control of the beam over the wide spectral region (200 nm to 1600 nm). Used together with the half wave plate in the white light generator (Figure 3.7), it allows any polarization configuration between the pump beams and the probe.

Sample compartment. The sample compartment consists of the sample holder providing the controls for adjusting the focal position of the sample and iris for blocking the pump light after it passes the sample cell. Free-space design with ca. 250 mm of unobstructed space around the sample allows free variation of sample containers (static cell, flow cell with the peristaltic pump, cryostat, solid-state sample etc.). Liquid samples (solutions) are contained in 1 mm path length fused silica cells (Hellma, Starna). Longer cells deteriorate the temporal instrument response function (IRF) while not improving the signal significantly, because beam interaction length in the sample is close to 1 mm at current focusing conditions. Shorter cells can be used at the cost of increasing optical density of the samples, which is not always possible.

Dispersed detection system. After the sample, the white light is recollimated and refocused (lenses L3 and L4, mirror M15) into the slit of quarter-meter Czerny-Turner spectrograph with all-reflective optics and diffraction grating (150 lines/mm, blaze wavelength 500 nm, Newport). The spectral resolution ant the image plane of the spectrograph was ca. 1 nm. White light spectra were recorded on a pulse-to-pulse basis using a home-built linear array detector system (see below).

3.2.4. Data collection and processing: acquisition procedures, detectors and electronics

Chopper states and possible signals. In a three-beam spectrometer, two pump beams are modulated by choppers CH1 and CH2 (Figure 3.8) and the recorded white light spectra are classified according to the chopper states. Hereafter we will denote one of the pump beams 'pump' and the other 'dump' to make a distinction, however the choice of which one is which is arbitrary. The pump and dump states allow four combinations in total:

CH1 state	CH2 state	White light notation
Off	Off	WL_{00}
On	Off	WL_{10}
Off	On	WL_{01}
On	On	WL_{11}

Out of these four signals, three difference absorption signals can be constructed by calculating absorbance change with respect to that of the unpumped sample. We denote them 'Pump-probe' (PP), dump-probe (DP) and pump-dump probe (PDP) respectively:

$$PP(t_{pump},\lambda)=\lg\frac{WL_{10}}{WL_{00}}$$
$$DP(t_{dump},\lambda)=\lg\frac{WL_{01}}{WL_{00}} \quad (3.1)$$
$$PDP(t_{pump},t_{dump},\lambda)=\lg\frac{WL_{11}}{WL_{00}}$$

To be able to construct these spectra, white light spectra must be detected in sync with the state of the choppers.

Detectors. Chopper states are recorded by measuring the pump pulse energy after the choppers. For that, two silicon photodiodes PD1 and PD2 (Figure 3.8) are used (Hamamatsu 1337-1010BQ, reversed biased by 4.5 V). The pump light on the diodes is attenuated using neutral density filters not to exceed one third of the supply voltage. This ensures that the diodes are working in linear range and the information about the pump light stability is gathered during the experiment. The signals form the photodiodes are stored in sample-and-hold circuits (home built, based on National Semiconductor LF398 integrated circuit) supplied to two analogue inputs of data acquisition computer board (DAQ, National Instruments 6120). The readings are then classified by the data acquisition software, separating out three possible chopper states: a) pulse is present, high signal; b) pulse is absent, low signal; c) pulse is being clipped by the chopper, intermediate value. If the chopper rotation is phase-locked to the laser pulse train, the latter case does not take place.

White light spectra are recorded by silicon linear array sensor (Hamamatsu S3901-256Q, driver circuit Hamamatsu C7884) placed at the image plane of Czerny-Turner spectrograph (Figure 3.8). Given the ‘start’ and ‘clock’ signals derived from the laser trigger, the driver circuit reads out the light intensity values on each of 256 array pixels. The analogue signal values are supplied to another analogue input of the DAQ. The driver circuit also generates a trigger signal, indicating the

precise time instant when the analogue values must be digitized by the board. With each laser pulse, 256 pixels of the array detector are read out and digitized. Given the repetition rate of the laser (1 kHz) and the resolution of A/D converter (16 bits or 2 bytes), the resulting data flow from one detector is 256×1000×2 = 512000 Bps.

Reference beam. In many implementations, a reference beam is added to the pump-probe setup to improve signal-to-noise ratio. The probe light is split into two portions, one of which intersects with the pump beam at the sample ('sample' beam) and the other impinges on the spot where pump light is not present ('reference' beam). The sample white light is then divided by the reference thereby canceling out all the contributions due to the fluctuations of the probe intensity:

$$WL \Rightarrow \frac{WL_{sample}}{WL_{reference}}. \tag{3.2}$$

The difference absorption signals are then calculated by substituting Eq. (3.2) into Eq. (3.1). Referencing improves the signal-to-noise, when the source of noise is the instabilities of the probe light. However, it requires an additional multi-channel detector and the data flow increases by a factor of two. In our implementation of the dispersed multi-pulse transient absorption spectrometer, we opted for leaving the reference beam out because of two major reasons: firstly, it is virtually impossible to have a beamsplitter that would divide the white light continuum probe into two equal parts over the spectral range of 320 nm to 1100 nm (the spectral range of the spectrometer), and, secondly, the primary source of noise in the dispersed setup is the electronic noise of the detection system, because the amount of probe light falling on every pixel of the array detector is low, when the white light generator is operated in a stable, single filament mode. When using the reference beam, the amount of the white light on single detector is decreased twofold and the electronic noise is enhanced correspondingly.

Measurement sequence and data processing. Given the fact that the setup generates the data at the rate of 0.5 MBps, and a typical duration of a transient absorption experiment is 60 minutes, it is obvious that data reduction must be performed during the measurement to avoid storing excessive amounts of data. To this end, the measurement sequence is organized in the following way: the data is acquired in buffers, containing a large number of laser shots each (for example, 1 second of measuring time, corresponding to 1000 laser pulses). The acquired white light spectra are then sorted into bins according to the states of the pump and dump choppers. At this point, statistical analysis of the acquired experimental points is performed and the spectra, where the pump or dump intensity was exceedingly low, are discarded. Figure 3.6 indicates that such data processing is essential: the energy distribution of the TOPAS output is asymmetric, with significant fraction of pulses carrying much lower energy than the average. Such laser shots are bound to produce ‘outlier’ spectra and should be excluded from the averaging. Normally, the laser pulses, where the energy differs from the median by more than three standard deviations are discarded.

The same selection procedure is performed on the acquired white light spectra themselves, discarding the spectra, the root-mean-square (RMS) error of which is higher than a user-set limit. Typically, the overall amount of discarded data is below 10 percent and the acquired data are not distorted by the selection procedure. Before acquiring the white light spectra, a background signal is measured by closing the probe shutter (SH2 in Figure 3.8). This accounts mainly for the ambient light and the pump and dump light scattered into the spectrograph. The background value is then subtracted from the acquired white light spectra, and Eq. (3.1) becomes:

$$PP(t_{pump},\lambda)=\lg\frac{WL_{10}-WL_{10}^{background}}{WL_{00}-WL_{00}^{background}}$$
$$DP(t_{dump},\lambda)=\lg\frac{WL_{01}-WL_{01}^{background}}{WL_{00}-WL_{00}^{background}} \quad , \quad (3.3)$$
$$PDP(t_{pump},t_{dump},\lambda)=\lg\frac{WL_{11}-WL_{11}^{background}}{WL_{00}-WL_{00}^{background}}$$

where the WL values are the averages of different 'bins' of spectra after the sorting by the pump and dump states and selection procedures. For each delay point, the measurement sequence can be repeated several times and more than one buffer of 1000 pulses can be acquired. Since the data resulting from one buffer is just one spectrum, different buffers can be stored separately on the computer. It is preferable to store raw white light spectra (averaged over the buffer) rather than calculated difference signals, because the raw data might contain information about the problems that occurred during the measurement. Background measurements can be performed only once for several tens of even hundreds of buffers, because they represent the ambient conditions, which, in the ideal case, do not change. The measurement sequence can be formalized as follows:

1. Measure background, if necessary (for example, a certain number of data points was measured since the last background measurement).
2. Move the pump and dump delays to a desired position.
3. Acquire a buffer (~1000) of white light spectra.
4. Sort the spectra by chopper states into 'bins' (WL_{00}, WL_{01}, WL_{10} and WL_{11}).
5. Discard the spectra with unsuitable excitation energy values.
6. Average the spectra in each bin, calculate RMS errors.
7. Discard the spectra with RMS errors larger than the user-set value.

8. Calculate difference absorption spectra using Eq. (3.3), plot and store the data.
9. If the desired number of buffers per delay point has not been reached, return to the step No. 3.
10. Proceed to the next time point.

It is desirable to organize the experiment in several ‘scans’, i.e. measure a sequence of delay points several times and store the results separately. Such organization provides the way of monitoring the state of the sample over the experiment: if the signal changes in a consistent fashion across the different scans, it is an indication that the sample is degrading due to overexposure to pump and dump light.

3.3. System characterization

3.3.1. Mode matching

To ensure reliable experimental results, the diameter of the probe beam at the sample needs to be kept well below that of the pump beam. This way, the entire probed area of the sample is excited in almost a uniform fashion, and the results of the experiment become less sensitive to the fact that the white light beam possesses some spatial transverse distribution of light wavelengths, and the pointing instability of the laser. Figure 3.9 shows the spatial profiles of the pump and the probe beams at the sample spot. The diameter of the dump beam is equal to that of the pump, because the two beams originate from the identical instruments (TOPAS). As is evident from the graphs, under the given focusing conditions, the pump beam diameter is ca. 150 μm, which is three times as large as the probe. This value along with the excitation energy is used in the estimations of how many photons enter the irradiated sample volume with each laser pulse.

Albeit precise, such measurement is normally not used to adjust the spatial overlap of the pump and the probe pulses in the sample. It is much less time consuming to optimize the overlap using a test sample (e.g. laser dye, such as DCM) and optimizing its pump-probe signal.

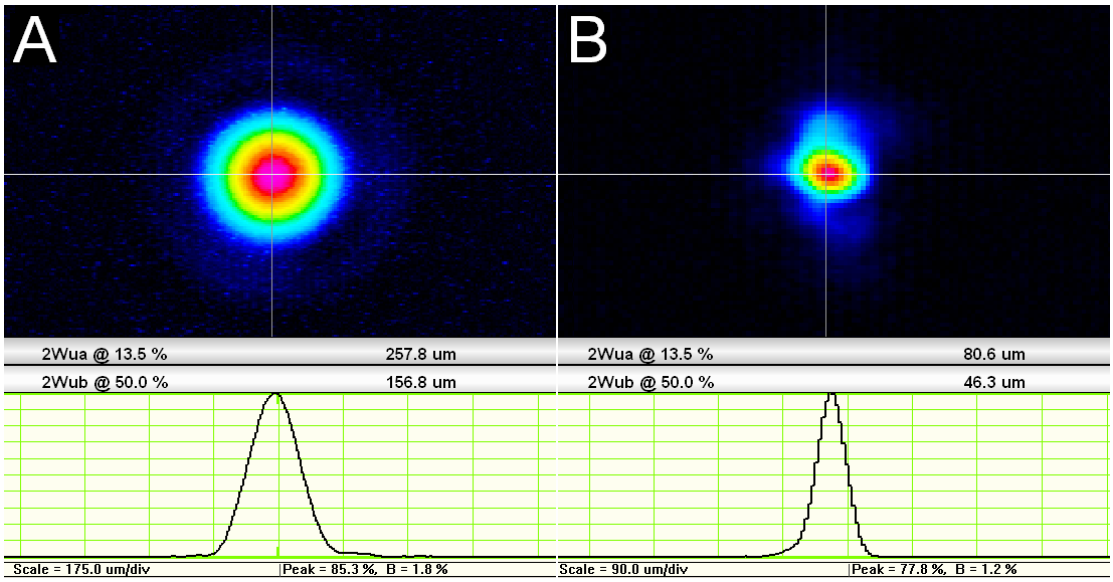

Figure 3.9 The spatial profiles of the pump beam (A) and probe beam (B) at the place of the sample. The estimated beam diameters at 50 % (FWHM) and 13.5 % ($1/e^2$) are shown on the graph.

3.3.2. Instrument response function and group velocity dispersion

A key parameter determining the performance of MPTAS spectrometer is its time resolution. It is normally evaluated by investigating the instrument response function (IRF) of the setup. IRF of a pump-probe setup corresponds to the cross-correlation between the pump and the probe pulses. In the dispersed detection scheme, where all the probe wavelengths are detected simultaneously, it is important to keep in mind that the probe light has a characteristic dispersion associated with it, i.e. the red components of the probe reach the sample before the blue ones and the signal is first observed in the blue part of the spectrum. Effectively, this translates in the observation that the time zero is different for every wavelength. Thus, the IRF has to be

measured at all wavelengths and the corresponding time shifts have to be determined.

Measuring this cross-correlation is not trivial. At least three different methods can be used, each with its own merits and disadvantages: 1) optical Kerr effect measurement in cubic nonlinear medium; 2) upconversion of probe light using a nonlinear crystal; 3) estimating IRF from the pump-probe measurement directly. The most precise and correct way of measuring IRF is the optical Kerr experiment (see Figure 3.10), where the sample cell is filled with cubic nonlinear medium, the probe light is cross-polarized after the sample, and the pump polarization is set at 45° with respect to the probe. When pump and probe pulses overlap in time and space, the probe polarization is rotated in the sample and the signal proportional to the intensities of both beams is registered by the detector. This way, IRF is measured in precisely the same arrangement as that of pump-probe experiment (the sample is replaced by transparent nonlinear medium), and can be estimated over the entire spectral range of the probe. However, this method has its drawbacks: cubic nonlinearities of typical liquids are extremely small and the Kerr effect competes with self-focusing and white-light continuum generation in the sample. Some traditional Kerr media, like CS_2 have a non-instantaneous contribution to the Kerr signal, which prevents their usage for IRF measurement in femtosecond time range. Upconversion of the white light signal in a nonlinear crystal by mixing it with the pump light is more easily achieved, whilst the signals are higher and easier to record. However, in this case, the measured IRF will differ from the one obtained in the actual pump-probe experiment, because the front window of the sample cell and the sample itself is replaced by the nonlinear crystal, which, presumably, has different propagation properties for the light in question.

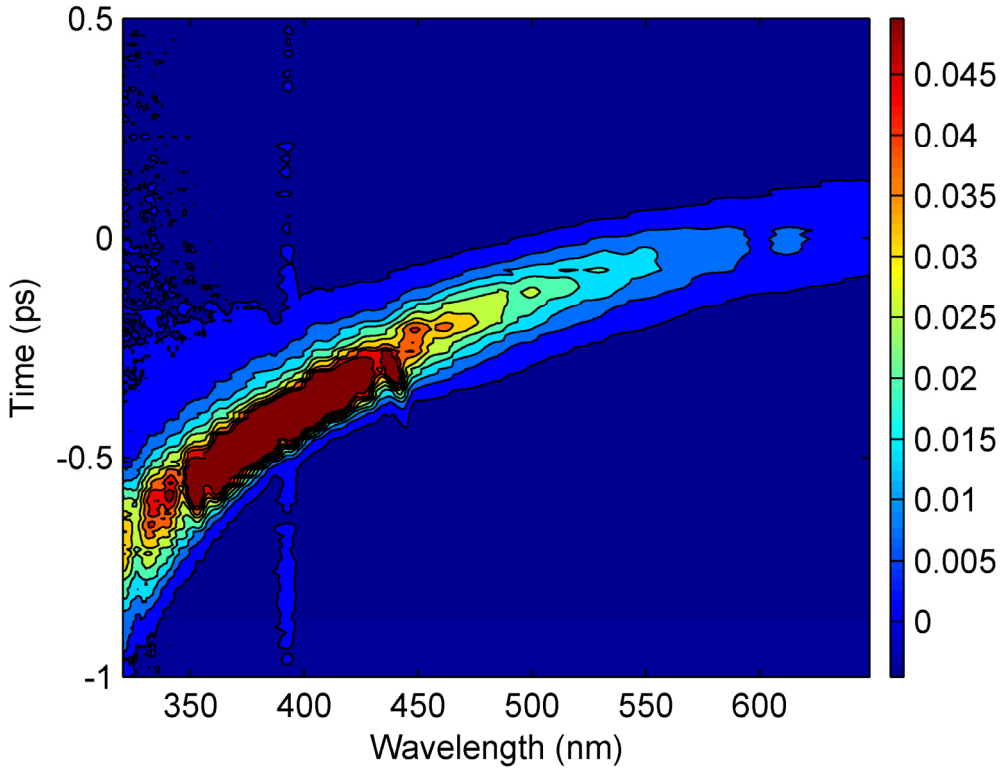

Figure 3.10 Optical Kerr effect measurement in MeCN with the 390 nm pump.

Another simple way of estimating the IRF and GVD of the setup is using the measured pump-probe data directly. If the molecules in the sample exhibit little femtosecond dynamics, the signal after the excitation follows the integral of the IRF profile:

$$PP(t,\lambda) \sim \int_{-\infty}^{t} IRF(\tau)d\tau \tag{3.4}$$

Thus, the instrument response of the setup can be estimated from the rise of the difference absorption signal and GVD from the time of the rise. Since not all the samples possess a slow response at all the wavelengths, usually it is enough to determine a single (if possible averaged over the spectrum) value of IRF. Figure 3.11 shows the pump-probe data measured on pNphe in acetonitrile solution after the excitation with 415 nm pump pulse. As it can be seen from the data, pump-probe signal is present across the entire spectral range and the instance where the half-rise of PP signal is observed can be interpreted

as the time-zero of the pump-probe signal. The derivative of the steepest rise of the signal in 375-475 nm range can then be used to represent the average IRF function of the setup at this particular arrangement. It must be noted, that the time-zero shift has a characteristic shape corresponding to the wavelength dependence of the refractive index of transparent media (relatively flat in the red part of the spectrum and increasingly steep towards the bluer wavelengths).

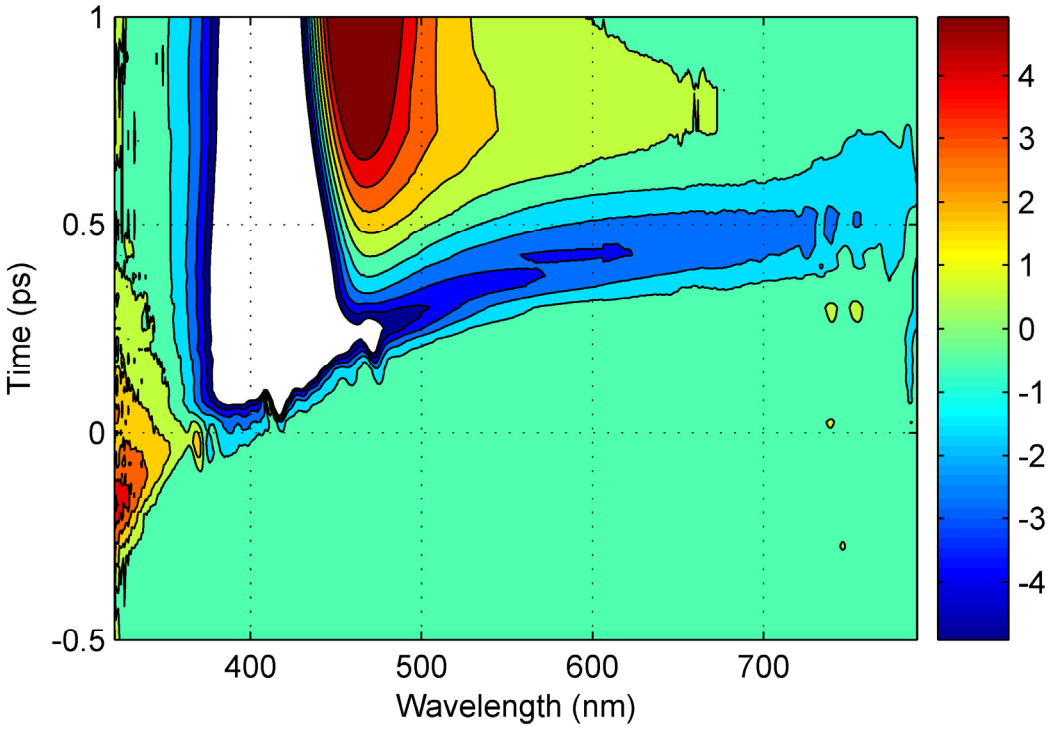

Figure 3.11 The rise of the pump-probe signal in pNphe dissolved in acetonitrile after the excitation with 415 nm pump pulse. Since the rise of the signal is present across the entire spectral range the GVD of the probe light can be easily estimated

The tests performed using all three methods for the measurement of IRF and GVD have revealed that direct estimation of GVD and average IRF from the pump-probe data is sufficiently accurate. Since such measurement requires no additional experiments other than the transient absorption of the investigated sample, in most cases it proved to be adequate and sufficient. And only if there are some major changes in the arrangement of the setup (especially in the while light

generation and transportation part) that we use the optical Kerr effect measurements to recalibrate IRF and GVD functions.

3.3.3. Spectral calibration

The spectral detection system used in the MPTAS spectrometer is home-built, and the spectral calibration is routinely performed in order to attribute wavelength values to the pixels of the diode array detector. To achieve this, a 3 mm thick holmium oxide glass plate is placed in the sample spot, and transmission spectrum is recorded. By contrasting it with the spectrum measured on a commercial spectrophotometer (Shimadziu UV-VIS-nIR 3101PC), wavelength calibration of the detector is performed. Since the dispersion of the imaging grating spectrograph is essentially linear in the spectral range covered, two parameters are sufficient to adequately calibrate the spectrum: the wavelength value of the first pixel (offset) and the number of nanometers per pixel (slope). The match between the calibrated holmium oxide glass absorption spectrum measured on the MPTAS spectrometer and the absorption spectrum measured using a commercial spectrophotometer is shown in Figure 3.12. As it can be seen from this picture the absorption peak wavelengths match within ca. 1 nm. Note that the deviations in absolute absorption values are cause by the lack of white light on the detector array (i.e. the white light continuum generated in CaF_2 crystal stretches only up to ca. 320 nm, hence making absorption measurements at shorter wavelengths unreliable; as well as the absorption peak around 380 nm is not properly reproduced due to very big absorbance[9]).

[9] Note that absorption of 2.5 OD corresponds to only ca. 0.3 % transmission, hence the transmitted light is attenuated practically down to the zero level.

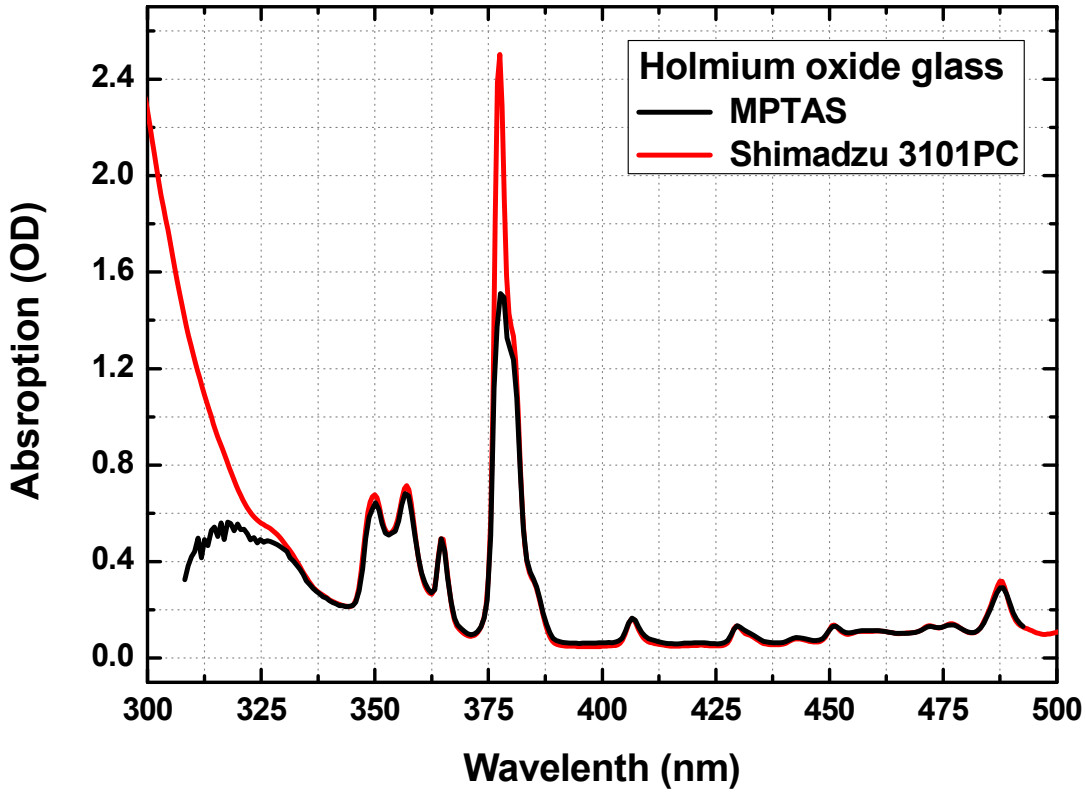

Figure 3.12 Absorption spectrum of holmium-oxide glass plate measured by the MPTAS spectrometer (black line) and commercial spectrophotometer after the spectral calibration. The recovered peak positions indicate the correctness of attribution of wavelength values to the pixels of the diode array.

3.4. Application: Excited and ground state dynamics of charge transfer membrane marker Laurdan

In this section, we demonstrate an application of the three-pulse spectrometer to investigate the ultrafast processes in biological membrane marker laurdan (6-dodecanoyl-2 dimethylaminonaphthalene). This molecule features a pronounced solvatochromism, which enables it to be used as a local structure- and temperature-sensitive probe in biological membranes [128-130]. The structural formula of laurdan is shown in the inset of Figure 3.13. As it can be seen form the formula, laurdan molecule comprises of a polar chromophoric group and non-polar aliphatic tail. These structural features enable an easy incorporation of laurdan in to the lipid bilayer. The active chromophoric group of laurdan is identical to that of prodan – another solvatochromic membrane probe dye widely used in solvation studies [131-134].

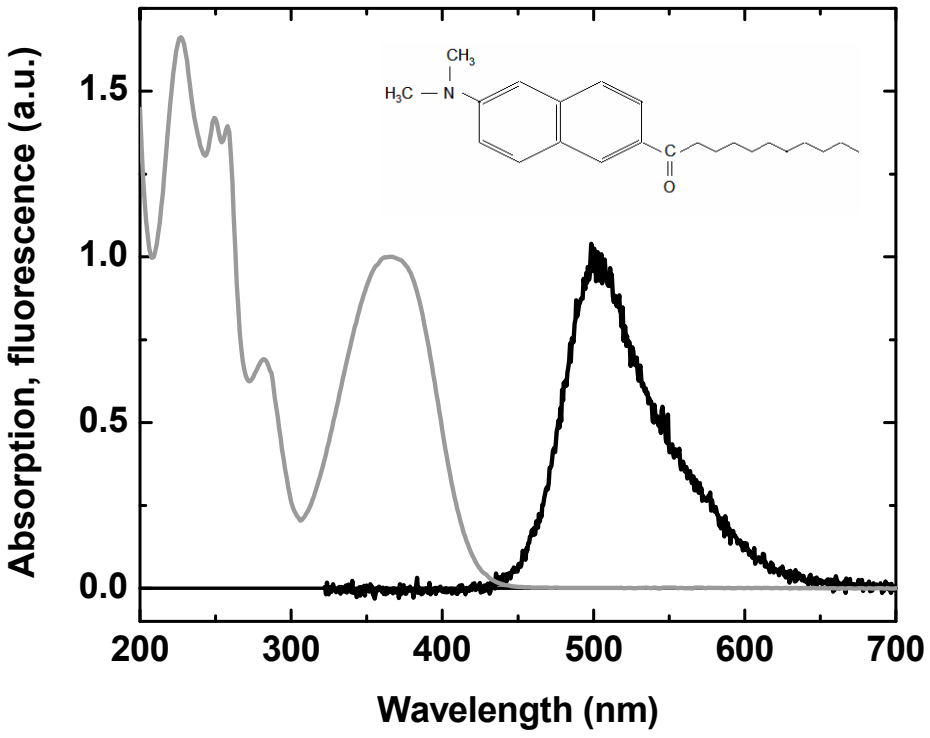

Figure 3.13 Absorption (gray line) and emission (black line) spectra together with the structural formula of membrane marker Laurdan in the methanol solution.

3.4.1. Experimental results

Absorption spectrum of laurdan dissolved in methanol peaks at ca 380 nm (Figure 3.13), whereas the fluorescence maximum is shifted by 7320 cm^{-1} to the red and lies at around 500 nm. This large stokes shift in polar solvents and the dependence of fluorescence peak wavelength on the solvent polarity were used as arguments indicating that a charge transfer state is mixed into laurdan excited state manifold [135]. Indeed, the structural formula suggests push-pull type of excited state charge transfer between the nitrogen and oxygen atoms situated on the different sides of the chromophoric groups. As will be evident from the multi-pulse transient absorption results (further in this section), our data supports this suggestion.

In this study, laurdan molecules were excited using 130 fs laser pulses with the wavelength centered at 380 nm (see section 3.2). This corresponds to the red wing of the lowest laurdan absorption band (Figure 3.13). The recorded pump-probe data are shown in Figure 3.14. The first observation that catches the eye, is the fact that time-evolution of stimulated emission (triangles in Figure 3.14 A) is fairly long: at the 510 nm wavelength corresponding to the emission peak (see at Figure 3.13), initially a weak positive signal is observed that quickly vanishes and continuously decreases further over several decades in time, reaching its minimum at ca. 100 ps, afterwards it relaxes back towards the zero (full decay is not observed at the time window of this experiment). At 440 nm wavelength (circles in Figure 3.14 A), an instantaneous negative signal is observed, which persists for several picoseconds, then increases over the time range of several tens of picoseconds and subsequently turns into a relatively weak induced absorption which hardly decays during the time window of the experiment. At 400 nm, wavelength that matches the absorption of

laurdan, instantaneous induced absorption is observed that grows slightly over 100 ps time scale and decays afterwards.

The ultrafast dynamics of laurdan is further illustrated by difference absorption spectra measured at different delay times after the excitation (Figure 3.14 B). Initial spectrum measured at 300 fs after the excitation (squares in Figure 3.14 B) consists of two bands: induced absorption peaking at ca. 390 nm and stimulated emission with the maximum at 450 nm. Weak induced absorption is also observed to the red from the stimulated emission band. Interestingly, the induced absorption band overwhelms the ground state bleaching signal that should be observed as a negative contribution to the difference absorption at the wavelengths, corresponding to the steady-state absorption spectrum of laurdan (compare to Figure 3.13). At later delays, the dynamics of difference absorption exhibits the red-shift and growth of the SE band accompanied by somewhat lesser increase and red shift of the induced absorption band. At 100 ps delay, the induced absorption band develops a shoulder at 450 nm. Note that the spectra measured at different delays lack an isosbestic point, indicating that the excited state dynamics is more complex than a simple transition between two excited state intermediates.

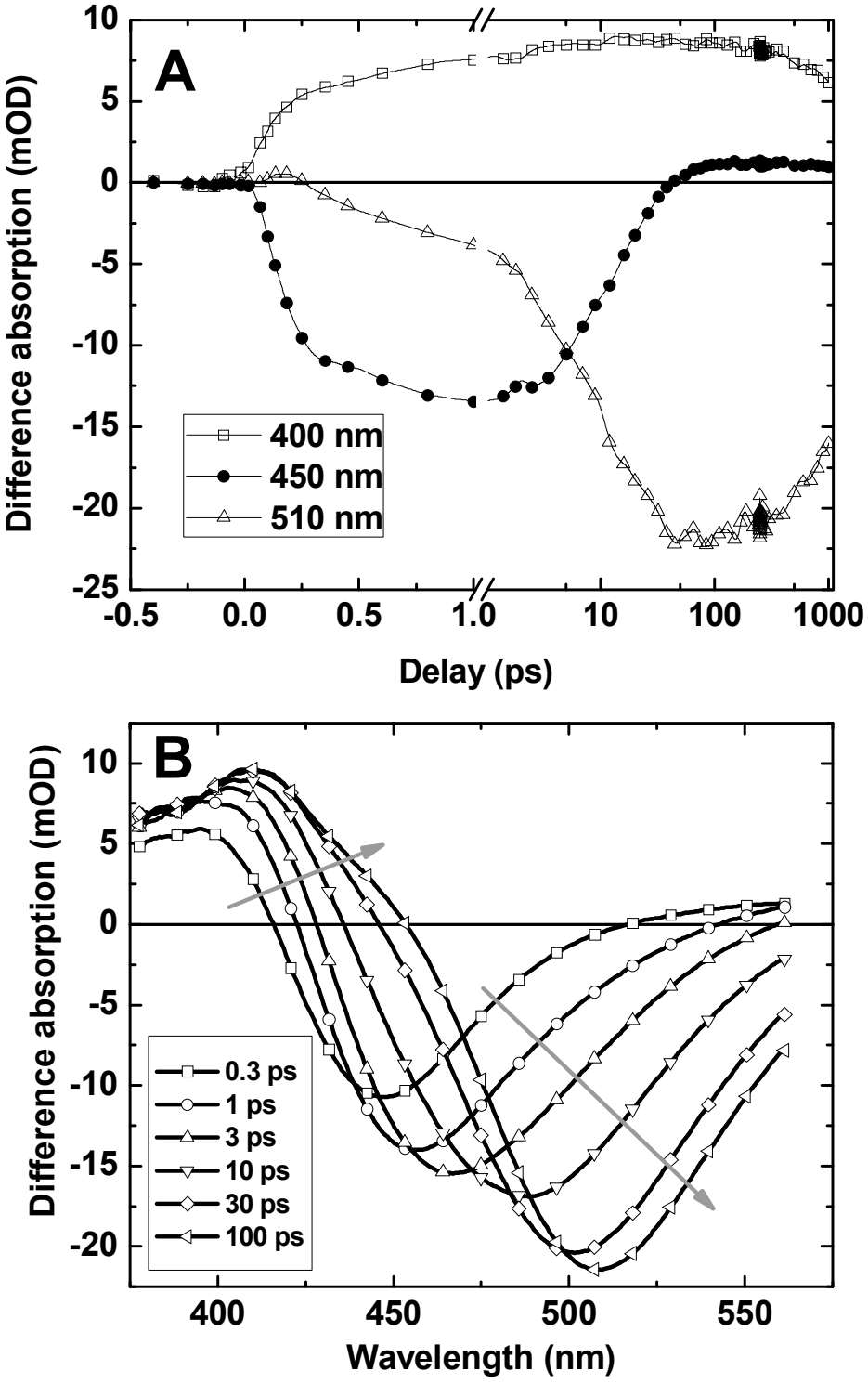

Figure 3.14 A: pump-probe traces measured on laurdan dissolved in methanol. Note that the time axis is linear up to 1 ps and logarithmic thereafter. B: difference absorption spectra measured at various delays after the excitation. Delay times are shown in the legend. Gray arrows indicate the observed trends.

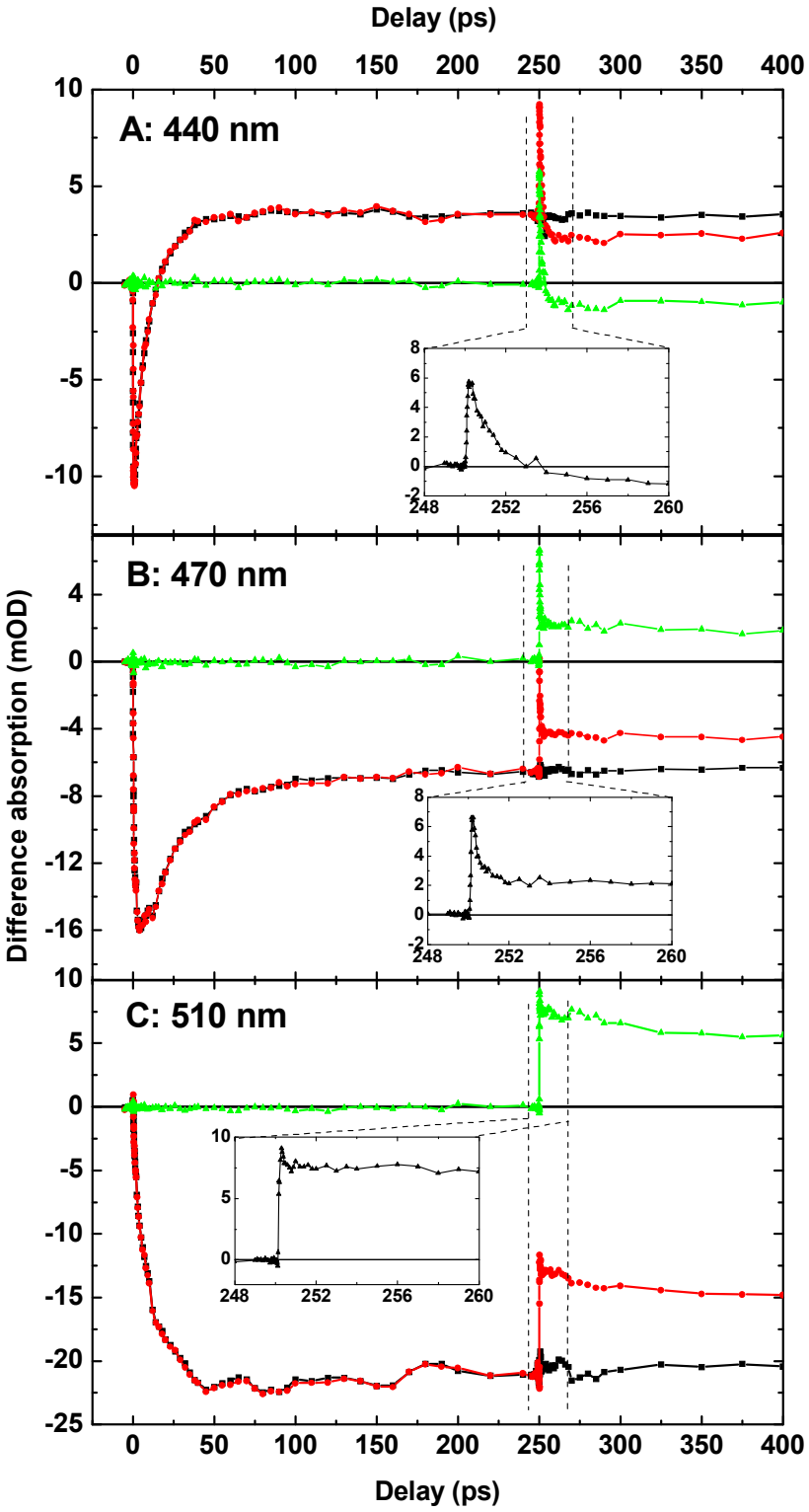

Figure 3.15 Selected pump-dump-probe traces on laurdan. Dump time is 250 ps after the pump. Black curves depict pump-probe data in the absence of the dump pulse, red curve show the difference absorption in the presence of dump pulse. Green curves depict the difference between the two signals (DΔOD = PDP-PP). The insets show the enlargement of time axis around the dump instance (only the double difference signal is shown). Probe wavelengths are indicated on the graphs.

To get further insight into the origin of the spectral dynamics of laurdan, additional actinic pulse was applied on the sample at 250 ps after the excitation. The wavelength of this additional pulse was tuned to 530 nm in order to interact selectively with the stimulated emission of the sample. At 250 ps after the excitation, the excited state of laurdan is equilibrated, and the dump pulse brings the population from the excited state to the ground state.

The transfer of population from the excited to ground state is best illustrated by pump-dump-probe (PDP) traces measured at 510 nm probe wavelength (Figure 3.15 C): at 250 ps, the pump-probe (PP) signal in the absence of the dump pulse remains virtually unchanged, whereas in the presence of dump, the difference absorption drops by ca. 35 %, indicating that the applied dump pulse is indeed diminishing the excited state population by this fraction. However, the action of the additional pulse is not as straightforward as this data might suggest. At wavelengths corresponding to the red wing of the induced absorption and the blue wing of stimulated emission (Figure 3.15 A and B respectively), the DΔOD (DΔOD = PDP-PP) signal indicates a transition process taking place within the first several picoseconds after the dump. At 440 nm, the induced absorption is not decreasing instantaneously, as would be the case if the dump pulse were simply returning the population to the original ground state. On the contrary, the amount of absorption momentarily increases (positive DΔOD) and subsequently decays below the PP signal in several picoseconds. At 470 nm, signal initially increases by an amount that it essentially becomes equal to zero. However, after ca. 1 ps part of the signal is recovered. Note that the rate of this recovery is different from the rate of the transition process observed at 440 nm. This is an indication that the signals result from the contribution of several spectrally distinct species.

3.4.2. Discussion and tentative interpretations

In pump-probe signals (Figure 3.14 B), shifting of spectral bands is observed, which takes several tens of picoseconds, the time scale compatible with solvation time scales in alcohols [134]. Solvation occurs when solvent molecules reorient to accommodate changed dipole moment and polarizability of the excited state. Such reorientation lowers the energy of the excited state and simultaneously increases the energy of the ground state, resulting in the red shift of stimulated emission (Figure 3.16). The fact that no isosbestic point is observed in the spectra is also compatible with the interpretation that the observed dynamics is due to solvation. Earlier fluorescence up-conversion and pump-probe studies have shown that solvation is a complex process that cannot be modeled using a two-state approach and should instead be approximated by a series of transitions among a continuum of states [13].

However, the bands not only change their positions, but also grow in amplitudes. Such growth may have two possible origins. The bands can increase because initially excited state absorption overlaps stimulated emission and, as the stimulated emission shifts to the red, the partial cancellation of the signals is removed and the intensity of observed bands increases. Another interpretation is that the dipole strength of the transition changes, which would imply the mixing in of a different state. Charge-transfer (CT) states were proposed as the candidates to explain solvatochromism of Laurdan [135]. Such a state could result in the change of the dipole moment of the excited molecule and thus increase the intensity of SE band. Additional argument in favor of the CT state contribution is the unusually large Stokes shift, exceeding 7000 cm^{-1}.

Irrespective, of which mechanism is governing excited state dynamics of laurdan, similar potential energy scheme can be used to

interpret observed PDP dynamics (Figure 3.16). Upon excitation, the molecule undergoes charge transfer and solvation, resulting in the red-shift and growth of the SE and induced absorption bands. Upon dumping, the population is transferred to an unrelaxed ground state, the configuration of which is not energetically optimal because of solvent orientation and/or intramolecular charge distribution. This unrelaxed ground state is responsible for instantaneous increase in absorption upon dumping, observed at 440 and 470 nm (Figure 3.15 A,B). Further this state relaxes to the original ground state leaving the smaller fraction of laurdan molecules in the excited state (see the pump-probe signals at 10 ps after the dump). At 510 nm, the unrelaxed ground state shows no absorption, and there the signal purely reflects the population of the excited state. The fact that the rate of this relaxation is wavelength-dependent indicates that, similarly to the dynamics observed after the pump, this is not a simple transition between two states. It must be noted that this transition is in fact a dynamic process taking place on intricate multi-dimensional potential energy surfaces of ground- and excited states (two obvious coordinates are solvent orientation and the amount of intramolecular charge transfer) and hence the processes in the excited state need not be exactly mirrored by those in the ground state. Quantitative analysis of dump-induced dynamics [109, 136] [137] combined with molecular modeling of the excitation and de-excitation processes [138, 139] can be used to get further insight into ground-state charge redistribution and solvation dynamics.

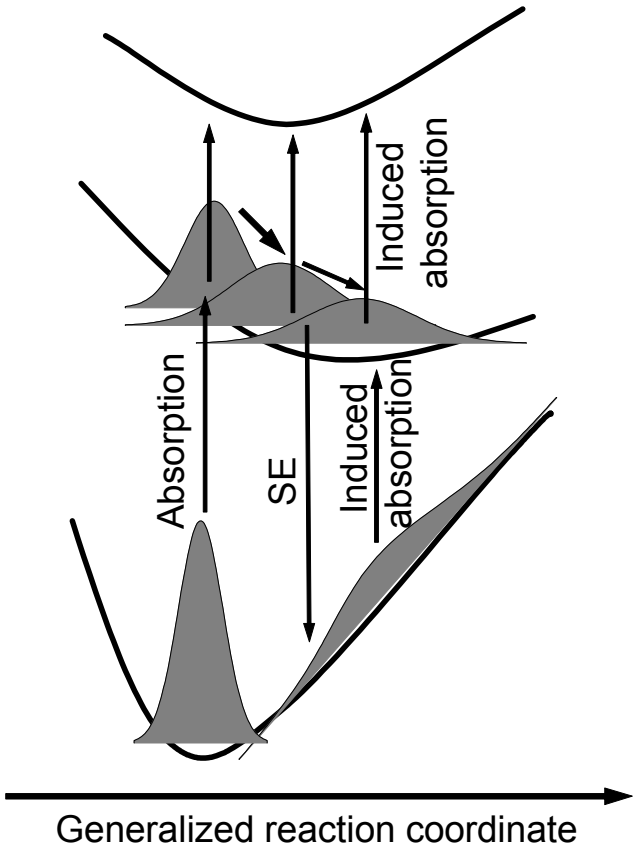

Figure 3.16 Simplified potential energy scheme used to interpret the pump-dump-probe spectroscopic results on laurdan.

4. Ultrafast dynamics of photochrome based on oxazine ring opening

In this chapter a femtosecond pump-probe and nanosecond flash-photolysis measurements on a new type of photochromic molecules are presented. These photochromes incorporate an indolo[2,1-*b*][1,3]benzoxazine ring system which opens upon UV light excitation and closes back within a few tens of ns. The details of ring opening and spectral properties of the photoproducts have been studied by investigating the spectral signatures of the model compounds, representing separate structural parts of the photochromic switch. Comparison of the photoinduced dynamics of the model compounds and those of photochromic molecule has revealed a detailed molecular picture of the light-driven switch function.

4.1. Introduction

Despite the early discovery of photochromism [140, 141] and continuous research efforts in this field [142-146], photochromic molecular compounds still attract ample attention due to their distinctive properties. These include the ability to change absorption spectra and/or refractive index [147], modulating molecular fluorescence yield [148] and optically inducing structural changes in supramolecular complexes [149-151]. All these modifications are reversible via thermal back conversion or upon exposure to a light of different wavelength. Essential mechanism responsible for these photoinitiated changes in photochromic compounds are: transformation in isomerization, intramolecular proton transfer, chemical bond cleavage or other stereoelectronic modifications [152]. Due to unimolecular character of photochromic transformation, these compounds were proposed to be

used for high-density optical data storage, or molecular-scale optoelectronic devices [153].

One of the newly synthesized [154-156] groups of photochromic compounds are indolo[2,1-*b*][1,3]benzoxazines. These photochromes undergo a fast C–O bond cleavage upon UV excitation which results in the formation of two distinct chromophoric groups [157, 158]. A broken C–O bond causes a formation of π-bond between nitrogen and chiral carbon atom, thus extending the conjugated system of 3*H*-indolium. Additionally, the broken bond enables the formation of 4-nitrophenolate anion which is able to absorb visible light at ca. 430 nm [155]. These photochromes revert thermally back to their initial state within ten-to-few hundred nanoseconds[10] after the excitation, and C–O bond re-forms [159]. This "on-off" switching time is one of the fastest among the photochromic compounds. Another noticeable feature of these photochroms is an excellent fatigue resistance, which allows thousands of switching cycles with no apparent sign of degradation [159].

In this chapter, we present a study on a compound with the simplest chemical structure from the group of indolo[2,1-*b*][1,3]benzoxazines (IB1 in Figure 4.1). Recently it was shown [157, 159] that absorption spectra of IB1 in its opened (IB1b) and closed (IB1a) ring configurations can be sufficiently well understood as a combination of spectral features characteristic to its constituent moieties. Thus, in our transient absorption studies, we compare ultrafast responses of IB1 with the ones of its model compounds, representing two chromophoric groups comprising the photoswitch. To our knowledge, this is the first attempt to investigate ultrafast dynamics in the family of indolo[2,1-*b*][1,3]benzoxazine photochromes.

[10] Note that presented lifetimes are for photochromes in solution, once these molecules are incorporated in polymer matrixes, back-switching durations increase by 3-4 orders of magnitude.

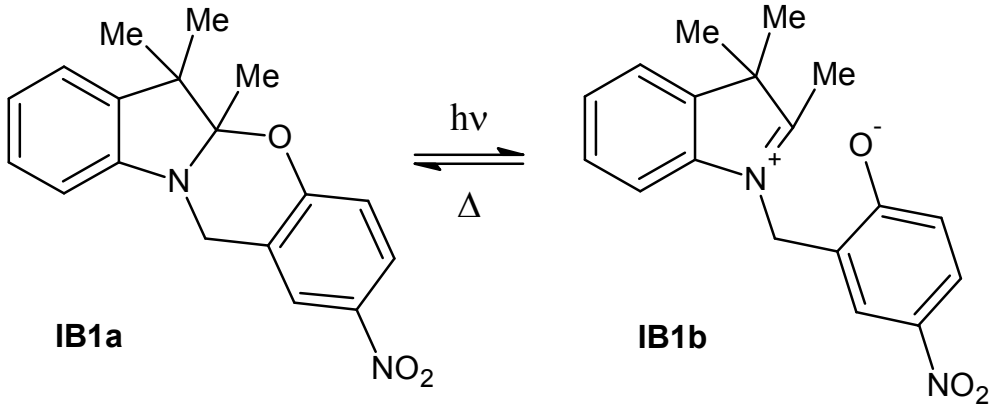

Figure 4.1 UV-induced reversible interconversion of indolo[2,1-*b*][1,3]benzoxazine IB1a to zwitterion IB1b.

4.2. Materials and methods

4.2.1. Sample preparation

Acetonitrile (MeCN) was purchased from Sigma-Aldrich (gradient grade) and used as received. 1,2,3,3-Tetramethyl-3*H*-indolium iodide (IndI in Figure 4.4) was synthesized by alkylation of 2,3,3-trimethyl-3*H*-indole with iodomethane and recrystallized from ethanol. IndI solution in MeCN was used as a model system for 3*H*-indolium cation of IB1b. The concentration was adjusted to have optical density of ca. 0.8 of the sample at the excitation wavelength (Figure 4.4). 4-nitrophenol was also purchased from Sigma-Aldrich and in order to prepare sodium 4-nitrophenolate solution in MeCN, powdered 4-nitrophenol was dissolved in MeCN (pNph, Figure 4.4) and dry sodium carbonate was added to the solution to deprotonate the phenolic hydroxyl group of pNph. After the filtration of precipitates, this yielded a solution of possessing sodium 4-nitrophenolate (pNphe in Figure 4.4) chromophore. pNph and pNphe were used as model systems for closed (IB1a) and opened (IB1b) forms of IB1 nitrophenol moiety [159]. The concentrations of pNph and pNphe solutions, used in our experiments, were 0.5 and 0.25 mM respectively. Photochromic compound IB1a (5a,6,6-trimethyl-2-nitro-

5a,6-dihydro-12*H*-indolo[2,1-*b*][1,3]benzoxazine) was synthesized according to the procedure described earlier [154]. Solutions of IB1a in MeCN with the corresponding concentrations of ~ 0.8 mM and 1.9 mM were used respectively for fs pump-probe and ns flash photolysis measurements. All the spectroscopic measurements presented in this study were carried out at room temperature, with the samples stored in closed fused silica cells of 1 mm pathlength.

4.2.2. Steady-state spectra

Steady-state absorption spectra were measured using a scanning spectrophotometer (Shimadzu UV-3101PC). Fluorescence spectra were measured by exiting sample with a laser radiation and collecting the emission light into a fiber-optic spectrometer (Avantes AvaSpec-2048).

4.2.3. Pump-probe measurements

Detailed description of the pump-probe setup is presented in chapter 3, while here only a short reminder is given. For pump-probe measurements we have used a home-built transient absorption spectrometer backed by the femtosecond laser system (Spectra-Physics, Spitfire), which delivered 1 mJ pulses with the duration of 130 fs at 1 kHz repetition rate. The wavelength of generated radiation was centered at 805 nm, the spectral bandwidth was ~ 150 cm^{-1}. Optical parametric amplifier (OPA) (TOPAS, Light Conversion) was used to obtain tunable pump pulses matching the sample absorption spectrum. White-light continuum, generated by focusing a weak 805-nm beam into a CaF_2 crystal (Figure 3.7), was used as a broadband probe. Group velocity dispersion within the probe pulse was characterized by optical Kerr effect in MeCN (see Figure 3.10). The obtained dispersion

curve was further refined in the global analysis procedure used to analyze the data. In all figures, the presented data is corrected for the dispersion of the probe light. Temporal delay between the pump and probe pulses was varied by changing the optical path length traveled by the probe pulse that was sent to the hollow retroreflector placed on computer-controlled linear translation stage. Polarizations of pump and probe beams were linear and set to be at the magic angle (54.7°) with respect to each other. Both beams were focused into the sample with the probe diameter set to ~ 80 μm and pump being roughly 3 times larger (Figure 3.9). The probe light transmitted through the sample was dispersed using an imaging spectrograph and recorded by linear-array detector (Hamamatsu). Collected spectra had an average noise level of < 0.5 mOD, with an exception of 725-800 region where the noise was 2-3 mOD. This increase in the noise was caused by the instabilities of the white-light continuum that become more pronounced in the spectral proximity of the driving 805-nm pulse. Within one experimental time point, ca. 5000 white light spectra were averaged and difference absorption spectrum was calculated. A typical dataset contained 512 spectral points and ca. 120 time points. Steady-state absorption spectra collected before and after each experiment did not show any substantial signs of photo-degradation.

4.2.4. Flash photolysis measurements

Flash photolysis setup, used in our experiments, is presented in Figure 4.2. In these measurements sample was excited by exposing it to the 4th harmonic of nanosecond Nd:YAG laser (Ekspla NL301). The pulse energy and excitation wavelength was respectively 6 mJ and 266 nm. Samples were exposed to an unfocused laser beam with the diameter of ca. 2.6 mm. Light flashes with the duration of ~ 100 μs

produced by the laser-synchronized Xe flash lamp were used to strobe the sample transmission, whilst temporal changes in its absorption spectra were detected using a monochromator, behind which a high-speed photodiode was placed and connected to a 1 GHz bandwidth oscilloscope (Tektronix TDS 7104). Another photodiode monitored the excitation pulse and was used to trigger the oscilloscope. Temporal resolution of these measurements was limited by the duration of laser pulses in use, and was approximately 4-5 ns. All the nanosecond kinetic traces presented in this chapter are averaged from 20 single shot measurements.

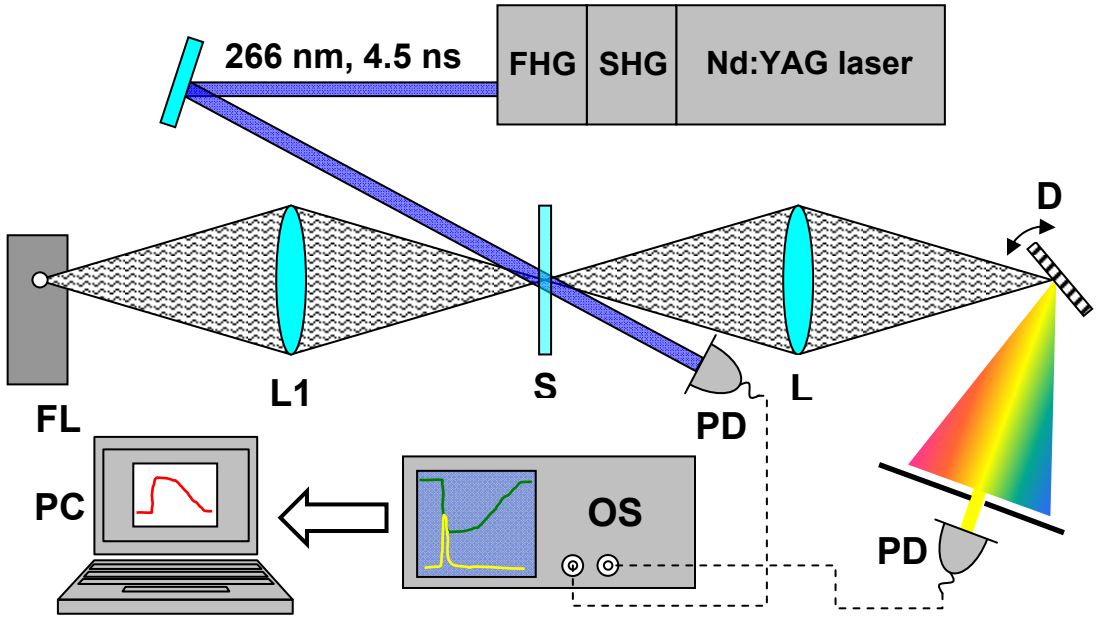

Figure 4.2 Optical layout of the flash photolysis setup. SHG and FHG – laser modules generating 2nd and 4th harmonics; FL – pulsed Xe flash lamp; L1, L2 – lenses; S – sample quvette; DG – diffraction grating; PD1 and PD2 – trigger and sample photodiodes; OSC – 1GHz oscilloscope; PC – computer.

4.2.5. Procedures for the data analysis

The collected time-resolved spectra and traces were analyzed using global analysis techniques described before [160, 161]. In short, a certain discrete number of compartments, connected in between by

linear rate kinetics, are assumed as a model system for the data to be fitted. The excitation populates one or several of these compartments, and as time passes, compartment populations are redistributed according to the assumed connectivity scheme. Free parameters of the fit are rates of redistribution between particular compartments and spectra assigned to a certain compartment. For simplicity, data presented in this paper was fitted using a sequential (evolutionary) model, where different compartments are characterized by time-dependent concentrations $c_i(t)$ and evolve in series (i.e. $c_1(t) \rightarrow c_2(t) \rightarrow \ldots$ see Figure 4.3). These concentrations are described by the following system of differential equations:

$$\begin{aligned} \frac{d}{dt}c_1(t) &= I(t) - \frac{1}{\tau_1}c_1(t), \\ \frac{d}{dt}c_i(t) &= \frac{1}{\tau_{i-1}}c_{i-1}(t) - \frac{1}{\tau_i}c_i(t), \; i \neq 1 \end{aligned} \tag{4.1}$$

and the model function used to fit the data is

$$F(t,\lambda) = \sum_{i=1}^{n} c_i(t)\sigma_i(\lambda). \tag{4.2}$$

Here τ_i is the lifetime of *i-th* compartment (a decay rate with witch it transforms to the *i+1* one), $I(t)$ is the input of the system, which populates only the first compartment and has a Gaussian profile with FWHM equal to the instrument response function (IRF), and $\sigma_i(\lambda)$ is a species associated difference spectrum (SADS) of *i-th* compartment. The number of compartments *n* was set to the smallest one which yielded a fit with all the features of spectral dynamics present in collected data. This specific way of fitting, should not be seen as an implication that our measured data results from the system governed by a sequential dynamics, but rather it should be regarded as a convenient way of parametrizing and presenting the vast amount of experimental data.

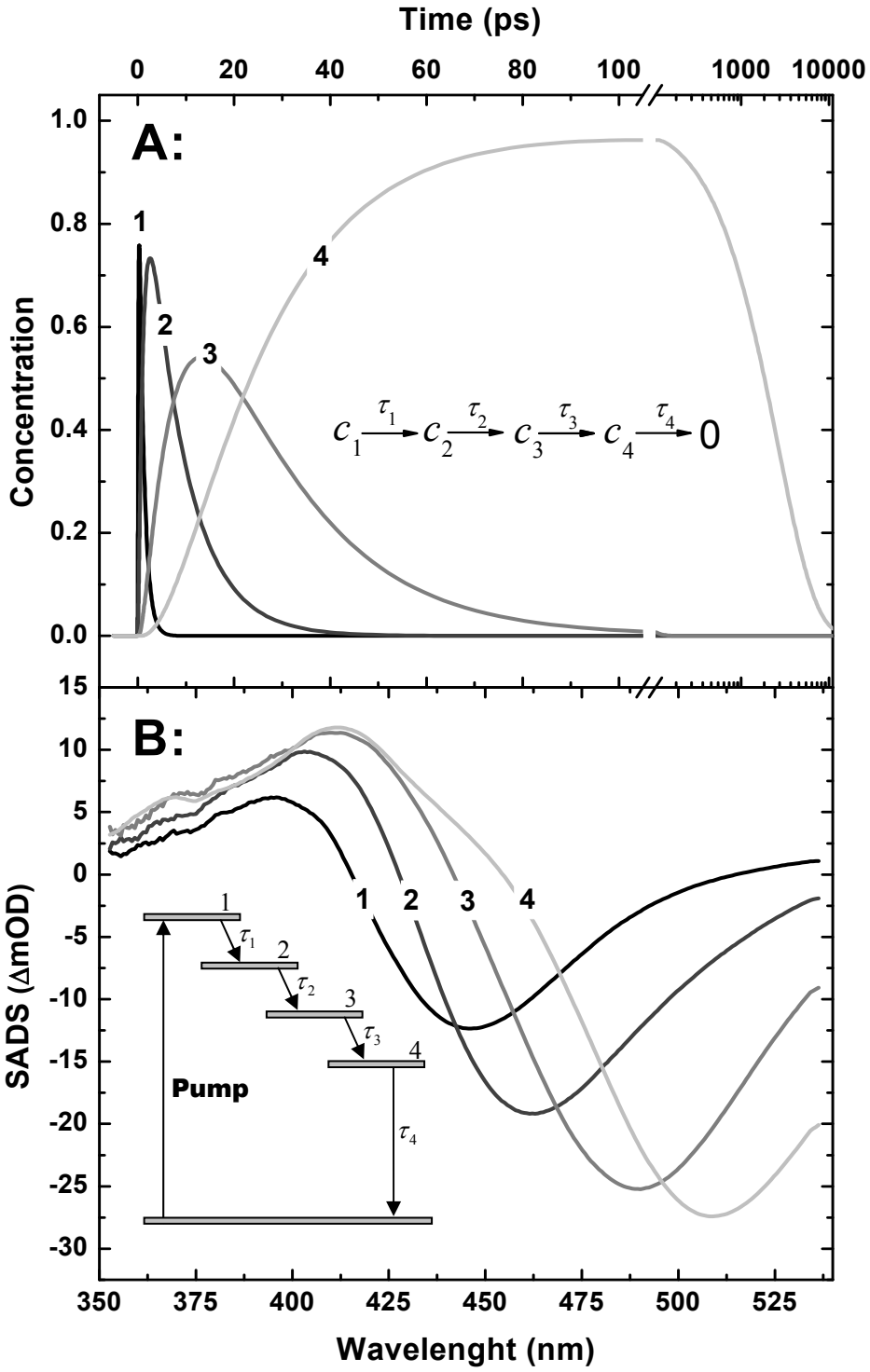

Figure 4.3 Global analysis of the time-resolved spectrum assuming four-compartment sequential model. A: time dependencies of the concentration of different compartments. B: the resulting species associated difference spectra (SADS) for different compartments in the spectral evolution. The connectivity schemes of sequential model are shown in the insets.

4.3. Results and discussion

4.3.1. Steady-state absorption and fluorescence spectra

Absorption and fluorescence spectra of the investigated compounds together with their structural formulae are presented in Figure 4.4. The top part of the figure depicts absorption (*a*) and emission (*c*) spectra of IndI. Two overlapping bands are observed in the absorption spectrum: a relatively weak one with the maximum at ca. 278 nm and another one, almost 3 times stronger, peaking around 247 nm. Photostability tests using the pump light of the pump-probe experiments have revealed that these bands are quite distinct in their photodynamics: an excitation of IndI at 247 nm causes some 2 to 3 orders of magnitude faster sample degradation while comparing it with a photo-excitation of 278-nm band in an optically matched IndI sample. Moreover, the position of this band corresponds to the absorption of iodine anion and is due to its charge-transfer-to-solvent band ($^2P_{3/2}$) in MeCN [162, 163]. The red edge of this band in MeCN is ca. 270 nm, thus the absorption of the lowest lying band (278 nm) can be attributed only to 3*H*-indolium cation. Only this band was excited while conducting our experiments (see the spectrum of excitation pulse in Figure 4.4, top panel). Fluorescence spectrum of 3*H*-indolium peaks around 375 nm, which corresponds to a Stokes shift of 9300 cm^{-1}.

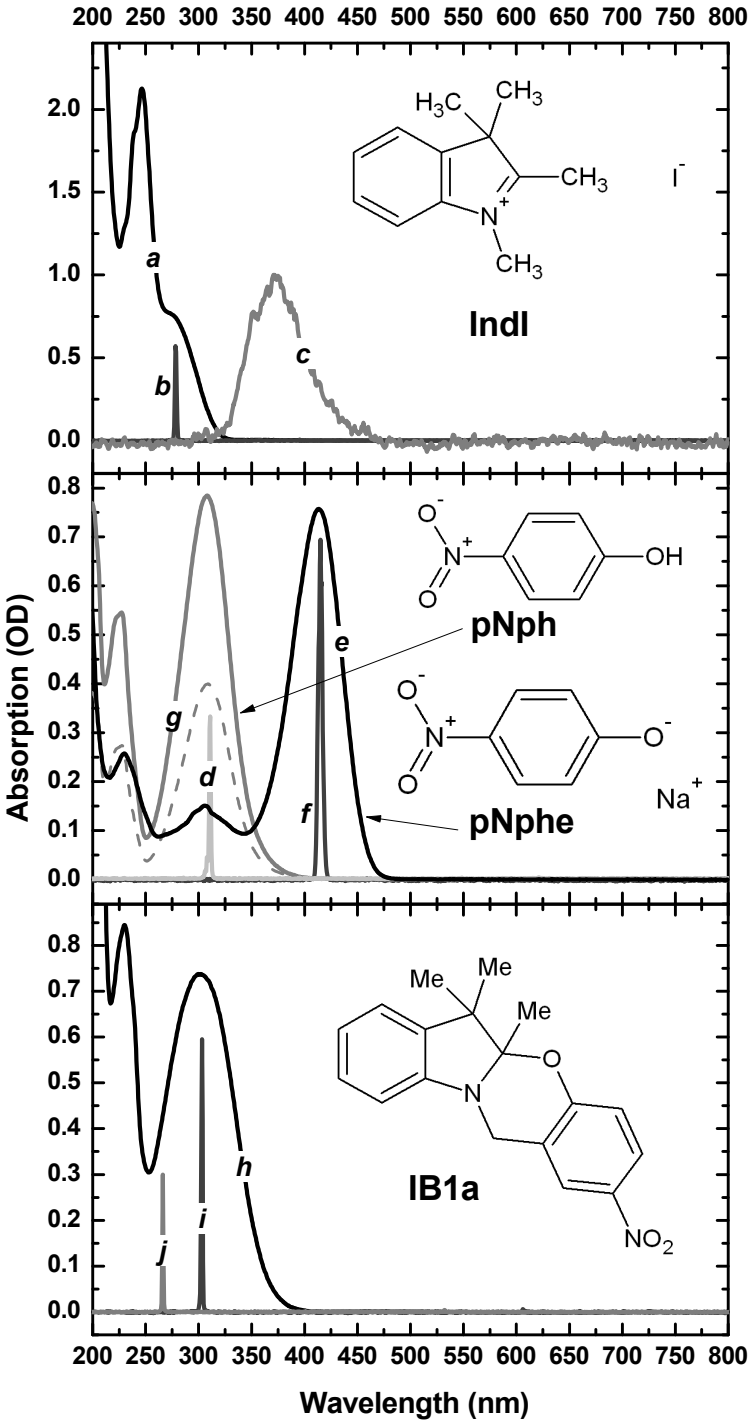

Figure 4.4 Steady-state absorption and emission spectra and structural formulae of investigated compounds. Top graph: absorption (*a*), fs excitation pulse (*b*) and fluorescence (*c*) spectra of Indolium iodide (IndI) dissolved in MeCN. Middle graph: steady-state sample absorption spectra of 4-nitrophenol (pNph, *g*) and 4-nitrophenolate (pNphe, *e*), the wavelengths of pump light used in pump probe experiments on pNph and pNphe respectively (*d* and *f*). Dashed line is pNph absorption with the concentration identical to that of pNphe sample. Lower graph: steady-stare absorption spectra (*h*) and structural formula of photochromic compound IB1a. The excitation laser wavelengths for fs pump-probe (*i*) and ns flash photolysis (*j*) experiments are displayed.

Curves *g* and *e* in Figure 4.4 depict the absorption spectra of pNph and pNphe. Evidently, the deprotonation of pNph and the formation of pNphe produces a significant red shift in its absorption spectrum: the peak of red-most band from 309 to 415 nm, which corresponds to the decrease in the excitation energy by 3250 cm^{-1}. From the comparison of the spectra of these two species at equal concentrations (dashed line and *e* line in Figure 4.4), it is clear, that twofold increase in a maximum extinction coefficient is associated with aforementioned deprotonation reaction of pNph.

Absorption spectrum of IB1a is dominated by two distinct bands at 230 and 302 nm. The 302 nm band qualitatively coincides with pNph absorption. Indeed, it is usually assumed in the literature that the conjugated systems of two chromophoric groups of IB1a molecule do not interact strongly [159]. The pNph absorption maximum is at 309 nm (*g*, Figure 4.4 and [159]) and its extinction coefficient is ~10 $mM^{-1}cm^{-1}$. Meanwhile, the reported values of these numbers for Indoline (a model compound for IB1a moiety) are (λ_{max} ~290 nm and ε ~2 $mM^{-1}cm^{-1}$) [159, 164]. Obviously, the 302 nm absorption band of IB1a is dominated by pNph moiety with some minor influence of Indoline part.

4.3.2. Pump-probe on Indolium iodide (IndI)

For IndI pumping we have used a 278-nm OPA output with the bandwidth of 230 cm^{-1} (Figure 4.4, *b*). Pump pulse energy was ~ 500 nJ and estimated instrument response function (IRF), for this configuration, was around 280 fs. Representative pump-probe traces and spectra are displayed in Figure 4.5 A and B.

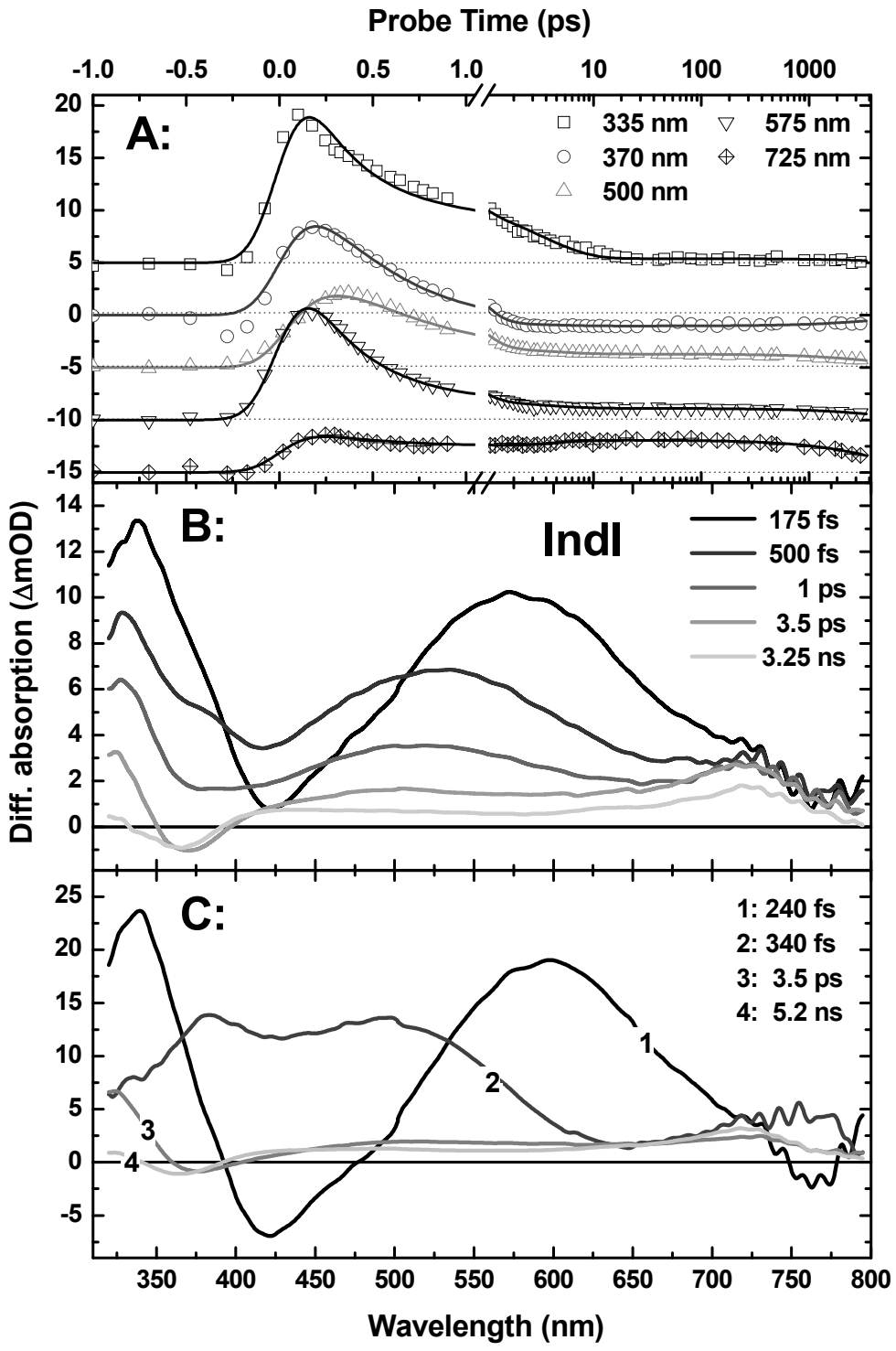

Figure 4.5 Measured and fitted data of Indolium iodide (IndI) A: pump-probe traces for different probe wavelengths (points), with global analysis fit on measured data (solid lines). Experimental and fitted traces were offset vertically to aid the viewing. Doted lines show the real zero-level for appropriate trace. B: time-gated pump-probe spectra measured at various delays (indicated in the legend) after the excitation. C: species associated difference spectra (SADS) from the global analysis fit based on four-compartment sequential model. Time constants associated with corresponding SADS are depicted in the legend.

From the spectra shown in Figure 4.5 B, it is evident that femtosecond dynamics of IndI is dominated by two induced absorption bands which are formed within sub-IRF time scale. These two bands exhibit different behavior: the first band appears at 337 nm and within its decay time of ca. 10 ps (Figure 4.5 A, open squares) gradually shifts by 12 nm to the blue, whilst the second one appears at 580 nm, rapidly, within 200-500 fs, shifts to ca. 528 nm and then steadily vanishes. The shifting of second band can also be observed in the kinetic traces; 500-nm trace gradually increases within 500 fs after excitation, while other traces follow more or less instrument response limited growth. In the transient absorption spectra measured on picosecond time scales, broad induced absorption (IA) plateau is observed stretching over the region of 400-800 nm, with an additional IA band peaking at around 725 nm. At times after ca. 2 ps, a negative band appears at ca. 365 nm. Its position roughly corresponds to the peak of IndI fluorescence spectrum (curve *c* in Figure 4.4), indicating that this band can be attributed to stimulated emission (SE) of IndI. Note that this band overlaps with IA plateau and this can cause additional distortion or small conceivable shift.

The vast amount of presented experimental data in this and subsequent sections, together with the complexity of transient dynamics in the investigated systems, clearly requires more concise presentation of all the measured data, not just selected ones, to aid the interpretations. Thus here and further we have used global fitting procedures to systematize and compare experimental results (see section 4.2.5). The analysis results for all investigated compounds, in the form of SADS and their lifetimes, are presented together with collected data in the ‘C’ parts of Figure 4.5 to Figure 4.9. The quality of the fit can roughly be judged from the match between fitted (solid lines) and measured kinetic traces shown in the ‘A’ parts of corresponding Figures.

The initial, IRF limited, transient absorption spectrum of our IndI sample (Figure 4.5 B), surprisingly well reproduces the $S_1 \rightarrow S_n$ absorption of indole radical cation (Indolyl) in aqueous environment, which has been observed by various spectroscopic methods [165-167]. Although indolyl radical and 3*H*-indolium cation investigated here are not exactly the same molecules, but the sizes and structures of their conjugated systems are similar, thus presumably leading to a close match between the excited state absorption (ESA) spectra. Another observation that can immediately be made from the spectra is the similarity between the 500-fs time-gated spectrum in Figure 4.5 B and transient absorption spectrum of 3*H*-indolium cation in low-pH solution, reported earlier by Jovanovic and Steenken [166]. The fact that the spectral shifts observed on the ultrafast time scales are comparable to those induced by the changes of solvent pH, could indicate that our sample undergoes substantial charge redistribution in the excited state. Alternatively, the observed spectral dynamics could be due to the relaxation among different electronic states in the excited state manifold. In this case, the late spectra (curves 3 and 4 in Figure 4.5 C) would correspond to the relaxed S_1 state as indicated by the SE band. The stimulated emission observed in the SADS of these compartments is accompanied by a featureless absorption plateau stretching from 425 to 725 nm. This plateau could be attributed to the absorption of dimer anion of MeCN [168], which is formed upon photoionization of IndI, when the selected electron is trapped by two solvent molecules.

4.3.3. Pump-probe on 4-Nitrophenol and 4-Nitrophenolate (pNph & pNphe)

Excitation of pNph was performed using 311-nm (~ 170 cm^{-1} bandwidth) wavelength and 500 nJ energy fs laser pulses with an estimated IRF of 215 fs. Selected pump-probe data are presented in

the Figure 4.6 A and B. Here, in the initial spectrum, corresponding to 125 fs probe delay, a sharp negative peak is observed around 342 nm. Its wavelength corresponds to the Stokes shifted pump wavelength (the strongest vibrational band in acetonitrile lies at 2940.8 cm^{-1} [169]), which, together with the fact that the band is only observed during the time-overlap of pump and probe pulses, show that the band is due to the impulsive Raman scattering of the pump. Another spectral feature, which appears in the first time-gated spectrum and is more pronounced in the consecutive one of 400 fs, is a wide induced absorption band in 350-650 nm range with a pronounced peak around 500 nm. The signal below 350 nm is negative. This decrease in absorbance matches the red edge of steady-state absorption and is due to the ground state bleaching (GSB). On picosecond time scales, IA additionally extends to the red (up to 800 nm) and 500-nm band vanishes within ~ 12 ps (open-down-triangle trace in Figure 4.6 A). At 45-ps after the excitation, double band structure becomes evident in the spectrum, with peaks around 400 and 470 nm, on top of wide absorption region dominating the visible and near-infrared parts of spectrum. At later times, pNph has no apparent spectral redistribution and all spectral components simultaneously decay within ~3 ns. This can be seen clearly in the kinetic traces, where the decay of GSB band (open squares in Figure 4.6 A) indicates the return to the original ground state.

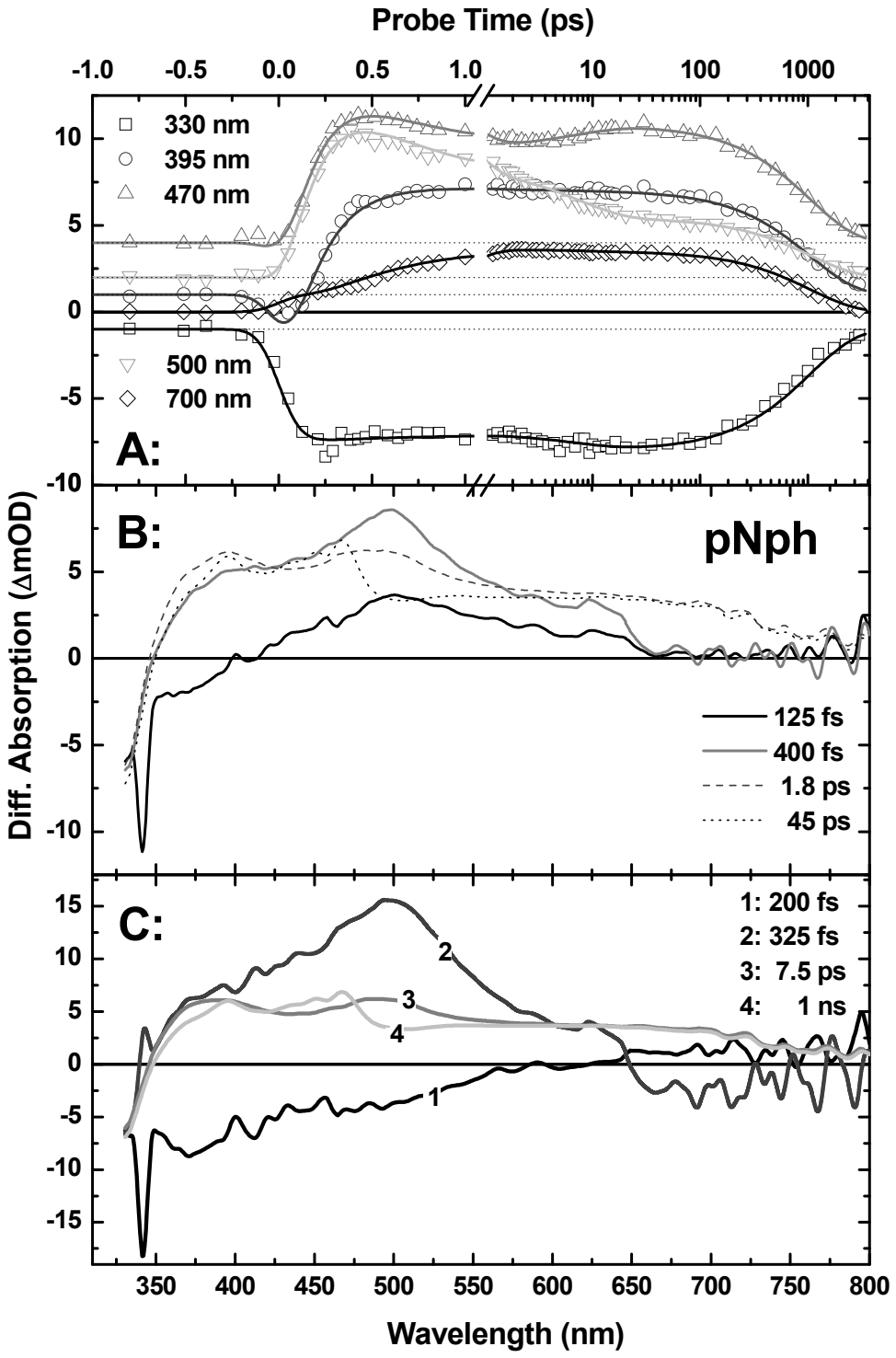

Figure 4.6 Measured and fitted data of 4-nitrophenol (pNph) chromophore A: pump-probe traces for different probe wavelengths (points), with global analysis fit on measured data (solid lines). For clarity, all pNph kinetic curves together with the fits were offset by 1 or 2 mOD, while doted-lines were added to illustrate the zero-levels. B: time-gated pump-probe spectra measured at various delays (indicated in the legend) after the excitation. C: species associated difference spectra (SADS) from the global analysis fit based on four-compartment sequential model. Time constants associated with corresponding SADS are depicted in the legend.

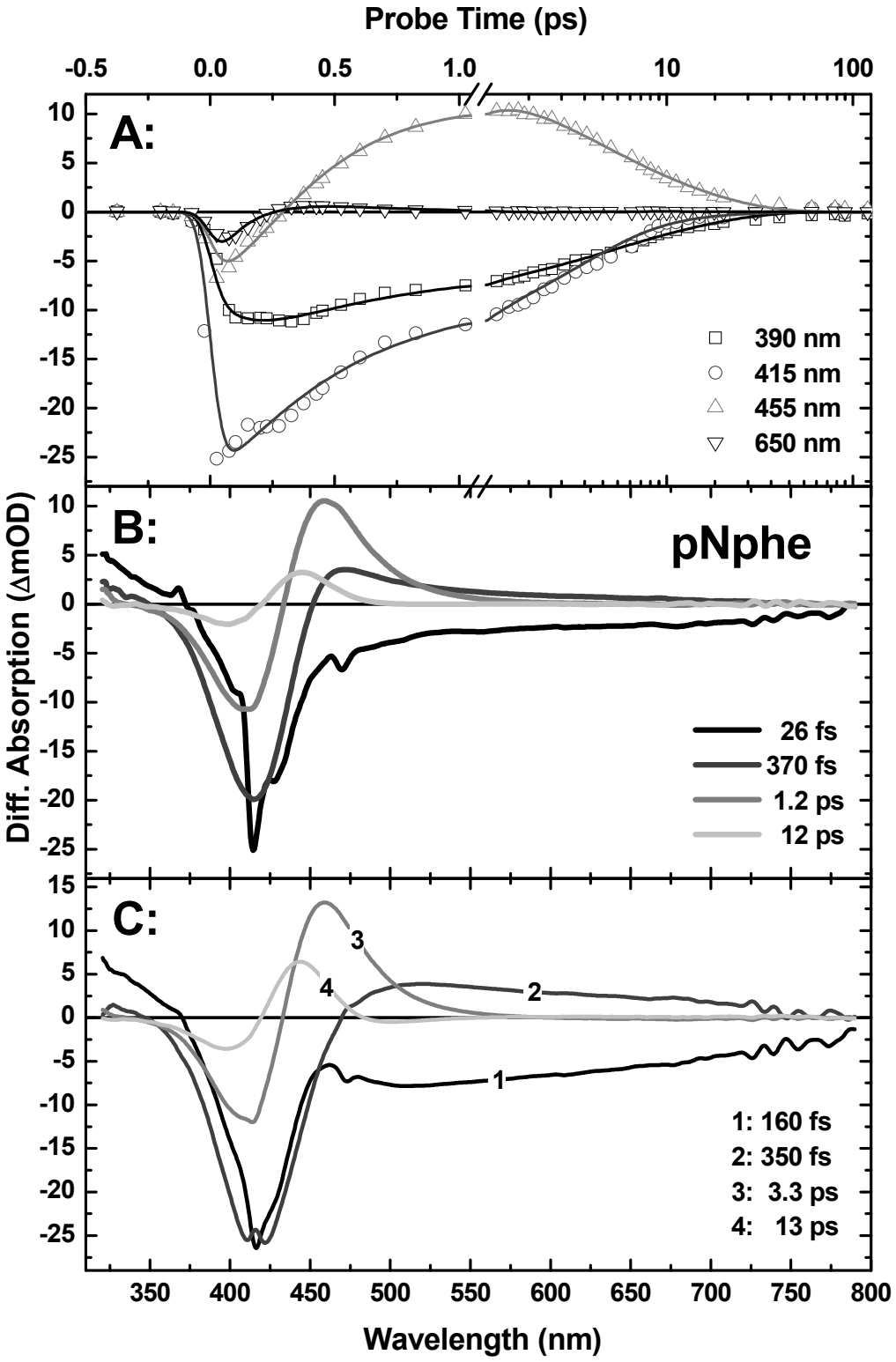

Figure 4.7 Measured and fitted data of 4-nitrophenolate (pNphe) chromophore A: pump-probe traces for different probe wavelengths (points), with global analysis fit on measured data (solid lines). B: time-gated pump-probe spectra measured at various delays (indicated in the legend) after the excitation. C: species associated difference spectra (SADS) from the global analysis fit based on four-compartment sequential model. Time constants associated with corresponding SADS are depicted in the legend.

The fitting of pNph data has allowed attributing the exact timescales to the observed dynamic processes (Figure 4.6 C). Qualitatively, the spectral relaxation is as described above. Distinct feature of pNph dynamics is the appearance of 500-nm band absorption, 200 fs past the excitation, and its subsequent decay extending into the second and third fit compartments (Figure 4.6 C). Another noticeable aspect is the constant amplitude of all SADS in the wavelength region corresponding to GSB. This indicates that all the spectral redistributions prior to the 4^{th} compartment are not associated with the disappearance of excitation, but rather are caused by other phenomena, such as solvation, vibrational relaxation or internal conversion dynamics within/between the excited state(s). After the redistributions, we see that induced absorption and GSB of the last compartment fully decays with a time constant of 1 ns. Given such a relatively long timescale, we can infer an assumption that this decay is nonradiative, because the emission of this sample could not be detected.

pNphe was excited with a fs laser pulses of 415-nm wavelength and 280 cm^{-1} bandwidth (curve *f* in Figure 4.4). Pulse energy and the IRF of the experiment were 175 nJ and 130 fs respectively. Collected pump-probe data are presented in Figure 4.7 A and B. An initial transient absorption spectrum (26 fs delay in Figure 4.7 B), shows a bleaching signal heavily affected by coherent artifacts [127]. Specifically, a cross-phase modulation can be observed as a narrow spike around the pump wavelength, and stimulated Raman scattering band (see above), is observed as a negative peak around 470 nm. After the disappearance of coherent phenomena, GSB can be observed clearly centered around 415 nm, and an induced absorption stretching all over the 450-750 nm region. Within ca. 1 ps, this wide induced absorption structure transforms to a relatively narrow band with a peak absorbance around 460 nm and as time passes it gradually decrease

and shift to the blue. As it is evident from the kinetic traces, transient absorption signal of pNphe comprised of GSB and induced absorption fully disappears within 40 ps after the excitation.

In the SADS of pNphe (Figure 4.7 C), we see that GSB band has similar amplitudes only in the first two compartments, thus spectral rearrangement within the excited state takes only ≤ 400 fs. Afterwards GSB signal continuously decreases while induced absorption shifts to the blue. This fast decrease in GSB could be caused by the presence of conical intersection between reaction surfaces of excited and ground states, whilst the thermalization of “hot” ground state would be consistent with blue shift of induced absorption. Time constant associated with the last SADS of pNphe is 12 ps; comparing it to the corresponding number from pNph fit, we see that proton removal from 4-nitrophenol increases the excitation relaxation rate by two orders of magnitude. Thus, in the further interpretations 4-nitrophenolate chromophore could be considered as excitation quencher.

4.3.4. Pump-probe and flash photolysis on IB1a

Excitation in the pump-probe experiments on photochromic switch IB1a was performed using a 303-nm wavelength (180 cm^{-1} bandwidth, curve *i* in Figure 4.4) and 450 nJ energy femtosecond pulses. IRF for this configuration was ca. 200 fs. Selected kinetic traces and time-gated spectra from pump-probe and flash photolysis experiments on IB1a are presented in Figure 4.8 and Figure 4.9, respectively. The first time-gated spectrum (32 fs delay in Figure 4.8 B) measured in IB1a shows two absorption bands and GSB signal appearing instantaneously after the excitation. Subsequently, within 500 fs (see 480 fs spectrum in Figure 4.8 B) the signal of GSB increases, while induced absorption bands increase and converge closer to each other. The kinetic traces depict this convergence, or gap disappearance between two absorption

bands, by slightly slower ingrowth of the transient absorption around 430 nm (trace of open up-triangles, Figure 4.8 A), compared to that at 500 nm (down triangles). Another non-IRF limited change in the kinetics is the increase of GSB signal. This gradual growth is an indication that GSB initially overlaps with an induced absorption band which disappears within ca. 8 ps after the excitation. Dynamic changes occurring on 5-10 ps timescale are present over the entire investigated spectral region, they result in qualitative changes of the shape of transient absorbance spectrum. A time-gated spectrum at 13 ps displays a broad absorption plateau in 350-800 nm region, with two distinct bands on top of it. These bands are centered at 395 and 435 nm. Within subsequent 3 ns, these bands shift respectively by 26 and 5 nm to the blue, whist the overall amplitude of absorption plateau decreases by about 40 %. Further dynamics, which was observed by the means of flash photolysis, is not as rich as in the ultrafast time domain (Figure 4.9). Here an even more pronounced 430-nm band is initially observed, placed over the broad induced absorption plateau. This band completely vanishes within 24 ns after the excitation. From this point on, no other spectral features, except the absorption plateau, can be distinguished. The logarithmic part of 425-nm kinetic trace (Figure 4.9 A, crossed-square) illustrates the decay of absorption plateau, which almost completely disappears in ca. 1 μs.

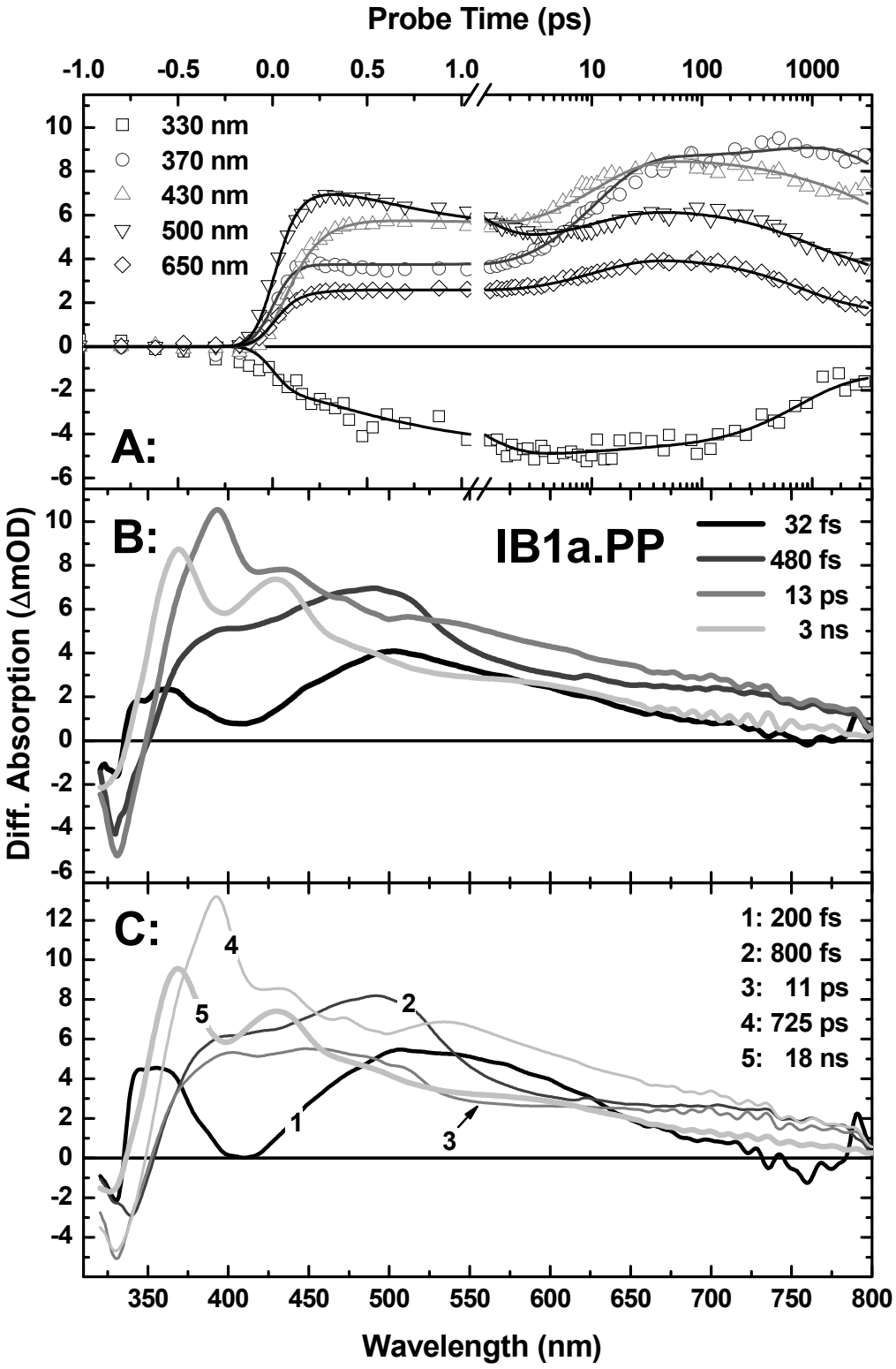

Figure 4.8 Results from pump-probe experiment on IB1a photochromic switch (IB1a.PP). Transient absorption kinetics for characteristic wavelengths (A:), time-gated spectra for selected delay times (B:) and fitting results in the form of SADS (C:). Probe wavelengths, gate times and SADS associated time constants are shown in the respective legends. Sequential dynamics model with five compartments was assumed while fitting; solid lines in the kinetic datasets (A:) depict fit curves for corresponding probe wavelengths.

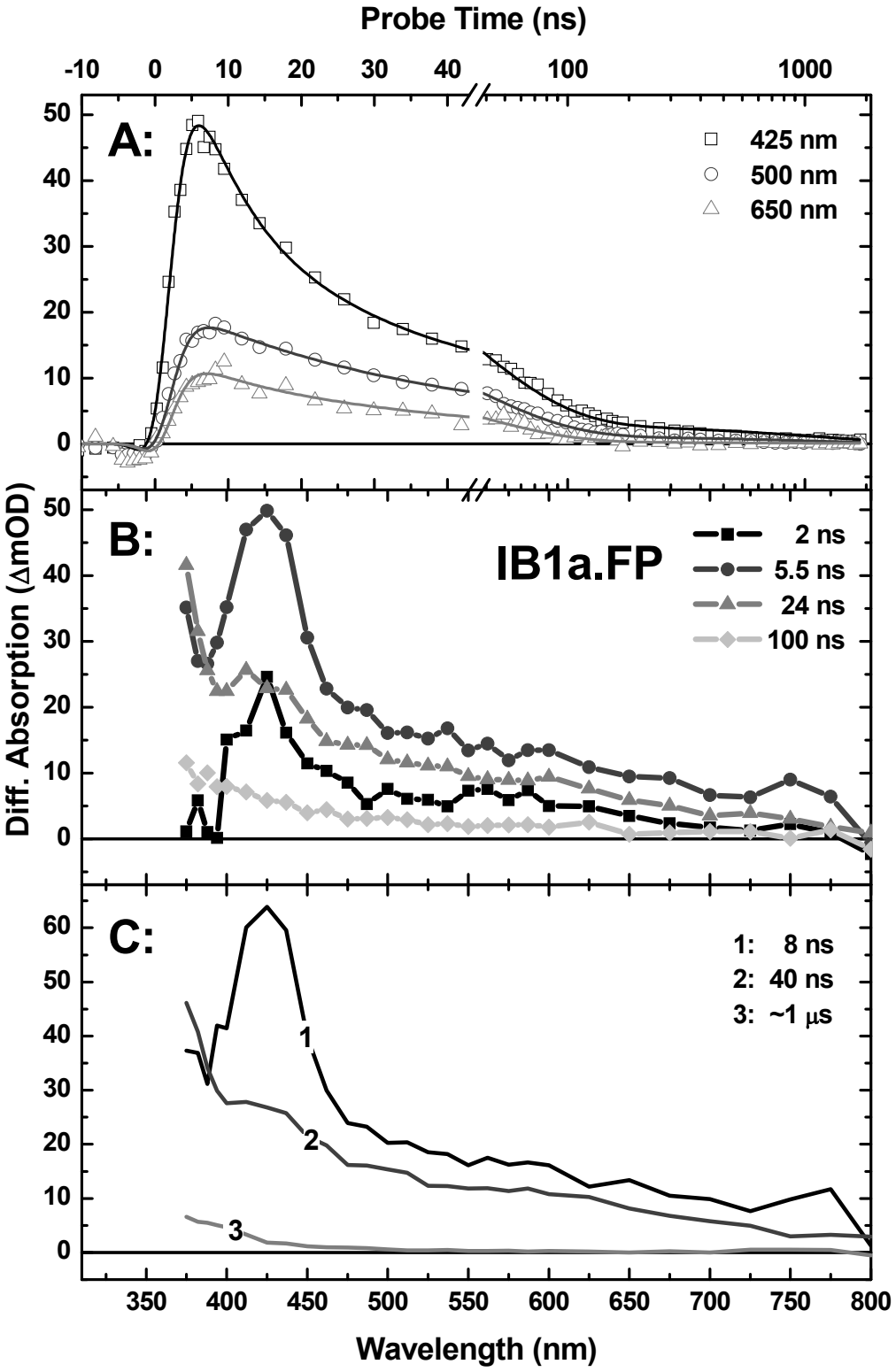

Figure 4.9 Results from flash photolysis experiment on IB1a photochromic switch (IB1a.FP). Transient absorption kinetics for characteristic wavelengths (A:), time-gated spectra for selected delay times (B:) and fitting results in the form of SADS (C:). Probe wavelengths, gate times and SADS associated time constants are shown in the respective legends. Sequential dynamics model with three compartments was assumed while fitting; solid lines in the kinetic datasets (A:) depict fit curves for corresponding probe wavelengths.

Our interpretation of ultrafast dynamics in IB1 derives form the comparison of fitted photochrom SADS with the ones of its model compounds. For the viewing convenience fits of the ultra-fast domain are re-pictured in Figure 4.10. The first eye-catching thing, while comparing these SADS, is the similarity between the first compartment spectra of IndI and IB1a.PP. Note that in the comparison of these spectra, one should keep in mind the GSB band presence in IB1a, which affects its spectral components below 375 nm; this causes a slight suppression of induced UV absorption band in the first compartment. The spectral resemblance implies that excited 3*H*-indolium cation in IB1 is formed within the IRF of our experiment. This implication is additionally supported by the fact that GSB band in IB1a.PP reaches is maximum at ca. 8 ps after the excitation (open squares in Figure 4.8 A), which closely resembles the overall lifetime of the UV absorption band in IndI (open squares in Figure 4.5 A). None of the other model compounds investigated shows any substantial induced absorption in 320-340 nm range. Unfortunately we have not been able to perform a pump-probe experiment on a compound which would resemble indoline moiety in IB1a (closed ring configuration); but this moiety has a smaller conjugated system, extending only to the benzene ring, thus one would expect that steady-state absorption and, correspondingly, ESA spectra would be blue-shifted with respect to those of IndI. Of course, it is conceivable that above mentioned GSB band suppression can arise from ESA of IB1 molecule as a whole, but it is very unlikely that it would produce analogous transient absorption spectra with a similar decay time as in IndI.

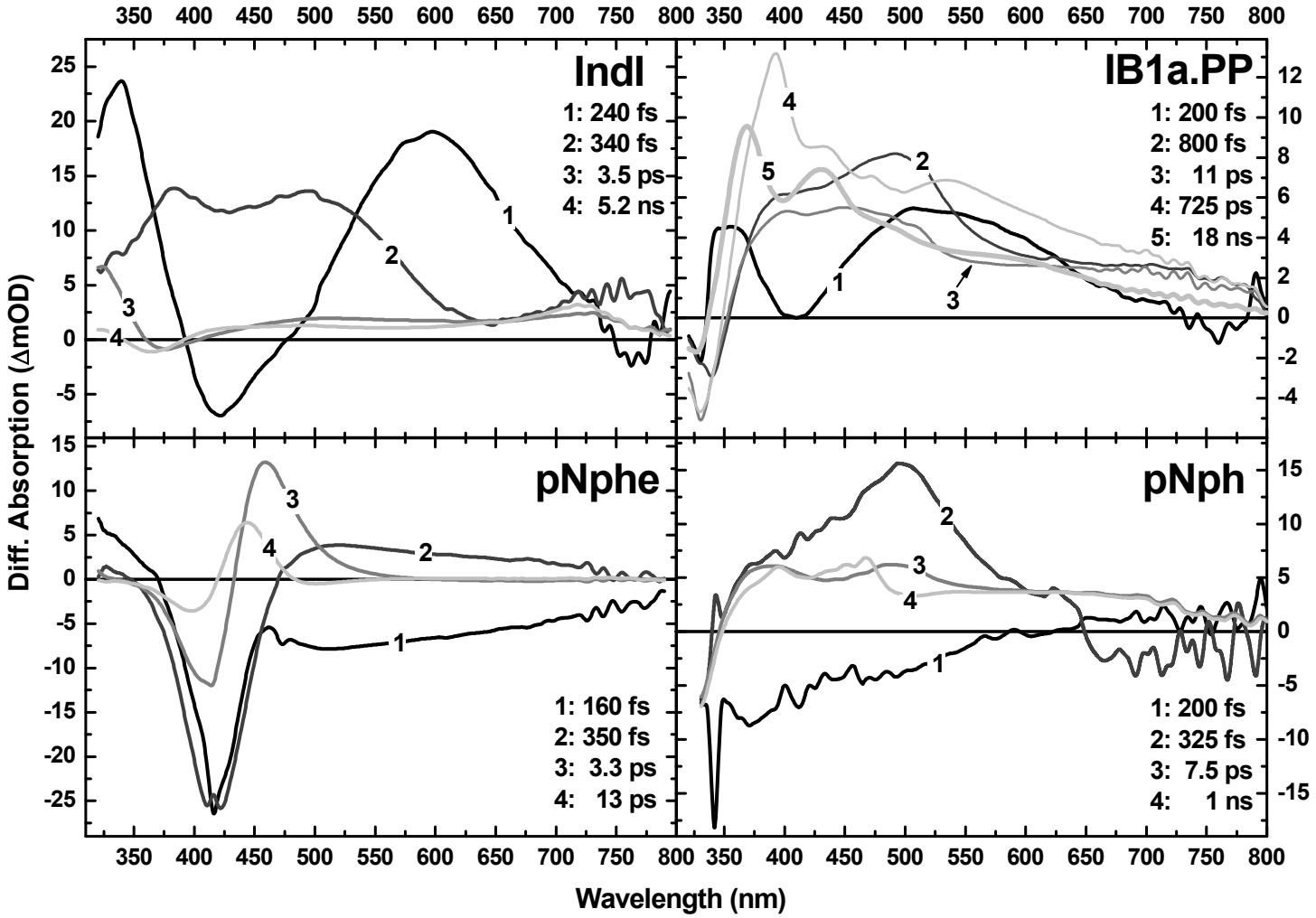

Figure 4.10 Comparison of the estimated SADS, coming from the global analysis fit on collected pump-probe data for: Indolium iodide (IndI), photochrom IB1a (IB1a.PP), 4-nitrophenoleate (pNphe) and 4-nitrophenol (pNph). Sequential dynamics model with four compartments was assumed in all fits, with an exception of the IB1a.PP that was fitted using the five-compartment model. Time constants associated with corresponding SADS are depicted in the legends.

The SADS of IB1a.PP indicate that initial induced absorption, with a double band structure in first compartment, transforms to a broad induced absorbance with pronounced band around 500 nm (IB1a.PP 2, in Figure 4.10). Although excited IndI also produces IA around 500-nm within ≥ 200 fs after the excitation, comparison of relative amplitudes in the first and second compartments suggests that apart form further dynamics of excited 3*H*-indolium cation we also see an input from excited nitrophenol ring. Another spectral feature of IB1, which demonstrates dynamics similar to pNph, is a featureless absorption plateau in the red edge of the spectrum above 650 nm. Here constant absorption is observed on subpicosecond and picosecond time scales (compare 2nd and 3rd IB1a.PP compartments with 3rd and 4th ones of pNph). Observation of pNph-like dynamics, at least in the initial steps of IB1a photoexcitation, is consistent with the point that excitation band in steady-state absorption of IB1a is dominated by absorbance from nitrophenol moiety (see description in the results section and [159]).

So far, while discussing the excitation dynamics within the first three compartments of IB1a, we did not encounter any induced absorption peaking around 425 nm. A distinct absorption band around this wavelength would be a sign of nitrophenolate anion formation in IB1b. And indeed, only in the fourth SADS, which is formed at 12 ps after the excitation, we see a minute absorption increase around 425 nm, which in the subsequent compartment transforms to a more pronounced band. This apparently means that nitrophenolate anion in our photochrome forms 12 ps past the excitation, which is in slight contrast to our abovementioned assumption of IRF limited formation of 3*H*-indolium cation. It may be possible that ring opening in IB1 and formation of two separate ions of zwitterion IB1b do not occur simultaneously. In principle, after the bond cleavage 3*H*-indolium cation should be formed within the time necessary for the formation of N=C bond, a process involving only electronic reconfiguration. In contrast, to

produce a stable nitrophenolate anion, IB1 photochrome needs to undergo not only the redistribution of electrons but also experience a minor conformational change: the distance between C–O atom changes from 1.47 Å in IB1a to 3.07 Å in IB1b (supporting information of [159]). Thus possibly the formations of cation and anion species are associated with different time constants.

Finally, the last spectrotemporal dynamic step of IB1a.PP is the emergence of absorption band around 393 nm (4^{th} SADS) and its subsequent shift to 369 nm within 725 ps (5^{th} SADS). Formation of this band is correlated with the appearance of nitrophenolate chromophore and it cannot be ascribed to any of the model compounds investigated. The fact that its appearance is synchronized with the formation of anion in IB1b, could mean that it originates from some kind of coherent interaction between anionic part of IB1b and the rest of the molecule. Precondition for this interaction can be found in Figure 4.4, where there is an apparent overlap between bands of IndI fluorescence (*c*) and pNphe absorption (*e*). Thus the excitation can couple or channel from 3*H*-indolium cation to nitrophenolate anion, were it would be efficiently quenched.

Tomasulo *el al.* [159] have recently performed a flash photolysis experiments on photochrome IB1 and interpreted their results by a simple model: UV induced C–O bond cleavage produces a 4-nitrophenolate chromophore which causes an absorption increase in the visible region; subsequently cleaved bond thermally re-forms back and induced absorption vanishes with the time constant of ca. 22 ns. Results of our flash photolysis measurements on IB1a, in the form of SADS, are presented in Figure 4.9 C. It is obvious, that apart from 4-nitrophenolate anion absorption, there is a longer-lived absorption plateau with an increasing absorbance in the blue part of the spectrum (2^{nd} and 3^{rd} compartment in Figure 4.9 C). An absorption band assigned to 4-nitrophenolate is observed only in the first fit compartment, which

decays with the lifetime of 8 ns. The following decay of absorption plateau takes about 40 ns with an exception of UV region where it lingers longer than 1 μs. The lifetime values of the same compound reported by Tomasulo *et al.*, probably partially incorporates the decay of absorption plateau which was not clearly resolved in their experiment because of lower signal-to-noise ratio.

From the presented data, it is difficult to find a feasible explanation for this featureless induced absorption plateau. It could be caused by some interaction between anionic and cationic moieties of IB1b, although it is strange why it persists by two orders of magnitude longer then 4-nitrophenolate chromophore. On the other hand, this induced absorption could come from a dimer valence anion of MeCN [162, 168] which forms within subpicosecond time scale after the release of electron to solution. However, its spectral shape does not resemble that of the MeCN dimer anion, and the lifetime of the anion has been reported to be in the millisecond time domain. Jet another possibility for the “long” time component, would be the unequilibrated ground state or possible formation of triplet states. Additional experimental work and modeling is necessary to enable better interpretation of this absorption feature. One of the few possibilities would be a search for possible traces of solvated electron in MeCN which has its absorption maxima around 1.4 μm. [162, 170]

Summing up the results, we propose the following model to synthesize the observations on the ultrafast dynamics in IB1a. UV excitation instantaneously cleaves the C–O bond and the excited 3*H*-indolium cation is formed within ≤ 200 fs. Subsequently, the molecule undergoes a minor conformational change and 4-nitrophenolate anion is fully formed in 12 ps. The following interaction of the two moieties of zwitterion results in the quenching of excitation by the nitrophenolate anion. These dynamic steps probably do not occur with 100% yields, and shortcuts back to the ground state may be present. One obvious

shortcut would be the situation where the conformational change, required for the visible absorbance band to form, fails to occur and the response of 4-nitrophenol moiety instead of 4-nitrophenolate is observed.

In summary, we have used a femtosecond pump-probe and nanosecond flash photolysis techniques to disentangle the excited state dynamics of the indolo[2,1-*b*][1,3]benzoxazine photochromic switch. The observed forward-switching dynamics could be partly rationalized by the dynamics of the model compounds, representing different moieties of the photochromic molecule. A scheme of excited state dynamics resulting in photochromism was proposed, that allowed qualitative interpretation of experimental observations. The understanding of the influence of different chromophoric groups in the switching behavior of this class of photochromes opens the way of intelligent design of the switches with desired spectral and dynamical properties.

Conclusions

Based on the results presented in this thesis, the following can be concluded:

1. Two-photon absorption in R-KDP, measured at 355 nm wavelength, is crystal orientation dependant, and the TPA coefficient value for tripler cut crystals is ~ 3 times larger for the e-polarization than for the o-polarization.
2. VIS absorbing defects in R-KDP crystals are formed by the two-photon absorption of the 3rd harmonic of Nd doped lasers and fully decay within ca. 6 s. The parameters necessary to estimate induced defect absorption were also determined.
3. UV-laser induced conditioning effect increases the overall lifetime of transient defect-states and can have an adverse influence on defect accumulation in systems that use R-KDP crystals.
4. Operation of a versatile three-pulse transient absorption spectrometer was demonstrated, yielding the possibility for direct observation of ground state dynamics in fluorescent membrane marker Laurdan.
5. Removal of a proton from 4-nitorphenol in the solution of acetonitrile, causes a decrease of excited state lifetime by ca. 2 orders of magnitude and thus making it an efficient excitation quenching moiety in molecular complexes.
6. A Mode explaining the ultrafast excited state dynamics and ring cleavage that results the photochromism was propose for newly synthesized indolo[2,1-*b*][1,3]benzoxazine compound.

References

[1]. A. L. Cavalieri, N. Muller, T. Uphues, V. S. Yakovlev, A. Baltuska, B. Horvath, B. Schmidt, L. Blumel, R. Holzwarth, S. Hendel, M. Drescher, U. Kleineberg, P. M. Echenique, R. Kienberger, F. Krausz and U. Heinzmann, Attosecond spectroscopy in condensed matter, Nature **449** (7165), 1029-1032 (2007).

[2]. G. Hinshaw, J. L. Weiland, R. S. Hill, N. Odegard, D. Larson, C. L. Bennett, J. Dunkley, B. Gold, M. R. Greason, N. Jarosik, E. Komatsu, M. R. Nolta, L. Page, D. N. Spergel, E. Wollack, M. Halpern, A. Kogut, M. Limon, S. S. Meyer, G. S. Tucker and E. L. Wright, Five-Year Wilkinson Microwave Anisotropy Probe (WMAP) Observations: Data Processing, Sky Maps, & Basic Results, Submitted to the Astrophysical Journal Supplement Series, (2008).

[3]. R. G. W. Norrish and G. Porter, Chemical Reactions Produced by Very High Light Intensities, Nature **164**, 658 (1949).

[4]. T. H. Maiman, Stimulated Optical Radiation in Ruby, Nature **187** (4736), 493-494 (1960).

[5]. L. E. Hargrove, R. L. Fork and M. A. Pollack, Locking of He–Ne laser modes induced by synchronous intracavity modulation, Applied Physics Letters **5**, 4 (1964).

[6]. S. A. Akhmanov, A. I. Kovrigin, A. S. Piskarskas, V. V. Fadeev and R. V. Khokhlov, Observation of parametric amplification in the optical range, JETP Letters **2**, 191-193 (1965).

[7]. K. P. Burneika, M. V. Ignatavichus, V. I. Kabelka, A. S. Piskarskas and A. Y. Stabinis, Parametric generation of ultrashort pulses of tunable-frequency radiation, JETP Letters, (1972).

[8]. J. R. Novak and M. W. Windsor, Laser Photolysis and Spectroscopy in the Nanosecond Time Range: Excited Singlet State Absorption in Coronene, Journal of Chemical Physics **47** (8), 3075 (1967).

[9]. F. Rondelez, H. Hervet and W. Urbach, A sensitive optical grating method for flash photolysis: application to the CIS-trans photochemical isomerization of azo dyes, Chemical Physics Letters **53** (1), 138-143 (1978).

[10]. J. Zhang and C. H. Wang, Simultaneous measurements of the diffusion coefficients of the dye molecule and its photoproduct by the holographic relaxation technique, Journal of Physical Chemistry **90** (11), 2296-2297 (1986).

[11]. A. J. DeMaria, D. A. Stetser and H. Heynau, Self Mode-Locking of Lasers with Saturable Absorbers, Applied Physics Letters **8** (7), 174-176 (1966).

[12]. A. Baltuska, Z. Wei, M. S. Pshenichnikov, D. A. Wiersma and R. Szipocs, All-solid-state cavity-dumped sub-5-fs laser, Applied Physics B-Lasers and Optics **65** (2), 175-188 (1997).
[13]. R. Jimenez and G. R. Fleming, Ultrafast Spectroscopy of Photosynthetic Systems in: *Biophysical Techniques in Photosynthesis*, Vol. ed. J. Amesz and A. J. Hoff (Kluwer Academic Publishers, Dordrecht, 1996) pp. 63-73.
[14]. F. Gai, J. C. McDonald and P. Anfinrud, Pump-Dump-Probe Spectroscopy of Bacteriorhodopsin: Evidence for a Near-IR Excited State Absorbance, Journal of American Chemical Society **119**, 6201-6202 (1997).
[15]. S. Ruhman, B. Hou, N. Freidman, M. Ottolenghi and M. Sheves, Following Evolution of Bacteriorhodopsin in its Reactive Excited State via Stimulated Emission Pumping, Journal of American Chemical Society **124** (30), 8854-8858 (2002).
[16]. P. Changenet-Barret, C. Choma, E. Gooding, W. DeGrado and R. M. Hochstrasser, Ultrafast Dielectric Response of Proteins from Dynamics Stokes Shifting of Coumarin in Calmodulin, J. Physical Chemistry B **104**, 9322-9329 (2000).
[17]. S. A. Kovalenko, J. Ruthmann and N. P. Ernsting, Femtosecond hole-burning spectrocopt with Stimulated Emission pumping and supercontinuum probing, Journal of Chemical Physics **109** (5), 1894-1900 (1998).
[18]. S. L. Logunov, V. V. Volkov, M. Braun and M. A. El-Sayed, The Relaxation dynamics of the excited electronic states of retinal in bacteriorhodopsin by two-pump probe femtosecond studies, Proc Natl Acad Sci U S A **98** (15), 8475-8479 (2001).
[19]. D. S. Larsen, I. H. M. van Stokkum, M. Vengris, M. A. van der Horst, F. L. de Weerd, K. J. Hellingwerf and R. van Grondelle, Incoherent manipulation of the photoactive yellow protein photocycle with dispersed pump-dump-probe spectroscopy, Biophysical Journal **87** (3), 1858-1872 (2004).
[20]. D. S. Larsen, E. Papagiannakis, I. H. M. van Stokkum, M. Vengris, J. T. M. Kennis and R. van Grondelle, Excited state dynamics of beta-carotene explored with dispersed multi-pulse transient absorption, Chemical Physics Letters **381** (5-6), 733-742 (2003).
[21]. S. A. Rice and M. Zhao, *Optical Control of Molecular Dynamics*, (Wiley Interscience, New York, 2000).
[22]. L. N. Rashkovich, *KDP family single crystals*, (Adam Hilger, Bristol, 1991).
[23]. J. A. Paisner, J. D. Boyes, S. A. Kumpan, W. H. Lowdermilk and M. Sorem, Conceptual design of the National Ignition Facility, SPIE **2633**, 2-12 (1995).
[24]. C. E. Barker, B. M. Van Wonterghem, J. M. Auerbach, R. J. Foley, J. R. Murray, J. H. Campbell, J. A. Caird, D. R. Speck and

B. W. Woods, Design and performance of the Beamlet laser third-harmonic frequency converter, SPIE **2633**, 398-404 (1995).
[25]. T. Sasaki and A. Yokotani, Growth of Large KDP Crystals for Laser Fusion Experiments, Journal of Crystal Growth **99** (1-4), 820-826 (1990).
[26]. M. A. Rhodes, C. D. Boley, A. G. Tarditi and B. S. Bauer, Plasma electrode pockels cell for ICF lasers, SPIE **2633**, 94-104 (1995).
[27]. J. A. Paisner, W. H. Lowdermilk, J. D. Boyes, M. S. Sorem and J. M. Soures, Status of the National Ignition Facility Project, Fusion Engineering and Design **44** (1), 23-33 (1999).
[28]. M. L. Andre, The French Megajoule Laser Project (LMJ), Fusion Engineering and Design **44** (1), 43-49 (1999).
[29]. I. V. Galakhov, S. G. Garanin, V. A. Eroshenko, G. A. Kirillov, G. G. Kochemasov, V. M. Murugov, N. N. Rukavishnikov and S. A. Sukharev, Concept of the Iskra-6 Nd-laser facility, Fusion Engineering and Design **44** (1), 51-56 (1999).
[30]. N. P. Zaitseva, I. L. Smolskii and L. N. Rashkovich, Investigation of KDP Crystals Grown When Applying Temperature Lowering Technique for Speedy Growing, Kristallografiya **36** (1), 198-202 (1991).
[31]. K. Fujioka, S. Matsuo, T. Kanabe, M. Nakatsuka and S. Nakai, Basic technology of fast growing for normal and partially deuterated KDP crystals, SPIE **2633**, 292-298 (1995).
[32]. N. P. Zaitseva, J. J. DeYoreo, M. R. Dehaven, R. L. Vital, K. E. Montgomery, M. Richardson and L. J. Atherton, Rapid growth of large-scale (40-55 cm) KH2PO4 crystals, Journal of Crystal Growth **180** (2), 255-262 (1997).
[33]. D. L. Xu and D. F. Xue, Fast growth of KDP, Journal of Crystal Growth **310** (7-9), 2157-2161 (2008).
[34]. A. Yokotani, Y. Nishida, K. Fujioka, T. Sasaki, T. Yamanaka and C. Yamanaka, A chromogenic limulus test for detection of microbes that decreases the laser damage threshold of potassium dihydrogen phosphate crystals, Journal of Applied Physics **61** (9), 4696-4698 (1987).
[35]. K. E. Montgomery and F. P. Milanovich, High-Laser-Damage-Threshold Potassium Dihydrogen Phosphate Crystals, Journal of Applied Physics **68** (8), 3979-3982 (1990).
[36]. S. G. Demos, M. Staggs and H. B. Radousky, Bulk defect formations in KH2PO4 crystals investigated using fluorescence microscopy, Phys. Rev. B **67** (22), 224102 (2003).
[37]. R. A. Negres, N. P. Zaitseva, P. DeMange and S. G. Demos, An expedited approach to evaluate the importance of different crystal growth parameters on laser damage performance in KDP and DKDP, SPIE **6403**, 64031S (2006).
[38]. S. G. Demos, M. Staggs, H. C. Yan, H. B. Radousky and J. J. DeYoreo, Microscopic fluorescence imaging of bulk defect

clusters in KH2PO4 crystals, Optics Letters **24** (4), 268-270 (1999).
[39]. M. Pommiès, D. Damiani, B. Bertussi, J. Capoulade, H. Piombini, J. Y. Natoli and H. Mathis, Detection and characterization of absorption heterogeneities in KH2PO4 crystals, Optics Communications **267**, 154-161 (2006).
[40]. J. E. Davis, R. S. Hughes and H. W. H. Lee, Investigation of Optically Generated Transient Electronic Defects and Protonic Transport in Hydrogen-Bonded Molecular-Solids - Isomorphs of Potassium Dihydrogen Phosphate, Chemical Physics Letters **207** (4-6), 540-545 (1993).
[41]. M. M. Chirila, N. Y. Garces, L. E. Halliburton, S. G. Demos, T. A. Land and H. B. Radousky, Production and thermal decay of radiation-induced point defects in KD2PO4 crystals, Journal of Applied Physics **94** (10), 6456-6462 (2003).
[42]. C. D. Marshall, S. A. Payne, M. A. Henesian, J. A. Speth and H. T. Powell, Ultraviolet-Induced Transient Absorption in Potassium Dihydrogen Phosphate and Its Influence on Frequency-Conversion, Journal of the Optical Society of America B (Optical Physics) **11** (5), 774-785 (1994).
[43]. P. DeMange, R. A. Negres, C. W. Carr, H. B. Radousky and S. G. Demos, Laser-induced defect reactions governing damage initiation in DKDP crystals, Optics Express **14** (12), 5313-5328 (2006).
[44]. C. Cavailler, N. Fleurot, T. Lonjaret and J. M. Di-Nicola, Prospects and progress at LIL and Megajoule, Plasma Physics and Controlled Fusion **46**, B135-B141 (2004).
[45]. D. N. Nikogosyan, *Nonlinear Optical Crystals: A Complete Survey*, (Springer, New York, 2005).
[46]. J. C. Slater, Theory of the Transition in KH_2PO_4, Journal of Chemical Physics **9**, 16-33 (1941).
[47]. C. C. Stephenson and J. G. Hooley, Heat Capacity of Potassium Dihydrogen Phosphate at the Curie Point, Physical Review **56** (1), 121 (1939).
[48]. H. Yoshida, T. Jitsuno, H. Fujita, M. Nakatsuka, M. Yoshimura, T. Sasaki and K. Yoshida, Investigation of bulk laser damage in KDP crystal as a function of laser irradiation direction, polarization, and wavelength, Applied Physics B-Lasers and Optics **70** (2), 195-201 (2000).
[49]. D. Megaw, *Crystal structures - a working approach*, (Saunders, London, 1973).
[50]. G. M. Loiacono, J. J. Zola and G. Kostecky, The taper effect in KH_2PO_4 type crystals, Journal of Crystal Growth **58** (3), 495-499 (1982).
[51]. I. Owczare and K. Sangwal, Effect of impurities on the growth of KDP crystals: On the mechanism of adsorption on {100} faces

from tapering data, Journal of Crystal Growth **99** (1-4), 827-831 (1990).
[52]. S. A. de Vries, P. Goedtkindt, S. L. Bennett, W. J. Huisman, M. J. Zwanenburg, D. M. Smilgies, J. J. De Yoreo, W. J. P. van Enckevort, P. Bennema and E. Vlieg, Surface Atomic Structure of KDP Crystals in Aqueous Solution: An Explanation of the Growth Shape, Physical Review Letters **80** (10), 2229-2232 (1998).
[53]. W. E. Hughes and W. G. Moulton, Electron Spin Resonance of Irradiated KH2PO4 and KD2PO4, J. Chem. Phys. **39** (5), 1359-13560 (1963).
[54]. R. C. DuVarney and R. P. Kohin, Domain Switching in Irradiated Ferroelectric KH2PO4 Observed by Electron Spin Resonance, Phys. Rev. Lett. **20** (6), 259 - 262 (1968).
[55]. K. Tsuchida, R. Abe and M. Naito, Electron Spin Resonance of γ-Irradiated KH_2PO_4, Journal of the Physical Society of Japan **35** (3), 806-809 (1973).
[56]. J. A. McMillan and J. M. Clemens, Paramagnitic and optical studies of radiation damage centers in $K(H_{1-X}D_X)_2PO_4$, Journal of Chemical Physics **68** (8), 3627-3631 (1978).
[57]. K. T. Stevens, N. Y. Garces, L. E. Halliburton, M. Yan, N. P. Zaitseva, J. J. DeYoreo, G. C. Catella and J. R. Luken, Identification of the intrinsic self-trapped hole center in KD2PO4, Applied Physics Letters **75** (11), 1503-1505 (1999).
[58]. E. Diéguez and J. M. Cabrera, Optical absorption and thermoluminescence of x-irradiated KDP, J. Phys. D: Appl. Phys. **14**, 91-97 (1981).
[59]. E. Diéguez, J. M. Cabrera and Agulló-López, Optical absorption and luminescence induced by x rays in KDP, DKDP, and ADP, Journal of Chemical Physics **81** (8), 3369-3374 (1984).
[60]. J. W. Wells, E. Budzinski and H. C. Box, ESR and ENDOR studies of irradiated potassium dihydrogen phosphate, J. Chem. Phys. **85** (11), 6340-6346 (1986).
[61]. S. D. Setzler, K. T. Stevens, L. E. Halliburton, M. Yan, N. P. Zaitseva and J. J. DeYoreo, Hydrogen atoms in KH2PO4 crystals, Physical Review B **57** (5), 2643-2646 (1998).
[62]. N. Y. Garces, K. T. Stevens, L. E. Halliburton, S. G. Demos, H. B. Radousky and N. P. Zaitseva, Identification of electron and hole traps in KH2PO4 crystals, Journal of Applied Physics **89** (1), 47-52 (2001).
[63]. C. S. Liu, C. J. Hou, N. Kioussis, S. G. Demos and H. B. Radousky, Electronic structure calculations of an oxygen vacancy in KH_2PO_4, Physical Review B **72** (13), 134110 (2005).
[64]. N. Y. Garces, K. T. Stevens, L. E. Halliburton, M. Yan, N. P. Zaitseva and J. J. DeYoreo, Optical absorption and electron paramagnetic resonance of Fe ions in KDP crystals, Journal of Crystal Growth **225** (2-4), 435-439 (2001).

[65]. E. Dieguez, A. Cintas, P. Hernandez and J. M. Cabrera, Ultraviolet absorption and growth bands in KDP, Journal of Crystal Growth **73** (1), 193-195 (1985).
[66]. V. I. Bredikhin, N. V. Kiseleva and V. V. Korolikhin, Inorganic Materials **22**, 94 (1986). Translated from: V. I. Bredikhin, N. V. Kiseleva and V. V. Korolikhin, Sov. Nonorganic Mater. **22**, 112 (1986),
[67]. N. Zaitseva, L. Carman, I. Smolsky, R. Torres and M. Yan, The effect of impurities and supersaturation on the rapid growth of KDP crystals, Journal of Crystal Growth **204** (3), 512-524 (1999).
[68]. N. Zaitseva and L. Carman, Rapid growth of KDP-type crystals, Progress in Crystal Growth and Characterization of Materials **43** (1), 1-118 (2001).
[69]. M. Yan, R. A. Torres, M. J. Runkel, B. W. Woods, I. D. Hutcheon, N. Zaitseva and J. J. De Yoreo, Investigation of impurities and laser-induced damage in the growth sectors of rapidly grown KDP crystals, SPIE **2966**, 11-16 (1997).
[70]. K. Fujioka, S. Matsuo, T. Kanabe, H. Fujita and M. Nakatsuka, Optical properties of rapidly grown KDP crystal improved by thermal conditioning, Journal of Crystal Growth **181** (3), 265-271 (1997).
[71]. S. G. Demos, M. Staggs, J. J. De Yoreo and H. B. Radousky, Imaging of laser-induced reactions of individual defect nanoclusters, Optics Letters **26** (24), 1975-1977 (2001).
[72]. I. N. Ogorodnikov, V. Y. Yakovlev, B. V. Shul'gin and M. K. Satybaldieva, Transient Optical Absorption of Hole Polarons in ADP ($NH_4H_2PO_4$) and KDP (KH_2PO_4) Crystals, Physics of the Solid State **44** (5), 880-887 (2002).
[73]. O. Martínez Matos, G. A. Torchia, G. M. Bilmes and J. O. Tocho, Photoacoustic characterization of transient defects in potassium dihydrogen phosphate crystals, Physical Review B **69** (22), 224102 (2004).
[74]. P. Liu, W. L. Smith, H. Lotem, J. H. Bechtel and N. Bloembergen, Absolute two-photon absorption coefficients at 355 and 266 nm, Physical Review B **17** (12), 4620-4632 (1978).
[75]. R. L. Sutherland, *Handbook of Nonlinear Optics*, (Marcel Dekker, New York, 1996).
[76]. T. R. Waite, Diffusion-Limited Annealing of Radiation Damage in Germanium, Physical Review A (General Physics) **107** (2), 471-478 (1957).
[77]. M. Barkauskas, A. Melninkaitis, M. Sinkevicius, A. Ciburys, R. Gadonas, V. Sirutkaitis, H. Bercegol and L. Lamaignere, Linear and nonlinear absorption and defects formation in KDP crystals used for large aperture doublers and triplers, SPIE **5949**, 360-368 (2005).

[78]. M. Divall, K. Osvay, G. Kurdi, E. J. Divall, J. Klebniczki, J. Bohus, Á. Péter and K. Polgár, Two-photon-absorption of frequency converter crystals at 248 nm, Applied Physics B **81**, 1123-1126 (2005).
[79]. A. Dubietis, G. Tamošauskas, A. Varanavičius and G. Valiulis, Two-photon absorbing properties of ultraviolet phase-matchable crystals at 264 and 211 nm, Applied Optics **39** (15), 2437-2440 (2000).
[80]. W. L. Smith, KDP and ADP transmission in the vacuum ultraviolet, Applied Optics **16** (7), 1798 (1977).
[81]. M. Barkauskas, A. Melninkaitis, D. Mikšys, L. Meslinaitė, R. Grigonis, V. Sirutkaitis, H. Bercegol and L. Lamaignere, Characterization of KDP crystals used in large aperture doublers and triplers, SPIE **6403**, 64031V (2006).
[82]. G. Porter, Flash photolysis and spectroscopy – A new method for the study of free radical reactions, Proc. R. Soc. London, Ser. A **200**, 284-300 (1950).
[83]. F. Gai, K. C. Hasson, J. C. McDonald and P. A. Anfinrud, Chemical dynamics in proteins: The photoisomerization of retinal in bacteriorhodopsin, Science **279** (5358), 1886-1891 (1998).
[84]. R. W. Schoenlein, L. A. Peteanu, R. A. Mathies and C. V. Shank, The 1st Step in Vision - Femtosecond Isomerization of Rhodopsin, Science **254** (5030), 412-415 (1991).
[85]. C. Burda, X. B. Chen, R. Narayanan and M. A. El-Sayed, Chemistry and properties of nanocrystals of different shapes, Chemical Reviews **105** (4), 1025-1102 (2005).
[86]. V. I. Klimov, D. W. McBranch, C. A. Leatherdale and M. G. Bawendi, Electron and hole relaxation pathways in semiconductor quantum dots, Physical Review B **60** (19), 13740-13749 (1999).
[87]. J. B. Asbury, R. J. Ellingson, H. N. Ghosh, S. Ferrere, A. J. Nozik and T. Q. Lian, Femtosecond IR study of excited-state relaxation and electron-injection dynamics of Ru(dcbpy)(2)(NCS)(2) in solution and on nanocrystalline TiO2 and Al2O3 thin films, Journal of Physical Chemistry B **103** (16), 3110-3119 (1999).
[88]. J. Z. Zhang, B. J. Schwartz, J. C. King and C. B. Harris, Ultrafast Studies of Photochromic Spiropyrans in Solution, Journal of the American Chemical Society **114** (27), 10921-10927 (1992).
[89]. R. J. Sension, S. T. Repinec, A. Z. Szarka and R. M. Hochstrasser, Femtosecond Laser Studies of the Cis-Stilbene Photoisomerization Reactions, Journal of Chemical Physics **98** (8), 6291-6315 (1993).
[90]. T. Nagele, R. Hoche, W. Zinth and J. Wachtveitl, Femtosecond photoisomerization of cis-azobenzene, Chemical Physics Letters **272** (5-6), 489-495 (1997).

[91]. I. K. Lednev, T. Q. Ye, R. E. Hester and J. N. Moore, Femtosecond time-resolved UV-visible absorption spectroscopy of trans-azobenzene in solution, Journal of Physical Chemistry **100** (32), 13338-13341 (1996).
[92]. R. van Grondelle, J. P. Dekker, T. Gillbro and V. Sundstrom, Energy transfer and trapping in photosynthesis, Biochimica et Biophysica Acta (BBA) - Bioenergetics **1187** (1), 1-65 (1994).
[93]. T. Arlt, S. Schmidt, W. Kaiser, C. Lauterwasser, M. Meyer, H. Scheer and W. Zinth, The Accessory Bacteriochlorophyll - a Real Electron Carrier in Primary Photosynthesis, Proceedings of the National Academy of Sciences of the United States of America **90** (24), 11757-11761 (1993).
[94]. C. Chudoba, E. Riedle, M. Pfeiffer and T. Elsaesser, Vibrational coherence in ultrafast excited state proton transfer, Chemical Physics Letters **263** (5), 622-628 (1996).
[95]. T. H. Joo, Y. W. Jia, J. Y. Yu, M. J. Lang and G. R. Fleming, Third-order nonlinear time domain probes of solvation dynamics, Journal of Chemical Physics **104** (16), 6089-6108 (1996).
[96]. S. A. Kovalenko, J. Ruthmann and N. P. Ernsting, Ultrafast Stokes shift and excited-state transient absorption of coumarin 153 in solution, Chemical Physics Letters **271** (1-3), 40-50 (1997).
[97]. S. A. Kovalenko, R. Schanz, H. Hennig and N. P. Ernsting, Cooling dynamics of an optically excited molecular probe in solution from femtosecond broadband transient absorption spectroscopy, Journal of Chemical Physics **115** (7), 3256-3273 (2001).
[98]. A. H. Zewail, Femtochemistry: Recent Progress in Studies of Dynamics and Control of Reactions and Their Transition States, Journal of Physical Chemistry **100** (31), 12701-12724 (1996).
[99]. H. van Amerongen, L. Valkunas and R. van Grondelle, *Photosynthetic Excitons*, (World Scientific, Singapore, 2000).
[100]. S. Mukamel, *Principles of nonlinear optical spectroscopy*, (Oxford University Press, New York, 1995).
[101]. S. Schenkl, F. van Mourik, G. van der Zwan, S. Haacke and M. Chergui, Probing the ultrafast charge translocation of photoexcited retinal in bacteriorhodopsin, Science **309** (5736), 917-920 (2005).
[102]. J. Herbst, K. Heyne and R. Diller, Femtosecond infrared spectroscopy of bacteriorhodopsin chromophore isomerization, Science **297** (5582), 822-825 (2002).
[103]. A. Assion, T. Baumert, M. Bergt, T. Brixner, B. Kiefer, V. Seyfried, M. Strehle and G. Gerber, Control of chemical reactions by feedback-optimized phase- shaped femtosecond laser pulses, Science **282** (5390), 919-922 (1998).

[104]. J. L. Herek, T. Polivka, T. Pullerits, G. J. S. Fowler, C. N. Hunter and V. Sundstrom, Ultrafast carotenoid band shifts probe structure and dynamics in photosynthetic antenna complexes, Biochemistry **37** (20), 7057-7061 (1998).
[105]. J. Savolainen, R. Fanciulli, N. Dijkhuizen, A. L. Moore, J. Hauer, T. Buckup, M. Motzkus and J. L. Herek, Controlling the efficiency of an artificial light-harvesting complex, Proc. Natl. Acad. Sci. USA **105** (22), 7641-7646 (2008).
[106]. J. Pique, Y. Engel, R. Levine, Y. Chen, R. Field and J. Kinsery, Broad Spectral Features in the Stimulated-Emission Pumping spectrum of Acetylene, Journal of Chemical Physics **88** (9), 5972-5974 (1988).
[107]. M. Vengris, D. S. Larsen, E. Papagiannakis, J. T. M. Kennis and R. van Grondelle, Multipulse transient absorption spectroscopy: a tool to explore biological systems in: *Analysis and Control of Ultrafast Photoinduced Reactions*, Vol. ed. O. Kühn and L. Wöste (Springer-Verlag, Berlin Heidelberg, 2007) pp. 750-774.
[108]. M. Vengris, I. H. M. van Stokkum, X. He, A. F. Bell, P. J. Tonge, R. van Grondelle and D. S. Larsen, Ultrafast excited and ground-state isomerization dynamics of the Green Fluorescent Protein chromophore in solution, Ultrafast Phenomena XIV 610-612 (2004).
[109]. M. Vengris, I. H. M. van Stokkum, X. He, A. F. Bell, P. J. Tonge, R. van Grondelle and D. S. Larsen, Ultrafast excited and ground-state dynamics of the green fluorescent protein chromophore in solution, Journal of Physical Chemistry A **108** (21), 4587-4598 (2004).
[110]. E. Papagiannakis, M. Vengris, D. S. Larsen, I. H. M. van Stokkum, R. G. Hiller and R. van Grondelle, Use of Ultrafast Dispersed Pump-Dump-Probe and Pump-Repump-Probe Spectroscopies to Explore the Light-Induced Dynamics of Peridinin in Solution, Journal of Physical Chemistry B **110** (1), 512-521 (2006).
[111]. J. T. M. Kennis, D. S. Larsen, I. H. M. van Stokkum, M. Vengris, J. J. van Thor and R. van Grondelle, Uncovering the hidden ground state of green fluorescent protein, PNAS **101** (52), 17988-17993 (2004).
[112]. E. Papagiannakis, I. H. M. van Stokkum, M. Vengris, R. J. Cogdell, R. van Grondelle and D. S. Larsen, Excited-state dynamics of carotenoids in light-harvesting complexes. 1. Exploring the relationship between the S-1 and S* states, Journal of Physical Chemistry B **110** (11), 5727-5736 (2006).
[113]. E. Papagiannakis, M. Vengris, L. Valkunas, R. J. Cogdell, R. van Grondelle and D. S. Larsen, Excited-state dynamics of carotenoids in light-harvesting complexes. 2. Dissecting pulse

structures from optimal control experiments, Journal of Physical Chemistry B **110** (11), 5737-5746 (2006).
[114]. C. MXR, Transient-absorption pump/probe system, Laser Focus World **40** (11), (2004).
[115]. Newport, Capturing ultrafast phenomena, Materials Today **9** (5), 62-62 (2006).
[116]. M. D. Perry and G. Mourou, Terawatt to Petawatt Subpicosecond Lasers, Science **264** (5161), 917-924 (1994).
[117]. C. H. Brito Cruz, P. C. Becker, R. L. Fork and C. V. Shank, Phase correction of femtosecond optical pulses using a combination of prisms and gratings, Opt. Lett. **13** (2), 123 (1988).
[118]. J.-C. M. Diels, J. J. Fontaine, I. C. McMichael and F. Simoni, Control and measurement of ultrashort pulse shapes (in amplitude and phase) with femtosecond accuracy, Applied Optics **24** (9), 1270-1282 (1985).
[119]. R. Trebino, *Frequency-Resolved Optical Gating: The Measurement of Ultrashort Laser Pulses*, (Kluwer Academic Publishers, Dordrecht, 2000).
[120]. R. Danielius, A. Piskarskas, A. Stabinis, G. P. Banfi, P. Ditrapani and R. Righini, Traveling-Wave Parametric Generation of Widely Tunable, Highly Coherent Femtosecond Light-Pulses, Journal of the Optical Society of America B-Optical Physics **10** (11), 2222-2232 (1993).
[121]. R. L. Fork, C. V. Shank, C. Hirlimann, R. Yen and W. J. Tomlinson, Femtosecond white-light continuum pulses, Opt. Lett. **8** (1), 1 (1983).
[122]. A. Brodeur, F. A. Ilkov and S. L. Chin, Beam filamentation and the white light continuum divergence, Optics Communications **129** (3-4), 193-198 (1996).
[123]. C. Gorling, U. Leinhos and K. Mann, Self-trapped exciton luminescence and repetition rate dependence of two-photon absorption in CaF2 at 193 nm, Optics Communications **216** (4-6), 369-378 (2003).
[124]. L. P. Maguire, S. Szilagyi and R. E. Scholten, High performance laser shutter using a hard disk drive voice-coil actuator, Review of Scientific Instruments **75** (9), 3077-3079 (2004).
[125]. L. P. Maguire, S. Szilagyi and R. E. Scholten, High performance laser shutter using a hard disk drive voice-coil actuator (vol 75, pg 3077, 2004), Review of Scientific Instruments **78** (1), (2007).
[126]. K. Ekvall, P. van der Meulen, C. Dhollande, L. E. Berg, S. Pommeret, R. Naskrecki and J. C. Mialocq, Cross Phase moculation artifact in liquid phase transient absorption spectroscopy, Journal of Applied Physics **87** (5), 2340-2352 (2000).
[127]. M. Lorenc, M. Ziolek, R. Naskrecki, J. Karolczak, J. Kubicki and A. Maciejewski, Artifacts in femtosecond transient absorption

spectroscopy, Applied Physics B-Lasers and Optics **74** (1), 19-27 (2002).
[128]. T. Parasassi, F. Conti and E. Gratton, Time-resolved fluorescence emission spectra of laurdan in phospholipid vesicles by multifrequency phase and modulation fluorometry, Cellular and Molecular Biology **32**, 103-108 (1986).
[129]. T. Parasassi, G. De Stasio, A. d'Ubaldo and E. Gratton, Phase fluctuation in phospholipid membranes revealed by laurdan fluorescence, Biophysical Journal **57**, 1179-1186 (1990).
[130]. T. Parasassi, G. Destasio, G. Ravagnan, R. M. Rusch and E. Gratton, Quantitation of Lipid Phases in Phospholipid-Vesicles by the Generalized Polarization of Laurdan Fluorescence, Biophysical Journal **60** (1), 179-189 (1991).
[131]. L. A. Bagatolli and E. Gratton, Two photon fluorescence microscopy of coexisting lipid domains in giant unilamellar vesicles of binary phospholipid mixtures, Biophysical Journal **78** (1), 290-305 (2000).
[132]. C. F. Chapman and M. Maroncelli, Fluorescence Studies of Solvation and Solvation Dynamics in Ionic-Solutions, Journal of Physical Chemistry **95** (23), 9095-9114 (1991).
[133]. R. Karmakar and A. Samanta, Steady-state and time-resolved fluorescence behavior of C153 and PRODAN in room-temperature ionic liquids, Journal of Physical Chemistry A **106** (28), 6670-6675 (2002).
[134]. M. Maroncelli, The Dynamics of Solvation in Polar Liquids, Journal of Molecular Liquids **57**, 1-37 (1993).
[135]. M. Viard, J. Gallay, M. Vincent, O. Meyer, B. Robert and M. Paternostre, Laurdan solvatochromism: Solvent dielectric relaxation and intramolecular excited-state reaction, Biophysical Journal **73** (4), 2221-2234 (1997).
[136]. D. S. Larsen, M. Vengris, I. H. M. van Stokkum, M. A. van der Horst, R. A. Cordfunke, K. J. Hellingwerf and R. van Grondelle, Initial photo-induced dynamics of the photoactive yellow protein chromophore in solution, Chemical Physics Letters **369** (5-6), 563-569 (2003).
[137]. M. Vengris, D. S. Larsen, M. A. van der Horst, O. F. A. Larsen, K. J. Hellingwerf and R. van Grondelle, Ultrafast dynamics of isolated model photoactive yellow protein chromophores: "Chemical perturbation theory" in the laboratory, Journal of Physical Chemistry B **109** (9), 4197-4208 (2005).
[138]. G. Groenhof, M. Bouxin-Cademartory, B. Hess, S. P. De Visser, H. J. C. Berendsen, M. Olivucci, A. E. Mark and M. A. Robb, Photoactivation of the photoactive yellow protein: Why photon absorption triggers a trans-to-cis Isomerization of the chromophore in the protein, Journal of the American Chemical Society **126** (13), 4228-4233 (2004).

[139]. M. E. Martin, F. Negri and M. Olivucci, Origin, nature, and fate of the fluorescent state of the green fluorescent protein chromophore at the CASPT2//CASSCF resolution, Journal of the American Chemical Society **126** (17), 5452-5464 (2004).
[140]. E. ter Meer, Ueber Dinitroverbindungen der Fettreihe, Justus Liebigs Ann. Chem. **181** (1), 1-22 (1876).
[141]. W. Wislicenus and F. Reitzenstein, Zur Kenntniss des Diketohydrindens, Justus Liebigs Ann. Chem. **277** (3), 362-374 (1893).
[142]. L. Harris, J. Kaminsky and R. G. Simard, The Absorption Spectrum of Malachite Green Leucocyanide and the Mechanism of the Dark Reaction after Photolysis, Journal of the American Chemical Society **57** (7), 1151 - 1154 (1935).
[143]. R. Heiligman-Rim, Y. Hirshberg and E. Fischer, Photochromism in Spiropyrans. Part V. On the Mechanism of Phototransformation, Journal of Physical Chemistry **66** (12), 2470-2477 (1962).
[144]. G. H. Brown, *Photochromism*, (Wiley, New York, 1971).
[145]. H. Dürr and H. Bouas-Laurent, *Photochromism: Molecules and Systems*, (Elsevier, Amsterdam, 1990).
[146]. J. C. Crano and R. J. Guglielmetti, *Organic Photochromic and Thermochromic Compounds*, (Plenum Press, New York, 1999).
[147]. Y. Y. Huang, W. Liang, J. K. S. Poon, Y. Xu, R. K. Lee and A. Yariv, Spiro-oxazine photochromic fiber optical switch, Applied Physics Letters **88** (18), (2006).
[148]. M. Irie, T. Fukaminato, T. Sasaki, N. Tamai and T. Kawai, Organic chemistry: A digital fluorescent molecular photoswitch, Nature **420** (6917), 759-760 (2002).
[149]. I. Willner, Photoswitchable biomaterials: En route to optobioelectronic systems, Accounts of Chemical Research **30** (9), 347-356 (1997).
[150]. O. Pieroni, A. Fissi, N. Angelini and F. Lenci, Photoresponsive polypeptides, Accounts of Chemical Research **34** (1), 9-17 (2001).
[151]. T. Hugel, N. B. Holland, A. Cattani, L. Moroder, M. Seitz and H. E. Gaub, Single-molecule optomechanical cycle, Science **296** (5570), 1103-1106 (2002).
[152]. H. Bouas-Laurent and H. Durr, Organic photochromism, Pure and Applied Chemistry **73** (4), 639-665 (2001).
[153]. M. Irie, Photochromism: Memories and switches - Introduction, Chemical Reviews **100** (5), 1683-1683 (2000).
[154]. A. A. Shachkus, Y. A. Degutis and A. G. Urbonavichyus, Synthesis and study of 5a,6-dihydro-12H-indolo[2,1-b][1,3]-benzoxazines, Chemistry of Heterocyclic Compounds **25** (5), 562-565 (1989). Translated from: A. A. Shachkus, J. A. Degutis and A. G. Urbonavichyus, Synthesis and study of 5a,6-dihydro-

12H-indolo[2,1-b][1,3]-benzoxazines, Khimiya Geterotsiklicheskikh Soedinenii, 5, 672-676 (1989).
[155]. M. Tomasulo, S. Sortino and F. M. Raymo, A fast and stable photochromic switch based on the opening and closing of an oxazine ring, Organic Letters **7** (6), 1109-1112 (2005).
[156]. A. Shachkus, J. Degutis and A. Jezerskaite, 5a,6-Dihydro-12H-indolo[2,1-b]-[1,3]-benzoxazines in: *Chemistry of Heterocyclic Compounds*, Vol. 35, ed. J. Kovač and P. Zalupsky (Elsevier, Amsterdam, 1988) pp. 518-520.
[157]. M. Tomasulo, S. Sortino and F. M. Raymo, Bichromophoric photochromes based on the opening and closing of a single oxazine ring, Journal of Organic Chemistry **73** (1), 118-126 (2008).
[158]. M. Tomasulo, S. Sortino and F. M. Raymo, Amplification of the coloration efficiency of photochromic oxazines, Advanced Materials **20** (4), 832-835 (2008).
[159]. M. Tomasulo, S. Sortino, A. J. P. White and F. M. Raymo, Fast and stable photochromic oxazines, Journal of Organic Chemistry **70** (20), 8180-8189 (2005).
[160]. I. H. M. van Stokkum, D. S. Larsen and R. van Grondelle, Global and target analysis of time-resolved spectra, Biochimica Et Biophysica Acta-Bioenergetics **1657** (2-3), 82-104 (2004).
[161]. A. R. Holzwarth, Data Analysis in time-resolved measurements in: *Biophysical Techniques in Photosynthesis*, Vol. 3, ed. J. Amesz and A. J. Hoff (Kluwer Academic, Dordrecht, 1996) pp. 75-92.
[162]. C. G. Xia, J. Peon and B. Kohler, Femtosecond electron ejection in liquid acetonitrile: Evidence for cavity electrons and solvent anions, Journal of Chemical Physics **117** (19), 8855-8866 (2002).
[163]. X. Y. Chen and S. E. Bradforth, The ultrafast dynamics of photodetachment, Annual Review of Physical Chemistry **59**, 203-231 (2008).
[164]. M. W. Allen, J. R. Unruh, B. D. Slaughter, S. J. Pyszczynski, T. R. Hellwig, T. J. Kamerzell and C. K. Johnson, Spectroscopy and photophysics of indoline and indoline-2-carboxylic acid, Journal of Physical Chemistry A **107** (30), 5660-5669 (2003).
[165]. D. V. Bent and E. Hayon, Excited State Chemistry of Aromatic Amino Acids and Related Peptides. III. Tryptophan, Journal of the American Chemical Society **97** (10), 2612-2619 (1975).
[166]. S. V. Jovanovic and S. Steenken, Substituent Effects on the Spectral, Acid-Base, and Redox Properties of Indolyl Radicals - a Pulse-Radiolysis Study, Journal of Physical Chemistry **96** (16), 6674-6679 (1992).
[167]. J. Peon, G. C. Hess, J. M. L. Pecourt, T. Yuzawa and B. Kohler, Ultrafast photoionization dynamics of indole in water, Journal of Physical Chemistry A **103** (14), 2460-2466 (1999).

[168]. Q. K. Timerghazin and G. H. Peslherbe, Electronic structure of the acetonitrile and acetonitrile dimer anions: A topological investigation, JOURNAL OF PHYSICAL CHEMISTRY B **112** (2), 520-528 (2008).
[169]. L. M. Richard, Calibration and Validation in: *Raman Spectroscopy for Chemical Analysis*, Vol. 157, ed. J. D. Winefordner (Wiley Interscience, New York, 2000) pp. 251-291.
[170]. I. A. Shkrob and M. C. Sauer, Electron localization in liquid acetonitrile, Journal of Physical Chemistry A **106** (39), 9120-9131 (2002).